Mechanics of 3D Lattice Structures Produced by Rapid Prototyping

Experiments and Numerical Simulations

Daniel Caduff

Diss. ETH N° 21813

Mechanics of 3D Lattice Structures Produced by Rapid Prototyping

Experiments and Numerical Simulations

A thesis submitted to attain the degree of

Doctor of Science
(Dr. sc. ETH Zurich)

presented by

DANIEL CADUFF

MSc ETH Bau-Ing., ETH Zurich

born 11^{th} May 1983

citizen of Castrisch

accepted on the recommendation of

Prof. Dr. Mario Fontana (examiner)
Institute of Structural Engineering, D-Baug, ETH Zürich

Prof. Dr. ir. Jan G.M. van Mier (co-examiner)
Bergschenhoek, The Netherlands

2014

Printed by the Repro-Zentrale, ETH Zuerich, Switzerland

.

Contents

Zusammenfassung

Stabgitter-Modelle stellen ein geeignetes Instrument dar, um das mechanische Verhalten sowie das Bruchverhalten von spröden, heterogenen Materialien wie Fels, Eis oder Beton numerisch zu simulieren. Das mechanische Verhalten von Gitterstrukturen wird in der vorliegenden Arbeit untersucht wobei die Heterogenität von den genannten Materialien vernachlässigt wird um die Problemstellung zu vereinfachen. Rapid Prototyping wurde für die Herstellung der physischen Gitterstrukturen bestehend aus 9×9×9 Zellen und der einzelnen Gitterstäbe als Produktionsverfahren gewählt, um die experimentellen Daten zu erhalten. Die gewünschte geometrische Genauigkeit und eine gewisse Homogenität im Material wurden durch den Einsatz eines 3D-Photopolymerdruckers erreicht. Der Einfluss von unterschiedlichen Stabschlankheiten und Querschnittgeometrien der Einzelstäbe auf das Verformungsverhalten der Gitterstruktur wurde durch die Verwendung von vier unterschiedlichen Stabformen untersucht.

Das Verformungsverhalten von den Gitterstrukturen wurde anhand zwei unterschiedlicher Modelle simuliert. Die mechanischen Eigenschaften der Einzelstäbe wurden für das klassische Modell gemessen, welches gewöhnlich von anderen Forschern verwendet wird. Die Messungen wurden in einer selbst entwickelten Mikro-Belastungseinrichtung durchgeführt. Ein plastisches Verhalten der Einzelstäbe wurde durch eine Erweiterung des klassischen Modells berücksichtigt. Das getestete Material weist ein visko-elastisches Materialverhalten auf. Die mechanischen Eigenschaften der Einzelstäbe mit den vier unterschiedlichen Formen weisen einen klaren Grössen- und Formeinfluss auf. Daher konnten keine universellen Materialparameter für das klassische Modell gefunden werden.

Ein neuer Modellierungsansatz wurde untersucht, welcher von Van Mier (2007, 2012, 2013) vorgeschlagen wurde. Das Modell ist direkt vom Kraft-Verformungsverhalten der Einzelstäbe abhängig. Viele Annahmen des klassischen Modells können damit vermieden werden wenn das Kraft-Verfomungsverhalten der Einzelstäbe die Basis der Analyse bildet und nicht mehr die klassischen Materialgesetzte auf der Basis von Spannungen und Dehnungen. Die Einzelstäbe wurden unter unterschiedlichen Randbedingungen bzw. verschiedenen Querkraft/Normalkraftverhältnissen und unter Zug- und Druckbelastung in der Mikro-Belastungseinrichtung getestet, um die nötigen Verfomungskurven für das neue Modell zu erhalten.

Die physischen Gitterstrukturen wurden unter Zug- und Druckbelastung getestet. Die Oberflächendeformation wurde während den Experimenten mittels dreidimensionaler Bildkorrelation gemessen, um Informationen über das Verformungsverhalten zu gewinnen. Die unter Zugbeanspruchung belasteten Gitterstrukturen weisen eine ungleichförmige Verformung über die gesamte Höhe auf, was zu einer

hohen Streuung in der gemessenen Maximalkraft führt. Die Ebene mit der kleinsten Verformungsrate schreibt die maximal erreichbare Kraft aufgrund des viskoelastischen Materialverhaltens vor. Die unter Druck beanspruchten Gitterstrukturen weisen eine kleine Streuung in der gemessenen Maximalkraft auf, wobei die Ebene mit der höchsten Verformungsrate die maximale Kraft vorgibt.

Die Resultate der beiden Modelle stimmen mit den Experimenten unter Zugbeanspruchung überein, wobei der neue Modellierungsansatz das Verformungsverhalten der Gitterstrukturen präziser beschreibt. Der neue Modellierungsansatz ist imstande, das visko-elastische Verformungsverhalten zu charakterisieren wobei die Berechnungen des klassischen Modells ein linear elastisches-plastisches Verformungsverhalten ergeben. Die Eingabecharakteristik der Einzelstäbe beschreibt direkt das Verformungsverhalten der Gitterstruktur für beide Modelle. Das klassische Modell reagiert sensitiv auf Veränderungen der Eingabeparameter. Eine kleine Veränderung der Steifigkeit des plastischen Bereichs der Einzelstäbe resultiert in einer ausgeprägten Veränderung der maximalen Gitterdeformation, bei welchem dieses versagt. Der neue Modellierungsansatz weist keine solche Sensitivität auf, was die Zuverlässigkeit der Resultate des neuen Modell unterstreicht.

Das klassische Modell liefert keine befriedigende Resultate für das Verformungsverhalten der Gitterstrukturen unter Druckbeanspruchung, auch wenn die Effekte 2. Ordnung berücksichtigt werden. Mit dem neuen Modellansatz werden bessere Resultate erzielt speziell für Gitterstrukturen, welche Stäbe mit einer grossen Schlankheit enthalten. Die Resultate beider Modelle sind stark abhängig von den Eigenschaften der im Gitter horizontal liegenden Stäbe. Die Veränderung der Eigenschaften der horizontal liegenden Stäbe beeinflusst die maximal erreichbare Kraft des Gitters sowie das Verformunsverhalten nach der Maximalkraft. Die Eigenschaften dieser Stäbe sind schwer zu bestimmen aufgrund des viskoelastischen Materialverhaltens.

Abstract

Beam lattice models are a convenient tool to simulate (numerically) the mechanical and fracture behaviour of brittle disordered materials like rock, ice or concrete. The mechanical behaviour of lattice structures is investigated in this thesis without considering the heterogeneity of the mentioned materials in order to simplify the study. Physical lattice structures (9×9×9 cells) and single beam elements with an accurate geometry were produced by means of Rapid Prototyping. The specimens i.e. the single beam elements and the global lattices were loaded in uniaxial tension and uniaxial compression. A three dimensional photopolymer printer was used to achieve the desired geometrical accuracy and a certain homogeneity in the material. Four different single beam shapes were chosen to investigate the influence of different slenderness ratios and cross-sectional geometries of single elements on the lattice deformation behaviour.

Two different lattice models were investigated to simulate the deformation behaviour of the physical lattice structures. The single beam element properties were measured by using a micro-mechanical loading device for the classical model which is commonly used by other researchers. This model was extended to handle also a plastic behaviour of the beam elements. The material shows a distinct visco-elastic behaviour. The tested single beam elements with the four different shapes show a distinct size and shape effect on the element properties. Universal material properties for the classical model could not be determined.

A new model approach, which was recently proposed by Van Mier (2007, 2012, 2013), was investigated where the model is directly based on the load and displacement information of the single beam elements. Many assumptions of the classical model can thereby circumvented when the load-deformation response of the single element forms the basis for the analysis and not any longer classical constitutive equations based on stress and strain. The single beam elements were also loaded in a micro-mechanical loading device in tension and compression under different loading conditions (i.e. shear to normal force ratios) to obtain the information required for the new model approach.

The physical lattice structures were tested under tensile and compressive load. The surface deformation during the experiments was measured with a three-dimensional image correlation system to obtain the deformation characteristics of the physical lattice structures. The global lattice structures under tension show a non-uniform deformation over the whole height. This leads to a high scatter in the measured maximum forces whereas the layer with the smallest loading rate determines the force capacity. The experiments under compression show a small scatter whereas the layer with the highest loading rate determines the force

capacity.

The results from the classical model and the new model approach are in agreement with the experiments under tensile load. However, the new model approach reproduces the deformation behaviour of the lattice more precisely. It is capable to characterize the visco-elastic deformation behaviour whereas the classical model shows a linear elastic-purely plastic deformation behaviour of the lattice structure. The input characteristic of the single beam elements prescribes directly the structural behaviour in both models. The classical model is more sensitive to changes of the input parameters especially when changing the stiffness of the plastic part of the single element behaviour. Only a small variation leads to a distinct change of the maximum lattice deformation where the lattice fails. The new model approach does not show such sensitivity to changes of the input parameters. This makes the new model approach more reliable.

The simple classical model is not capable to simulate the deformation behaviour of the lattice structures under compression. The measured deformation behaviour could not be simulated satisfactory, also not when the second order effect was taken into account. The new model approach shows a better agreement with the experiments especially for lattice structures which contain beams with a high slenderness. The results from both models strongly depend on the properties of the in-plane beams loaded in tension. The properties of these beams influence the maximum force and the deformation behaviour after the maximum force. The in-plane beam properties are difficult to determine due to the visco-elastic material behaviour. These beams have a low deformation rate compared with the out-of-plane beams loaded under compression.

1. Introduction

1.1. Background

The understanding of the mechanical and fracture behaviour of building materials is of high interest to construct and build safe civil engineer structures i.e. large constructions like bridges. The material properties have to be evaluated in the laboratory on specimen sizes from 100mm up to 10m whereas the size of the civil engineer constructions lies beyond this level. Therefore, fundamental knowledge of materials and structures is needed to develop better mechanical and fracture models that can predict the behaviour of the materials at this size of structures.

A convenient tool to simulate (numerically) the mechanical and fracture behaviour of brittle disordered materials like rock, ice or concrete are simple truss or beam lattice models. Herrmann et al (1989) first studied the fracture in disordered materials using a beam lattice model. Subsequently, different approaches of lattice models were proposed to study the fracture mechanics in different disordered materials. Many input parameters can influence the outcome of the results from these simulations. Trusses instead of beams can be used, the difference between regular and random distributed beams in the lattice was studied or statistically distributed material properties were assigned to the beams. The selection of the fracture criterion like the Rankine or the Von Mises criterion and different softening behaviour of the beams have a high impact on the fracture behaviour.

A lattice model where the heterogeneity of the material is taken into account by projecting the material structure on top of the lattice and assigning properties of various phases to the individual beams was first introduced by Van Mier and his co-workers (Schlangen and Van Mier (1992a); Schlangen (1993), Vervuurt (1997)). A simple one-dimensional constitutive equation is sufficient to model the material behaviour. Satisfactory results were achieved for the tensile and shear fracture behaviour of disordered materials where the selection of the mechanical properties and the fracture law for the different phases plays a key role in the numerical simulations. The size and shape effect was successfully simulated by Man (2010) using this type of model, although the calculated size-range was for computational reasons rather narrow. However, simulations by means of this type of lattice model did not show very satisfactory results in the case of compressive fracture.

1.2. Scope of the research

The aim of the present research is to improve the understanding of the mechanical behaviour of lattice structures and to separate the influence of the geometrical (i.e. the size and the shape of one single beam element) and the material properties (i.e. modulus of elasticity E, yield stress f_{pl}) in the model to the structural behaviour. The material heterogeneity was not considered in a first attempt to simplify the topic. Physical lattice structures (9×9×9 cells) and single beam elements with an accurate geometry were produced by means of Rapid Prototyping to obtain the experimental data. A three dimensional photopolymer printer was used to achieve the desired geometrical accuracy and homogeneity in the material. Four different single beam shapes were chosen to investigate the influence of different slenderness ratios and cross-sectional geometries of single elements on the lattice deformation behaviour.

Two different lattice models were investigated to simulate the deformation behaviour of the physical lattice structures. The single beam element properties (modulus of elasticity E_{beam}, yield stress f_{pl} and the maximum deformation $\delta_{beam,max}$) were measured by using a micro-mechanical loading device for the classical model which is commonly used by other researchers. This model was extended to handle also a plastic behaviour of the beam elements. Subsequently, the physical lattice structures were tested under tensile and compressive load. The surface deformation during the experiments was measured with a three-dimensional image correlation system to obtain the deformation characteristics of the physical lattice structures.

A new model approach is investigated where the model is directly based on the load and displacement information of the single elements which was already introduced by Van Mier (2007, 2012, 2013). Many assumptions of the classical model can thereby circumvented when the load-deformation response of the single element forms the basis for the analysis and not any longer classical constitutive equations based on stress and strain. The single beam elements were also loaded in a micro-mechanical loading device in tension and compression under different loading conditions (i.e. moment to normal force ratios) to obtain the information required for the new model approach. The loading conditions were chosen by analysing the force distribution in a global lattice structure using the classical lattice model where the results are only dependent on the single element geometry and the used material properties are irrelevant.

The experiments are compared with both models to obtain informations about the applicability to simulate the structural behaviour of such types of lattices. The sensitivity of the models is investigated by means of parameter studies. The influence of varying material parameters on the deformation behaviour of the global lattice illustrates the challenge to separate the geometrical and material parameters conclusively.

1.3. Outline of the thesis

This thesis is divided into seven Chapters. After an overview of both types of simulation processes used, the specimen generation and the model assumptions are described in detail. The performed experiments are explained and the comparison between the simulations and experiments have been studied. The contents of subsequent Chapters is as follows:

- Chapter 2:

  A description of the lattice model concept and its application in research is given. The generation of the lattice model structure is explained. The simulation processes of the classical model and the new model approach are described. The classical model is extended to consider plastic material behaviour. The principle of video image correlation is discussed which will be used in the single beam element tests and the global lattice experiments to obtain a better understanding of the deformation behaviour.

- Chapter 3

  The principle of Rapid prototyping is explained where three different processes are illustrated. The specimen generation and production method for the single beam element tests and the global lattice experiments are described. A Model assumption for the simulations is introduced to handle specimens with a non-constant cross-section over the length. The generation of the specimens for the new model approach is described in detail to obtain the correct force-deformation curves for the simulations.

- Chapter 4

  The micro-mechanical behaviour of the single beam elements for the classical model and the new model approach are investigated. The micro-mechanical testing device and the parameters that influences the mechanical properties of the elements are described. The results from the single beam element tests are discussed and a method to measure the modulus of elasticity of the elements using video image correlation is introduced.

- Chapter 5

  The macro-mechanical behaviour of the global lattice under tensile and compressive load is investigated. The testing setup for both type of experiments is explained in details. The results are discussed with regards to the measured deformation behaviour of the layers in the lattice using video image correlation. The model assumption is verified in order to examine the applicability in the simulations.

- Chapter 6

  The comparison between the macro-mechanical experiments and the simulations is presented, The applicability of the models are verified by comparing

the deformation behaviour of the lattice structures with the numerical results. Parameters studies for both models are carried out to investigate the sensitivity of the models when changing the input parameters. The fracture behaviour of the models is compared with the experiments in tension.

- Chapter 7

  The observations from the last Chapter are concluded and the advantages and disadvantages are summarized for both models. An outlook is given on topics how the specimens have to be redesigned and what sort of production method is more favourable than used in this thesis to obtain more certainty about the geometrical and the material influences on the global lattice behaviour.

2. Preliminary investigations

2.1. Lattice modelling

2.1.1. Concept

Among others, lattice models are used to discretise a continuum and form a simple method to simulate fracture in quasi-brittle material by generating a network of two or three dimensional spring, trusses or beam elements. Hrennikoff (1941) first proposed the idea replacing a continuum by trusses. Hrennikoff used the lattice approximation to solve linear elastic problems. The lattice theory was adopted in the 70's to simulate fracture and creep processes at the atomistic scale by studying the behaviour of square lattice structures (Thomson et al (1971) and Hsieh and Thomson (1973)). In statistical physics, lattice models were introduced to study fracture of disordered media. The fracture model was initially reduced to a scalar problem by applying the electric analogy where each element was reduced to a resistor (Duxbury et al (1987)). Fracture was simulated by loading the lattice with an increasing current. Once the current reached a certain value in an element, the resistance becomes infinite and the element reacts as an insulator. The current will be increased until the whole lattice is no longer conducting. It was found in the 80's that this analogy was not appropriate to compare experimental results and simulations. Fracture in disordered media was then studied by Herrmann et al (1989) using two dimensional beam-lattice models. In this simulation, the element with the highest ratio of mechanical stress over the tensile strength is removed one after another.

Different lattice models were subsequently used to model fracture in disordered material where the implementation of heterogeneity (particle projection or statistically distribution of the mechanical properties), the type of elements (trusses or beams) and the adopted fracture criterion (linear elastic with or without softening) were changed. Burt and Dougill (1977) assigned different stiffness and strengths on the elements in a random network structure to study the influence of the material heterogeneity on the stress-strain-curve. Simulations of lattices in square configuration from physicists showed a Poisson's ratio of $v = 0.0$. Triangular lattices were then preferred to simulate fracture in quasi-brittle material due to the possibility to adjust the Poisson's ratio (Schlangen and Van Mier (1992b)). Schorn and Rode (1989) adopted the lattice model to the third dimension where the linear elastic trusses were connected to each other in a regular cubic pattern. The elements preserved different stiffness as well as tensile and compressive strength of a certain distribution.

Van Mier and his co-workers developed a lattice model (Schlangen and Van Mier (1992a); Schlangen (1993)) where the heterogeneity was implemented by projecting the lattice on the internal structure of concrete and by assigning different properties to the elements dependent in which region the element is located. Beams instead of trusses are used in this model because on one hand it is possible to take a wide range of the Poisson's ratio into account and on the other hand it permits to simulate crack bridging, where intact material pieces link the crack faces as was observed in experiments by Van Mier (1991). Schlangen and Garboczi (1997) illustrated that a simulation with trusses leads to simple crack pattern while using beams, complex crack pattern can be achieved. Results based on the work of Nooru-Mohamed (1992) show this conclusion, where shear simulations on double-notched square specimens with homogeneous lattices were performed. Ince et al (2003) showed the influence by using Timoshenko beams instead of Bernoulli beams on the load-displacement response while the difference is quite small (between 5% to 10%).

The model of Schlangen and Van Mier (1992a) was adopted by other researchers (Bolander Jr et al (1996), Bolander and Sukumar (2005), Joseph and Jefferson (2007)). It is also used to describe the fracture of different materials for instance fibre concrete (Bolander et al (2008)), asphalt concrete (Kim and Buttlar (2005)) or wood (Landis et al (2002)). Due to the development in parallel computing and larger computer facilities, the model was successfully extended in the third dimension by Lilliu and Van Mier (2003) and Liliu (2007). The three-dimensional model takes the realistic internal structure of the concrete into account and the simulations lead to a better performance for the softening behaviour of concrete for tensile experiments. The lattice model is in general capable to simulate a softening behaviour of the material by using a linear elastic-purely brittle constitutive law for the beams and mapping the internal structure. It gives the opportunity to have a better insight in the origin of softening. Man and van Mier (2008) and Man (2010) studied the size and shape effect in three-dimensional numerical concrete where the internal aggregate distribution was determined through Magnetic Resonance Imaging (MRI).

Compared to the approach taking the internal structure of the material into account to describe the mechanical material behaviour, there are many attempts to achieve this by varying the fracture behaviour of the single beams. Schorn and Rode (1989) used a criterion related to the Rankine criterion. They specified for every truss a statistically distributed tensile and compressive stress. The Von Mises yield criterion was used by Herrmann et al (1989), but this approach did not lead to a realistic simulation for fracture in compression. Arslan et al (1995) assumed the beam properties as linear elastic-plastic to achieve a plastic fracturing in the lattice model. By changing the ultimate strain of the beam, they reached a better result of the softening behaviour of concrete under uniaxial tension than by using a linear elastic-purely brittle fracture law.

Lattice structures have the same composition like cellular solids. Cellular solids are structures that consist of hollow cells with solid edges or faces, combined together to fill space in the solid. Different cellular solids appear in nature like sponge, cork or wood. Man-made cellular solids nowadays are honeycomb material as well as open- or close- cell foams of polymers, metals, glass or ceramics. There is a wide range of applications of cellular solids like insulation, absorbing kinetic energy, cushioning and the usage as building material.

In contrary to the discretisation of the continuum in fracture mechanics, researchers in the field of cellular solids evaluate the properties of these materials by using discrete models. Gibson and Ashby (1997) give an overview of the application and mechanical behaviour of cellular solids. Studies in the early development in cellular solids were done by Suh (1980), Suh and Webb (1985), Wendle (1976), Hilyard (1982) and Hilyard and Cunningham (1994). They studied the collapse of single cells and approximated the results to the general behaviour of cellular solids. To investigate the size effects, Onck et al (2001) modelled the structure of honeycombs in a finite element program, where the struts are described as a continuum material. Constitutive laws for the system response were developed on the basis of experimental results obtained from tests on foams with varying densities (Andrews et al (2001)). Schmidt and Fleck (2001) studied the influence of cell irregularities on the stress intensity factor also by modelling the internal structure as a set of finite element struts. Mangipudi and Onck (2011) used for the multi-scale analysis of metallic foams the elastic beam formulation by Crisfield et al (2012). With this method, the influence of cell shape anisotropy and size effects were investigated. To take the exact geometry of the internal microstructure of open cell foam into account, X-ray tomography was used by Jang and Kyriakides (2009a). They tested the material under compression and simulated the behaviour with a finite element program, where they used beam elements with variable cross sections and adopted the exact geometry of the cells in the model (Jang and Kyriakides (2009b)).

2.1.2. Generation of the lattice model

Different types of lattices are used to discretise the continuum. Lattices in a random configuration are applied in the model where the internal structure of the material is unknown to represent the heterogeneity in the material. Regular lattices are used in models, where the internal structure is included by applying different material properties dependent in which phase of the material the beam is laying. The lattice network can be generated by square or triangular arrangement. In this thesis, triangular regular lattices with equal beam length are investigated due to their widespread application in fracture mechanics.

Triangular lattice structures can be constructed through an approach from the crystallography. In two dimensions, circles with equal diameters are arranged in a hexagonal arrangement (Figure 2.1(a)). One circle is surrounded by six neighbouring circles. Through connecting the centres of every circle with its neighbours, the regular triangular lattice network is constructed. Modelling of

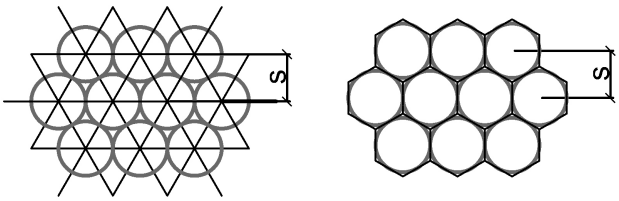

(a) (b)

Figure 2.1.: Different two-dimensional lattices: (a) Triangular and (b) Honeycomb configuration

cellular solids, respectively honeycomb structures in two dimensions is done by connecting every centre of a triangle with the centres of neighbouring triangles (Figure 2.1(b)). Gibson and Ashby (1997) describe the mechanical response and the fracture mechanism of such structures. In both cases, the beam lengths in the lattice are the same (Beam length in triangular lattice: 1· circle diameter s; Beam length in honeycomb lattice: $\sqrt{3}/3$· circle diameter s).

Three-dimensional lattices are constructed in the same way like the two-dimensional lattices. Instead of circles, spheres with diameter s are arranged in space considering the closed packed arrangements of hexagonal sphere-layers. The distance d between two layers is:

$$d = \frac{\sqrt{6}}{3} \cdot s \tag{2.1}$$

Layer B and C can be placed in two different relations relative to Layer A (Figure 2.2). In the hexagonal closed packed structure (hcp, Figure 2.2(a)), every second layer is the same (ABAB). In the centred cubic packing (fcc, Figure 2.2(b)), every third layer is the same (ABCABC). The distance d between the layers keeps the same for both configurations. The difference in these arrangements is the existence of two different types of triangular gaps dependent on the layer order. Each sphere has 12 neighbours in every case: 6 in the same layer and both 3 on the lower and upper layer. The beams in the lattice are constructed by connecting the centres of every sphere with the neighbouring centres.

A side view of the two different layer arrangements is showed in Figure 2.3. It shows the geometry of the lattice boundary. The lower and upper boundary layers of the regular lattice are planar. The layers are used in the simulation to apply the external forces or displacements. The vertical boundaries of the lattices are disturbed which is normal for a triangular type lattice. To quantify the disturbance, the maximal relative horizontal difference between two layers can

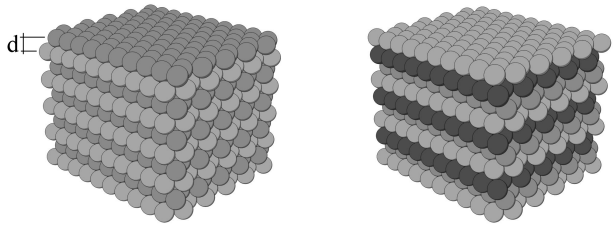

(a) hpc packing (b) fcc packing

Figure 2.2.: 3D sphere packing: (a):hcp packing (light grey layer A; grey layer B), (b) fcc packing (light grey layer A; grey layer B; dark grey layer C)

be calculated for both structures.

$$x = \frac{\sqrt{3}}{6} \cdot s \qquad y = \frac{\sqrt{3}}{3} \cdot s \tag{2.2}$$

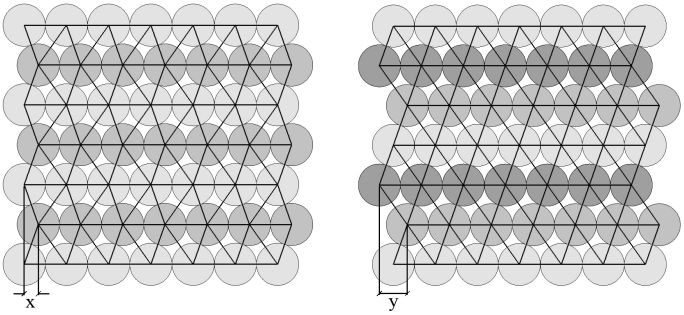

(a) hcp lattice (b) fcc lattice

Figure 2.3.: Side view of two different 3D lattice configuration

The fcc lattice has a two times higher relative horizontal difference than the hcp lattice. To achieve a more homogeneous force and deformation behaviour in the lattice, only the hcp configuration will be investigated in this thesis.

A number of different cell configurations in 3D is used to describe the microstructure of cellular materials. A common geometry for simulating the mechanical behaviour of open cell foams is the Kelvin cell (Figure 2.4(b)). The analogy in modelling the two different domains (continuum and open cell foam modelling) is obvious (see Figure 2.4). In both cases, a frame of trusses or beams

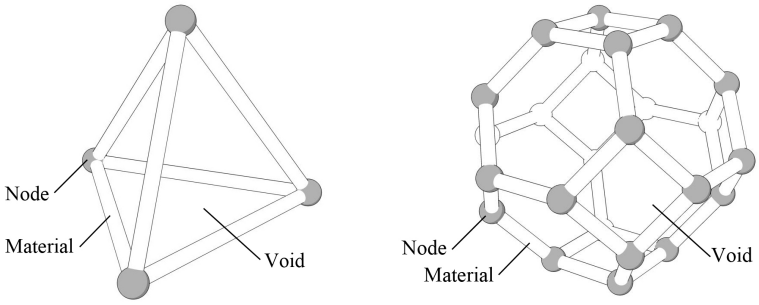

(a) Triangle cell (b) Kelvin cell

Figure 2.4.: Analogy between lattice and cellular structures modelling

connects the nodes to describe the structure. Therefore, the same model is supposed to work for both point of views.

2.1.3. Fracture Simulation

This section describes how the deformation and fracture of a lattice can be modelled. Two different models will be investigated. The first model refers to the classical method which is appropriate in this field of fracture research by now (Schlangen and Van Mier (1993), Bolander et al (2008), Man (2010) etc.). This model is extended to handle a linear elastic-purely plastic material behaviour. The geometrical stiffness matrix is implemented in the model to investigate its influence on the deformation behaviour of the lattice under compression. A new approach will be presented, first hypothesized by Van Mier (2007, 2012, 2013), where the constitutive formulation of the material behaviour and the fracture law of a single beam are not necessary any more.

Classical model

In the classical beam lattice model, the direct stiffness method is used to calculate the deformations and the forces in single Bernoulli beam elements. The global stiffness matrix is calculated from the local stiffness matrix (Equation 2.3) by

transformation in the global coordinate system.

$$\begin{bmatrix} F_{x,i} \\ F_{y,i} \\ F_{z,i} \\ M_{x,i} \\ M_{y,i} \\ M_{z,i} \\ F_{x,j} \\ F_{y,j} \\ F_{z,j} \\ M_{x,j} \\ M_{y,j} \\ M_{z,j} \end{bmatrix} = \begin{bmatrix} \frac{EA}{L} & 0 & 0 & 0 & 0 & 0 & -\frac{EA}{L} & 0 & 0 & 0 & 0 & 0 \\ & \frac{12EI_z}{L^3} & 0 & 0 & 0 & \frac{6EI_z}{L^2} & 0 & -\frac{12EI_z}{L^3} & 0 & 0 & 0 & \frac{6EI_z}{L^2} \\ & & \frac{12EI_y}{L^3} & 0 & -\frac{6EI_y}{L^2} & 0 & 0 & 0 & -\frac{12EI_y}{L^3} & 0 & -\frac{6EI_y}{L^2} & 0 \\ & & & \frac{GJ}{L} & 0 & 0 & 0 & 0 & 0 & -\frac{GJ}{L} & 0 & 0 \\ & & & & \frac{4EI_y}{L} & 0 & 0 & 0 & \frac{6EI_y}{L^2} & 0 & \frac{2EI_y}{L} & 0 \\ & & & & & \frac{4EI_z}{L} & 0 & -\frac{6EI_z}{L^2} & 0 & 0 & 0 & \frac{2EI_z}{L} \\ & & & & & & \frac{EA}{L} & 0 & 0 & 0 & 0 & 0 \\ & & & & & & & \frac{12EI_z}{L^3} & 0 & 0 & 0 & -\frac{6EI_z}{L^2} \\ & & & & sym. & & & & \frac{12EI_y}{L^3} & 0 & \frac{6EI_y}{L^2} & 0 \\ & & & & & & & & & \frac{GJ}{L} & 0 & 0 \\ & & & & & & & & & & \frac{4EI_y}{L} & 0 \\ & & & & & & & & & & & \frac{4EI_z}{L} \end{bmatrix} \times \begin{bmatrix} u_i \\ v_i \\ w_i \\ \varphi_{x,i} \\ \varphi_{y,i} \\ \varphi_{z,i} \\ u_j \\ v_j \\ w_j \\ \varphi_{x,j} \\ \varphi_{y,j} \\ \varphi_{z,j} \end{bmatrix} \tag{2.3}$$

The deformations and forces in the nodes can be calculated by solving the following Equation:

$$F = K \times U \tag{2.4}$$

Equation 2.4 is used independently if external deformations or forces are applied on the lattice structure. The beam forces in the local coordinate system are calculated through back transformation of the global forces at the nodes.

Using a linear elastic-purely brittle constitutive law for the beam behaviour (Figure 2.5(a)), the fracture is simulated by removing a single beam element in the mesh for every load step. A uniformly distributed unity displacement or force is applied on the lattice and the element with the highest stress over tensile strength ratio is removed. The failure criterion considers the normal force and the maximum moment at the end of the beam to calculate the maximum stress in the beam as follows:

$$\frac{\sigma_i}{f_{\{t,pl\}}} = \frac{1}{f_{\{t,pl\}}}\left(\frac{F_i}{A} + \alpha \times \frac{max\left\{|M_i|, |M_j|\right\}}{W_{\{el,pl\}}}\right) \geq 1 \tag{2.5}$$

A refers to the cross sectional area of the lattice beam and W to the cross sectional modulus of resistance. The elastic modulus of resistance W_{el} is taken into account for linear elastic behaviour. The parameter α considers the influence of the bending moment in this criterion. In fracture mechanics of concrete, the influence of the parameter α on the tail of the stress-deformation curve was investigated by Schlangen (1993) for two dimensional analysis and by Liliu (2007) for three-dimensional analysis. The maximum external displacement or force, where one beam fails, is determined by multiplying the unit load with the factor

$$\frac{1}{\mu} = max\frac{\sigma_i}{f_{t,i}} \tag{2.6}$$

In this case, all other elements will not fail:

$$\mu \cdot \frac{\sigma_i}{f_{t,i}} < 1 \tag{2.7}$$

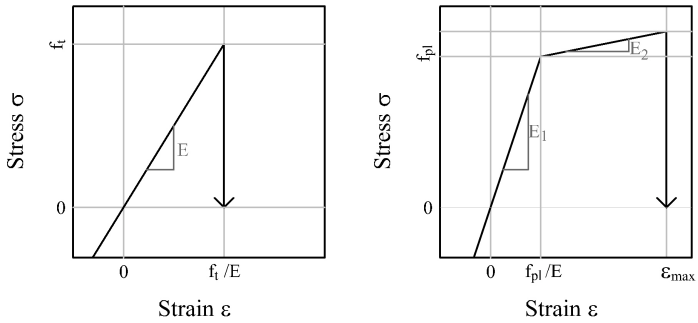

Figure 2.5.: Stress-strain relation of a single lattice element: (a) linear elastic-purely brittle, (b) linear elastic-ideal plastic-purely brittle

The global stiffness matrix is recalculated for the lattice without the failed element and the procedure starts over.

The simulation process for the lattice model with linear elastic-ideal plastic material behaviour is illustrated in Figure 2.6. Figure 2.5(b) shows the stress-strain diagram of the estimated material property. In comparison with the elastic solution, there are two more parameters to consider: the stiffness of the plastic plateau E_2 and the ultimate strain ϵ_{max}. The internal forces and displacements for every lattice element are stored after each step to handle the two new parameters in contrast to the common method where the calculation starts from zero for each step. The advantage is that the new parameters can directly be implemented in the simulation. Arslan et al (1995) reduced the effective modulus of elasticity for every step dependent on the deformation of each element to simulate the linear elastic-plastic behaviour. This method leads to iterations whereas the deformations and forces can directly be determined with the described method.

The element stresses in this model are also calculated with Equation 2.5. Compared to the linear elastic analysis, the plastic modulus of resistance W_{pl} will be inserted. This will lead to a small overestimation of deformation, when a cross-section of one beam reaches the yielding plateau. However, the ultimate stress in the beam is not influenced. To check whether the stress or the strain criterion is reached, two new parameters are introduced:

$$\xi_{i,j} = \frac{1}{f_{pl}}\left(\frac{f_{pl} - \sigma_{i,j-1}}{\sigma_{i,j}}\right) \qquad \zeta_{i,j} = \frac{1}{\epsilon_{max}}\left(\frac{\epsilon_{max} - \epsilon_{i,j-1}}{\epsilon_{i,j}}\right) \tag{2.8}$$

where i indicates the element and j indicates the step number. By finding the minimum of these two values, the load or strain factor equal to Equation 2.6 can

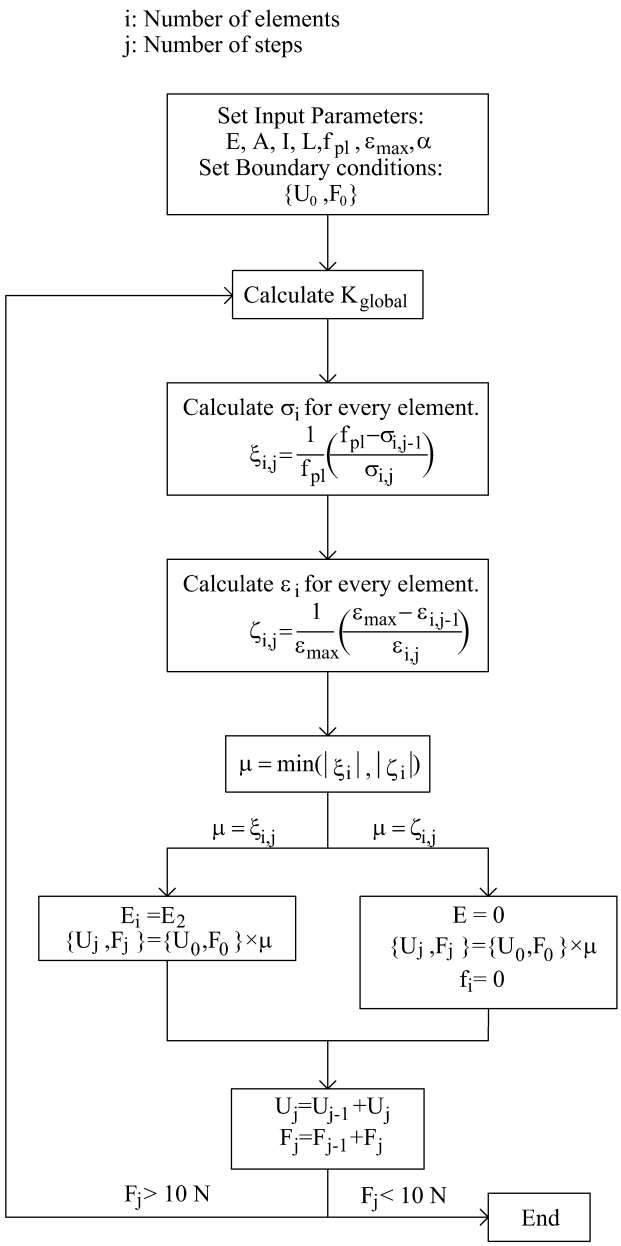

Figure 2.6.: Classical Simulation process

be found:

$$\mu = min(|\xi_{i,j}, \zeta_{i,j}|) \tag{2.9}$$

Dependent if the plastic stress or the ultimate strain is reached, the modulus of elasticity for the critical element is set differently in the next step. In addition, the internal forces are set to zero in the second case which corresponds to the removal of the element from the lattice.

The following two Equations are valid for every element in the lattice depending whether the yield stress of an element is first reached,

$$\mu(\frac{\sigma_{i,failed}}{f_{pl}}) = 1 \text{ and } \mu(\frac{\sigma_{n\neq i}}{f_{pl}}) < 1 \tag{2.10}$$

or the ultimate strain is reached

$$\mu(\frac{\epsilon_{i,failed}}{\epsilon_{max}}) = 1 \text{ and } \mu(\frac{\epsilon_{n\neq i}}{\epsilon_{max}}) < 1 \tag{2.11}$$

For the fracture process, it is possible that the load factor μ reaches a negative value due to change in the global stiffness matrix which leads to a different internal force distribution.

It is assumed in the current models that the deformations in the structure are negligibly small. Sufficient accurate results are reached for analysing the equilibrium in the undeformed configuration. If the deformations are large (strain $> 0.05\%$), analysing the equilibrium for the deformed configuration leads to more accurate results and stability effects like buckling are directly taken into account. The geometrical stiffness matrix has to be included in the simulations for this purpose:

$$k_g = \frac{T}{L}\begin{bmatrix}
0 & 0 & 0 & 0 & 0 & 0 & 0 & 0 & 0 & 0 & 0 & 0 \\
0 & \frac{6}{5} & 0 & 0 & 0 & \frac{L}{10} & 0 & -\frac{6}{5} & 0 & 0 & 0 & \frac{L}{10} \\
0 & 0 & \frac{6}{5} & 0 & -\frac{L}{10} & 0 & 0 & 0 & -\frac{6}{5} & 0 & -\frac{L}{10} & 0 \\
0 & 0 & 0 & 0 & 0 & 0 & 0 & 0 & 0 & 0 & 0 & 0 \\
0 & 0 & -\frac{L}{10} & 0 & \frac{2L^2}{15} & 0 & 0 & 0 & \frac{L}{10} & 0 & -\frac{L^2}{30} & 0 \\
0 & \frac{L}{10} & 0 & 0 & 0 & \frac{2L^2}{15} & 0 & -\frac{L}{10} & 0 & 0 & 0 & -\frac{L^2}{30} \\
0 & 0 & 0 & 0 & 0 & 0 & 0 & 0 & 0 & 0 & 0 & 0 \\
0 & -\frac{6}{5} & 0 & 0 & 0 & -\frac{L}{10} & 0 & \frac{6}{5} & 0 & 0 & 0 & -\frac{L}{10} \\
0 & 0 & -\frac{6}{5} & 0 & \frac{L}{10} & 0 & 0 & 0 & \frac{6}{5} & 0 & \frac{L}{10}0 & \\
0 & 0 & 0 & 0 & 0 & 0 & 0 & 0 & 0 & 0 & 0 & 0 \\
0 & 0 & -\frac{L}{10} & 0 & -\frac{L^2}{30} & 0 & 0 & 0 & \frac{L}{10} & 0 & \frac{2L^2}{15} & 0 \\
0 & \frac{L}{10} & 0 & 0 & 0 & -\frac{L^2}{30} & 0 & -\frac{L}{10} & 0 & 0 & 0 & -\frac{2L^2}{15}
\end{bmatrix} \tag{2.12}$$

where

$$T = EA(u_j - u_i)/L \tag{2.13}$$

The matrix is dependent on the normal force T in the elements. It is added to the local stiffness matrix (Equation 2.3) to achieve the second order local stiffness matrix of one single Bernoulli beam. This results in an iterative process during the simulation. The equilibrium is reached in one iteration for displacement controlled simulations. In a first step, the global stiffness matrix is built to calculate the normal forces in the elements. In a second step, the internal normal forces are included by Equation 2.12 and the forces in the elements are calculated for the deformed equilibrium. For force controlled simulations, appropriate iteration methods can be chosen (modified Newton-Rapson, Arch-length method etc.) to calculate the equilibrium.

New approach

The new approach is based on the consideration to take the force-displacement curve for one element directly into account to describe the fracture behaviour of the lattice. Van Mier (2007) and Van Mier (2012) described the approach in terms of using the interaction potential between two atoms in the atomistic scale to describe the material behaviour for large scales. Considerations are made for structural lattices. Taking the force-displacement curves into account has several advantages compared to the classical modelling of lattice structures. One of the main features is that the material properties respectively the assumed constitutive laws are not necessary any more to calculate the stiffness matrix. Also the approval of the specific fracture law is not needed any longer because this information is all contained inside the force-displacement curve of an element. In addition, the information about the stress distribution over a cross section of an element and the inclusion of the geometrical stiffness matrix (Equation 2.12) to consider stability effects also become unnecessary for this type of input.

The basis for this approach is to access to a database of experimental data for single beams with exactly the same geometry as they are present in the lattice and which are tested under the same load and boundary condition as in the lattice structure. This results in a database of force-displacement curves for different types of loading conditions. Figure 2.7 illustrates the process of the new model. In a first step, the loading condition of every beam has to be calculated. This is done in the classical way by estimating the global stiffness matrix in which the value of the modulus of elasticity is indifferent. This proposition is evident when looking at the form of the stiffness matrix (Equation 2.3). Assuming following Equation for isotropic material

$$G = \frac{E}{2 \cdot (1 + \nu)} \tag{2.14}$$

the modulus of elasticity can be excluded from the matrix and it only includes geometrical terms.

By applying a force or displacement load on the lattice, the relative displacement w_1 and the load distribution for every element is calculated. Figure 2.8(b)

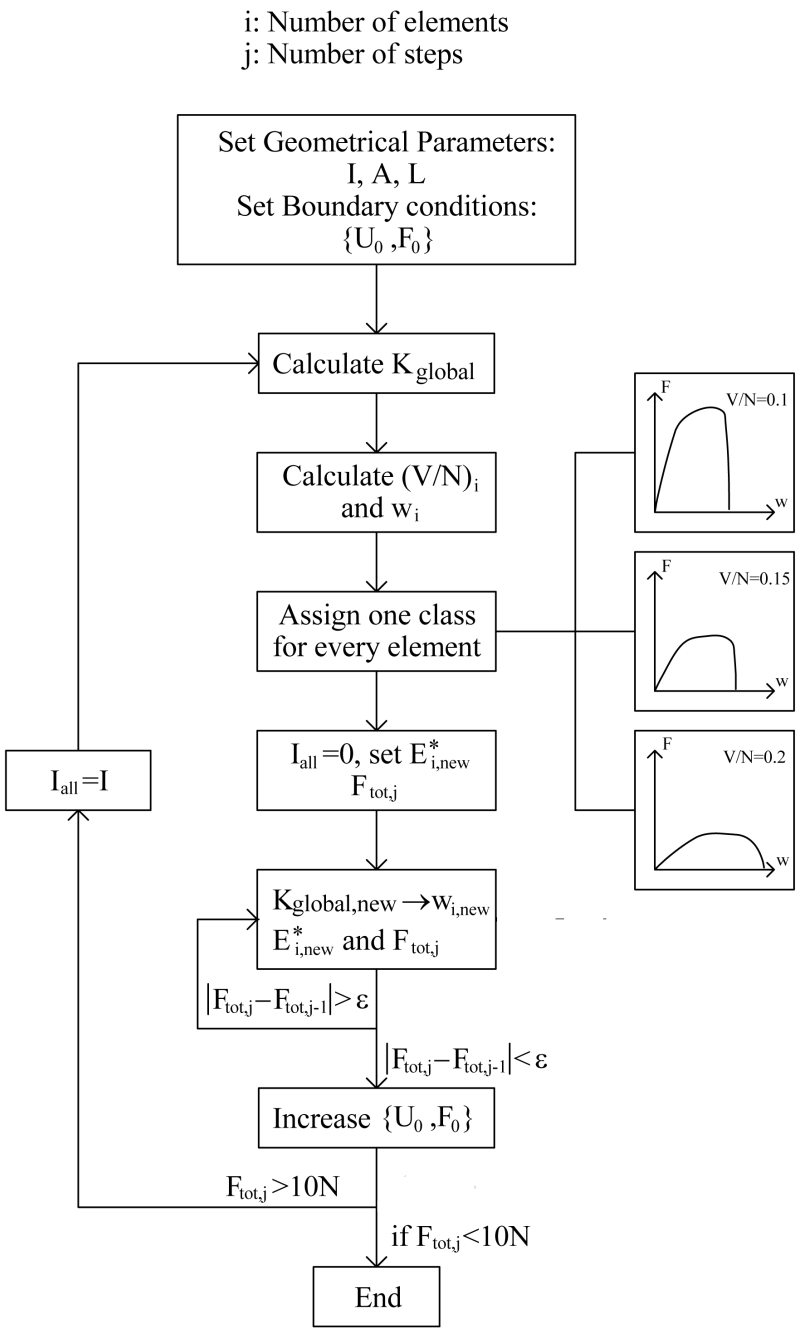

Figure 2.7.: Simulation process for the new approach

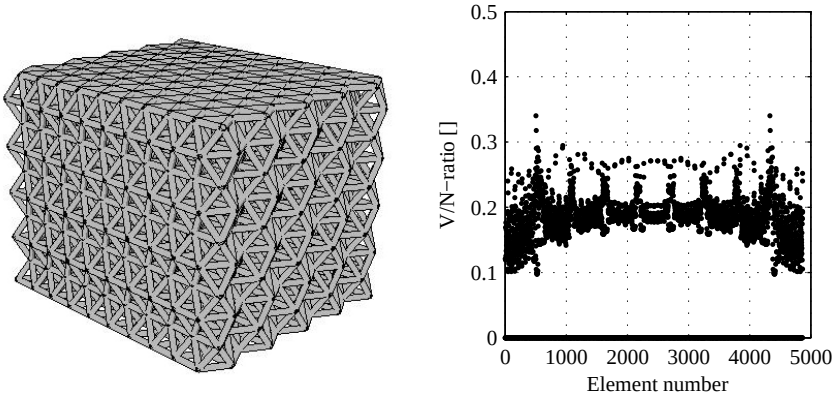

(a) (b)

Figure 2.8.: Element force distribution for lattice elements: (a) Regular lattice, (b) V/N-ratio for all elements

shows the distribution of the shear to normal force ratio i.e. V/N-ratio for all elements in a regular lattice (Figure 2.8(a)). It is obvious that there is a distribution in the lattice, i.e. not every element has the same loading condition.

By assigning a force-displacement curve from the database to every element which corresponds to the same loading condition, the force in every element is captured with respect to the relative displacement of the element (Figure 2.9(a)). This leads to a change of the secant modulus of elasticity whereas an iteration process is necessary. The moment of inertia I and the polar moment of inertia J will be set to zero before the iteration starts because the information about the V/N-ratio is included in the force-displacement curve. Only the relative displacements w_i are relevant to solve the equilibrium from Equation 2.4. The iteration stops until certain accuracy for the calculated external force is reached:

$$F_{tot,j} - F_{tot,j-1} < \epsilon \tag{2.15}$$

The external load or displacement can be increased after the iteration stops. The simulation process start over due to the fact that the force distribution in the lattice has changed. This leads to a new assignment of different force-displacement curves to every element. The simulation stops when the lattice structure drops under a certain external force level.

Both models are compared with the experiments on the lattice structures in Chapter 6 on the basis of experimental results on single lattice elements. The experimental results are discussed in Chapter 4 for single elements and in Chapter 5 for lattice structures.

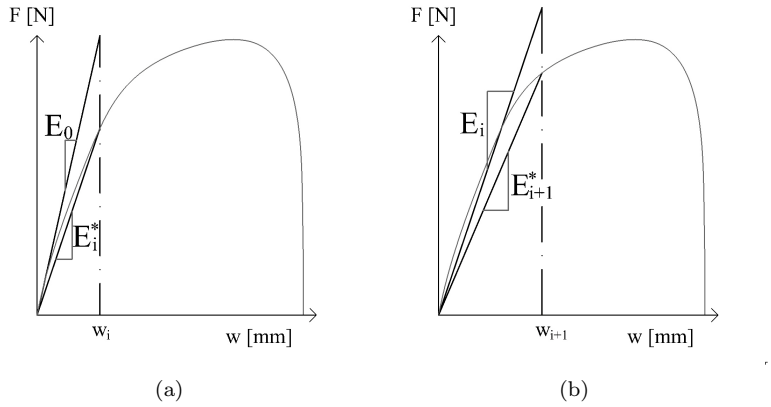

Figure 2.9.: Force-displacement diagram for a given V/N-ratio: (a) First calculation step of modulus of elasticity E_i^*, (b) Second calculation step of modulus of elasticity E_{i+1}^*

2.2. Digital image correlation

Digital image correlation is a convenient tool to measure surface deformations of specimens and to identify strain distributions in the analysed material. Digital image correlation (DIC) is used in single element tests to determine the modulus of elasticity of the material which is needed as an input parameter for the classical lattice model (see Chapter 2.1.3). DIC is also used to capture the surface strain distribution during experiments on lattice structure in order to verify certain model assumptions and the uniformity of the deformation on the lattice. This Chapter gives an overview of the DIC process and the required specimen preparation.

2.2.1. DIC process

The method was investigated in the $80's$ in the field of experimental mechanics to detect surface deformations. Chu et al (1985) and Hild and Roux (2006) describe the procedure for identifying the surface deformations. Nowadays, this technique is used in a wide field of applications. Grediac (2004) gives an overview of the measurement methods in composite materials as well as the advantages and disadvantages by using this technique. Godara and Raabe (2007) used DIC to investigate the influence of glass fibre alignment in polymers where Jerabek et al (2010) determined the strain distribution on polymer specimens under tensile load. Wattrisse et al (2001) analysed the strain localization in steel for tensile experiments. The deformation behaviour of fibre reinforced composites was studied by Giancane et al (2010) whereas Vanlanduit et al (2009) investigated the

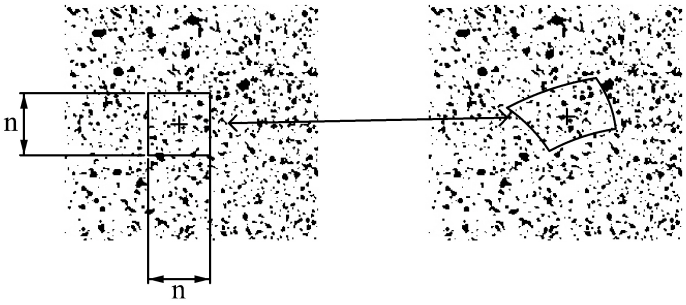

Figure 2.10.: Subset shape with pixel size n before (left) and after (right) deformation

fatigue and crack growth process on aluminium. The technique is also applied for detecting strain concentrations respectively cracks at an early loading stage and debonding phenomena's. Kuentz et al (2006) analysed the crack behaviour of a reinforced concrete beam. Studying the crack distribution on micro fibre reinforced cement specimens under tensile load was done by Rieger (2010). Caduff and Van Mier (2010) investigated the crack nucleation and growth on three different types of concrete under compressive load. The interfacial debonding properties in concrete were analysed by Corr et al (2007).

The principle of two dimensional digital image correlation is composed of comparing two grey scale pictures before and after a certain surface deformation. To calculate the movement of a single pixel in the image, a square pixel area around the pixel is taken into account (subset). This area must have a unique character in order to recognise it in the deformed state. The grey scale values of the area before and after the deformation are compared using the following Equation:

$$C(x,y,u,v) = \sum_{i,j=-n/2}^{n/2} (I(x+i,y+j) - I^*(x+u+i,y+v+j))^2 \qquad (2.16)$$

C:	Correlation function
x,y:	Coordinates of the centre pixel in undeformed state
u,v:	Displacement of the centre pixel
n:	Subset size [pixel]
$I(...)$:	Grey scale value in undeformed state
$I^*(...)$:	Grey scale value in deformed state

Equation 2.9 represents the classical correlation function, which calculates the least square error of the subsets. A perfect match in the deformation calculation corresponds to a value of $C = 0$. Due to noise effects and deformations in the sub-pixel field, the correlation function never reaches zero. Calculating the defor-

mation in the sup-pixel region is done by using a Fourier or iterative algorithm. The cross-correlation function surface is calculated over a range of deformations u and v on the basis of the Fourier algorithm. The exact deformations are found by fitting the calculated cross-correlation surface in the sub-pixel range where the maximum surface peak corresponds to the deformations. Hild and Roux (2006) and Sutton et al (2009) describe the different algorithms in details. The deformed subset shape does not have to be square due to rotations, enlargements or reductions in the movement. The deformation field is expanded with Taylor arrays of the order zero to two. The second order allows curvatures along the subset sides.

The light conditions can change during the recording of the surface which leads to a change of grey scale values in the pictures. In this case, to avoid erroneous calculated deformation of the correlation function in this case, a photometric transformation is used to produce a rugged algorithm

$$I(x, y) = P(I^*((x + u, y + v)) \tag{2.17}$$

where P is the photometric transformation function.

Different interpolation functions are implemented in the transformation to interpolate the grey scale values in the sub-pixel size and to reach a continuity in the subset area.

Strains in two dimensions can be calculated from the measured deformations using

$$\varepsilon_{\mathrm{xx}} = u_{,\mathrm{x}} + 0.5(u_{,\mathrm{x}}^2 + v_{,\mathrm{x}}^2) \tag{2.18}$$

$$\varepsilon_{\mathrm{yy}} = v_{,\mathrm{y}} + 0.5(u_{,\mathrm{y}}^2 + v_{,\mathrm{y}}^2) \tag{2.19}$$

$$\gamma_{\mathrm{xy}} = 0.5(u_{,\mathrm{y}} + v_{,\mathrm{x}}) \tag{2.20}$$

One camera is used for two dimensional detection of deformations which stands perpendicular to the subjected surface. Out-of-plane deformations cannot be detected and they can lead to poor deformation calculations. To measure deformations in the third dimension, two cameras are required. Both cameras are used to view the same area of the specimen (Figure 2.11). The deformation calculations are done by stereo correlation. A calibration is required with this technique to determine the position of the two cameras. A high accuracy in the calibration leads to a high accuracy in the deformation calculation.

The strains in the third dimension are calculated through the Nabla function

$$\varepsilon_{\mathrm{xx,yy,xy}} = \nabla(u_{\mathrm{x,y,z}}, v_{\mathrm{x,y,z}}) \tag{2.21}$$

Strains are calculated at the same subset centres as the deformations were determined. The surrounding centres are taken into account with a certain weight. Close centres have a higher weight than distant centres. The accuracy is enhanced

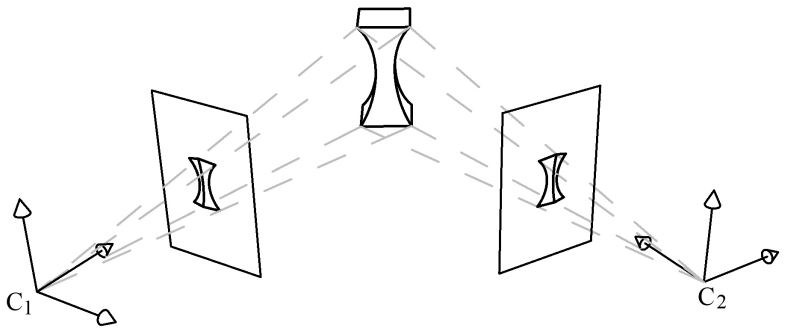

Figure 2.11.: Camera positions (C_1, C_2) for three dimensional deformation measurement

by considering more centres for image noise reduction but local strain concentrations cannot be detected any more. Therefore, the number of centres included in the calculation has to be considered depending on the character of the investigation. For instance, are we interested in a homogeneous strain calculation or is the focus on strain localisation.

The computational time of correlating the subsets and calculating the strains has also to be considered. More computational time is consumed when the subset size is increased. A subset size of more than $n = 25$ pixels does not lead to a more accurate deformation calculation. By increasing the number of analysed subset centres, the deformation field is more precise as the calculated strain concentrations on a nearby area. The computational time increases linearly with the number of analysed subset centres. Therefore, it has to be considered what type of information are required for the target investigation before starting the correlation calculations.

2.2.2. Sample preparation

Calculating the deformations requires a random and not repeating pattern of the observed sample surface in order to identify the subsets in the unreformed and deformed state. If the sample surface does not show a useful specific pattern, a random speckle pattern has to be applied on the surface. The applied film may not influence the material behaviour and should deform simultaneously with the surface. The application is done by spraying a continuous film of white paint on the surface. The paint should not reflect the light which will lead to erroneous deformation calculations. An airbrush is used to generate a random speckle pattern with black colour. The speckle size is dependent on the resolution of the cameras and the size of the observed area on the surface that the subset includes at least 3 by 3 speckles.

3. Specimen production and generation

3.1. Introduction

Producing specimens for single element and lattice structure experiments requires a high accuracy in the fabrication to avoid irregular or imperfect geometries. Due to the undercut geometry of the lattice structures, common fabrication methods such as CNC drilling or the application of simple mould techniques are not convenient. Techniques with lost moulds are not appropriate due to the complexity in the production process, to achieve the desired geometry and to sustain a homogeneous material behaviour for every part. Rapid prototyping is capable to produce complex undercut specimens with a high geometrical accuracy and certain homogeneity in the material considering a few construction rules. This Chapter gives an overview of the functionality of rapid prototyping and describes the fabricated geometries of the single element and lattice structure specimens. Three different rapid prototyping methods will be described in detail.

3.2. Rapid prototyping

Prototyping or model making is used to verify a conceptualisation of a design. At the early ages until now, manual prototyping is applied to build prototypes by employing different production methods like castings, moulds, material removal or joining. This fabrication method is time consuming dependent on the complexity of the model and leads to high costs (Metelnick (1991)). Rapid prototyping (RP) or solid free form fabrication was invented to reduce the time and costs of fabricating models. The principle of this production method consists in lying thin layers of a material over each other to build a three dimensional structure (Figure 3.1). First attempts with this technique were made in the 19th century at which wax plates were cut with a specific contour. The free form volume was created by laying the plates on top of each other (Bourell and Beaman (2012)). The first presentation of a photo-polymer rapid prototyping system was in 1981 (Prinz et al (1997)) where a photo-polymer resin is cured with an UV-laser layer by layer. Due to the enhancements in computer technology, rapid prototyping had been growing through the last three decades and there are more than 30 production techniques on the market by now. Kruth (1991), Kochan (1993), Beaman et al (1997) and Chua et al (2010) describe the historical trends and the

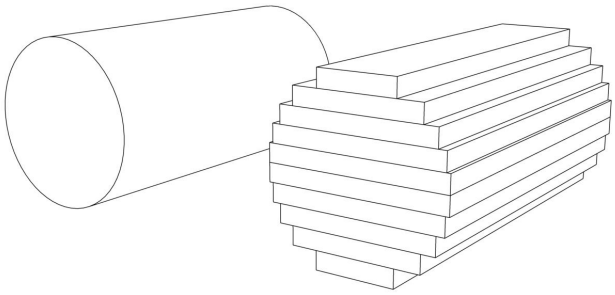

Figure 3.1.: Illustration of the layer modelling technique in rapid prototyping process

different production methods for RP. The processing goes from rapid prototyping to rapid tooling at which fabricated parts are directly deployed for mechanical loaded machine components.

3.2.1. Stereolithography

Stereolithography (SL) describes a process, where ultraviolet-curable resin polymerizes during an exposure with a laser. Jacobs (1992) and Jacobs (1995) describe the process in detail. During the process, an elevator platform is located below the surface of a liquid thermoset polymer. The desired polymer area above the elevator is exposed with an ultraviolet laser, which leads to solidification. The hardened parts adhere on the top of the elevator. The platform shifts downwards by the height of the next layer. During the next exposure of the liquid polymer, the material in contact with the previous layer solidifies. The whole model is build by repeating the process. The solidified part is finally removed from the platform and the uncured resin is washed off using an adequate solvent. The part is in a green state and it has to be post cured by exposure to UV light in a chamber to reach the final strength of the material. Due to the mandatory connection of the layers to each other, support structures have to be considered to build layers for overhanging parts. The support structures are removed after the post-curing of the model. Acrylic based resins were used initially whereas nowadays different resins are on the market with improved accuracy and strength properties.

Different parameters influence the properties of the final part. Curtis et al (2003) investigated the optimization of build parameters for different resin types to avoid different material properties in the same part. The existence of cured and uncured resin in the same green state part can cause shrinkage and distortion during post-curing. Fuh et al (1997) optimized the build parameters to achieve parts with a high accuracy and homogeneous material parameters. Decreasing the layer thickness leads to a higher strength of the material (Chockalingam et al (2008)).

Post-curing of the green state samples leads to a change of the material properties. Parts, which were exposed to UV light and microwave show greater values for the yield and ultimate strength as well as the modulus of elasticity (Curtis et al (2003) and Salmoria et al (2005)). Different degrees of curing induce a variation in strength, while post-curing improves the toughness in conjunction with the durability (Cheah et al (1997) and Karalekas and Rapti (2002)). Post processing with electroplating of the green part to improve the mechanical properties was used by Saleh et al (2004). Improving the material properties by adding reinforcing materials like fibres, Nano tubes and other materials was also investigated (Cheah et al (1999), Sandoval and Wicker (2006), Sandoval and Wicker (2006)).

3.2.2. Selective Laser Sintering

In contrast to the stereolithography process, powder material is used in the Selective Laser Sintering (SLS) fabrication process to build the desired parts. The process was invented by Deckard (1988), where a laser fuses thermoplastic polymer powder together, building the part. The principle of the layer technique remains the same as in the SL-process. Different materials (thermoplastics, composites, metals or ceramics) are capable for the SLS production as long as heat-fusible powder of the specific material can be produced. The part is build in a chamber where the environmental temperature is below the melting or the glass-transition temperature of the used powder material. The production speed is increased since only a few degrees of locally heating is necessary to fuse or sinter the powder by means of a CO_2 laser. The chamber is filled with an adequate gas to avoid chemical reactions of the powder. The unconsolidated powder provides the support material for overhanging parts. The specimen is cleaned from the powder by air or brush after the process is completed. Post-curing is not required to improve the material properties.

Different parameters in the SLS-process influence the material properties as well as the geometrical accuracy. The powder grain size and powder blend influences both the part strength as its durability (McAlea (1997)). The application of different laser types with different energy levels is investigated to achieve a better coupling between the grains which leads to a denser material part respectively better mechanical properties (Tolochko et al (2000), Santos et al (2004), Abe et al (2001)). Santos et al (2006) give an overview of the development using different laser systems. Agarwala et al (1995) observed the influence of the laser scanning speed on the material density. Pre-heating of the powder was investigated to reduce the residual stresses in the build part due to the concentrated energy input (Klocke et al (1995)).

3.2.3. Jetted Photopolymer

Jetting heads are used to release droplets of photopolymer material at the desired position. Multiple jetting heads are required to release both the part and support photosensitive material separately. Curing takes place directly after the material

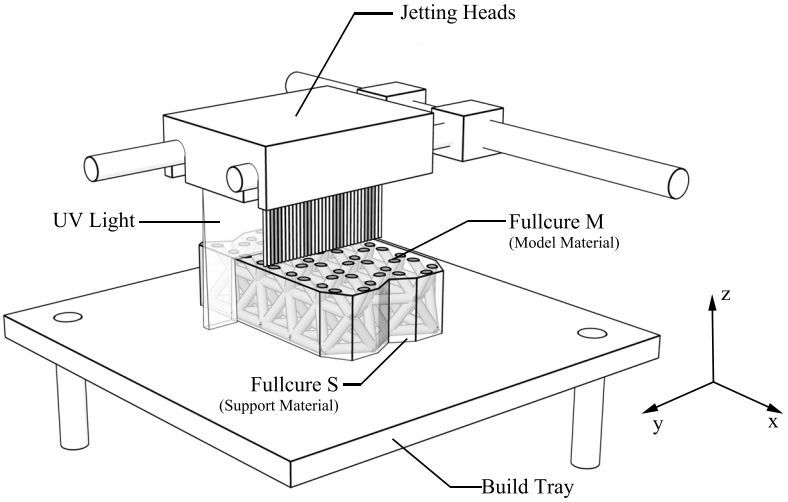

Figure 3.2.: Production principle for jetted photopolymer process; This technique is used to produce all specimens

release by subjecting it to UV light. The UV light sources are integrated in the jetting heads (Figure 3.2). After finishing one layer of the part, the build tray moves downwards vertically for one layer thickness. The jetting heads have to move only in the x-y-plane. The support material is washed out by using a water jet after the part has been finished. The part is fully cured after the building process and post-processing is not necessary. The jetted photopolymer process was first invented by Fudim (1988) and the first commercial PolyJet machine for rapid prototyping was introduced by *Objet3d* in 2000.

The fabricated parts are mainly used for design studies or in the jewellery industry. Therefore, the influence of different process parameters on the material properties has not investigated until now.

3.2.4. Process Comparison

Each process is based on the same principle namely building a part using the layer technique. Table 3.1 lists the main properties of the three described processes. The in-plane and the out-of -plane accuracy of the desired part depends on the fabrication process. The thinnest layers as the best in-plane accuracy can be reached with the jetted photopolymer process whereas the in-plane accuracy depends on the size of the produced part for the stereolithography process. Different materials can be used for SL and SLS, whereas only acrylic photopolymers are available for jetted photopolymer application. Post-curing is needed in the SL-process to reach the desired material properties.

Table 3.1.: Comparison of Rapid Prototyping process properties

	SL	SLS	Jetted Photopolymer
Minimum layer thickness $[mm]$	0.05	0.1	0.016
In-plane accuracy	0.1-0.2% of part dimension	0.1-0.5 mm	0.02-0.2 mm
Build material	Different liquid photopolymers	Different powders	Acrylic photopolymer
Post-curing	Yes	No	No

Figure 3.3.: 3D Printer Objet Eden 500V

The jetted photopolymer process is used in this thesis to produce the desired parts due to the high geometrical accuracy of the specimen production and to avoid post-curing of the parts. All specimens are produced with the machine type $Eden\ 500V$ from $Objet3D$ (Figure 3.3) which uses the PolyJet technique. The maximum size of the produced part can be $500 \times 300 \times 200mm$. The acrylic photopolymer $FullCure720$ is used for the material parts and $FullCure705$ serves as support structure. All specimens used in this thesis are constructed with the NURBES modelling software $Rhinoceros\ V5.0$ from $RobertMcNeel\&Associates$. Ma et al (2001) describes the advantages of using NURBES models for designing parts for Rapid Prototyping. Binary STL-files (Standard Tesselation Language) were exported to the $Objet3D$ printing software. The export parameters are listened in Appendix A.1.

3.3. Single beam geometry

The single beam element properties (modulus of elasticity E_{beam}, yield stress f_{pl} and maximum deformation $\delta_{max,beam}$) needed in the classical simulation (Fig-

ure 2.6) are determined using the specimens shown in Figure 3.4. Four different specimen shapes are considered. The cross-sectional geometry (square or round) and the cross-sectional area in the middle of the beam vary. Two different cross-sectional shapes are chosen to investigate the influence on the deformation behaviour of lattice structures, to verify the simulations which should be independent of the cross-sectional shape and to determine the influence of the beam shape on the single element properties. Two different cross-sectional areas are used to vary the slenderness of the beams and to inspect any size effects on the single beam properties in the chosen dimension range. The cross-sectional area in the middle of the specimen has the same value between the large square and the large round cross-sections (Figure 3.4(a) and 3.4(b)) as well as between the small square and the small round cross-sections (Figure 3.4(c) and 3.4(d)). The length of the beams corresponds to the node distance in the simulation and is the same for all four geometrical shapes. The parts which contain a cylindrical hole serve as support in the single element experiments where the testing device is described in Chapter 4.2.1.

The dimensions were chosen on considerations of the production process and the handling of the specimens. The cleaning of the global lattice specimens from the support material is done by using a water jet with a certain pressure. The water jet can destroy single beams in the lattice structure when the cross-sectional area of the beams is too small. A too large beam cross-sectional area interferes with the water jet when penetrating the lattice structure to the centre. The water pressure will decrease to a level in the centre where it is not possible any more to wash out the support structure. Increasing the water pressure to clean the centre is not suitable due to risk damaging the beams. The same considerations are valid for the length of the beam between the nodes. Increasing the beam length leads to a higher distance from the lattice surface to the centre. A higher water jet pressure is necessary to wash out the support material where the risk for a beam failure increases.

A constant radius over the length for every specimen shape was chosen for two main reasons. Uniaxial tensile tests are performed to measure the tensile strength of material with different types of ductility (brittle, quasi-brittle, ductile). The specimen shape for different ductile materials is standardized in DIN 50125 (2009) for metallic materials or DIN 53504 (2009) and ASTM D638 (2008) for plastics. The specimen shape for brittle material is not standardized. Van Vliet (2000) suggested a dogbone-shaped specimen with freely rotating supports to identify the tensile strength of a quasi-brittle material like concrete. There are several advantages and disadvantages using different specimen shapes to measure the tensile strength. Van Vliet (2000) and Rieger (2010) analysed the stress distribution for different specimen shapes whereas nearly the same analysis is made here but for slightly different specimen shapes. Figure 3.5 illustrates the stress distribution for three different specimen shapes under tension in the elastic regime. The bright areas of the specimens correspond to high stresses. The advantage of using a rectangular shaped specimen (Figure 3.5(a)) is the well-

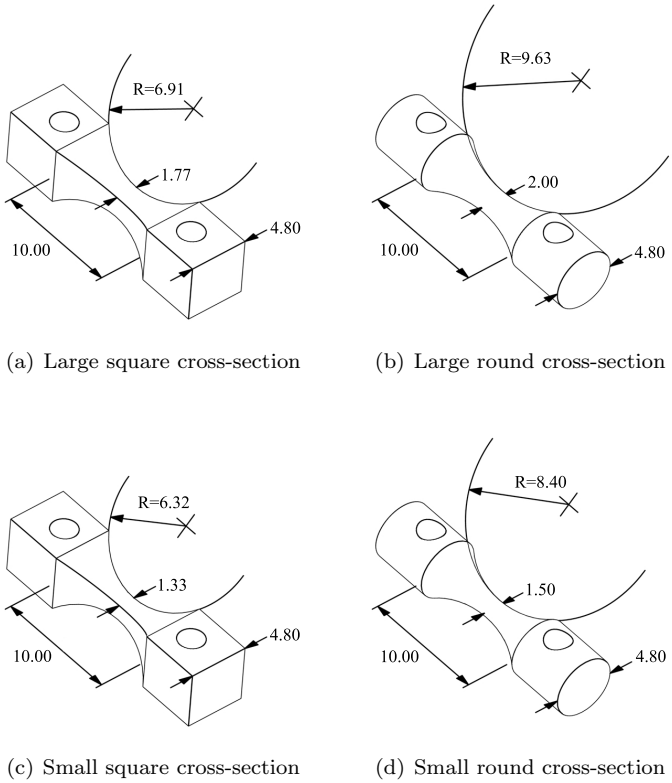

(a) Large square cross-section

(b) Large round cross-section

(c) Small square cross-section

(d) Small round cross-section

Figure 3.4.: Single beam geometries; Dimensions in [mm]

defined geometry as the stress distribution of the part between the supports but there are stress concentrations near the edges as can be seen in Figure 3.5(a). This can lead to failure at the intersection between the specimen and the supports during the experiment. The stress concentrations can be reduced by rounding the edges to reduce the stress concentrations which leads to a dumbbell shaped specimen form (Figure 3.5(b)). This shape is commonly used to identify the tensile strength of ductile materials. Small stress concentrations remain at the intersection between the curved part and the straight part which also can lead to a geometrical induced failure of the specimen. Using a constant radius over the whole specimen height (Figure 3.5(c)) eliminates the stress concentrations between the support parts and the specimen. The highest stress is located in the middle part of the specimen. Thereby, the analysis is in agreement with Van Vliet (2000) and Rieger (2010). The problem remains that the stress distribution in the middle part is not fully constant over the whole cross-section, but the risk of a geometrical induced failure is minimised. On this account, dogbone shaped

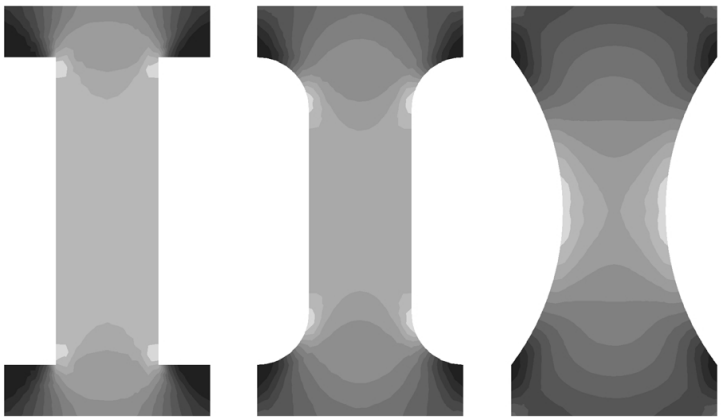

(a) Rectangular (b) Dumbbell (c) Dogbone

Figure 3.5.: Stress concentration for three different specimen shapes

specimens with a constant radius are used in this thesis for the single beam experiments. A nearly constant stress distribution in the middle cross-section can be reached by maximizing the radius of the dogbone which leads to a thinner specimen shape. A too large radius is not suitable as illustrated before due to the cleaning process of the specimens.

Another reason to analyse the mechanical behaviour of single beams with variable cross-section over the length is to investigate the adaptability of the lattice model to the behaviour of open-cell foams. The beams in open-cell foams exhibit variable cross-sections due to the production process of this material. Jang and Kyriakides (2009b), Onck et al (2004) and Gong et al (2005) took the variable cross-sections into account to model the mechanical behaviour of open-cell foams under tensile and compressive load. The basic lattice model calculates the forces in the single beams using constant cross-section areas A and moment of inertias I over the whole length of the beam. Equivalent constant areas A_{eq} and moment of inertias I_{eq} can be calculated to take the variable cross-section of single beams in global lattice structures into account. The methods to calculate the equivalent geometrical parameter are described in section 3.4.

The print orientation must also be considered in the evaluation of the single beam properties. Depending on the alignment of the specimens in three dimensional space, the mechanical properties will vary due to the layered production process of the parts. Figure 3.6 illustrates the four different possible orientations of the single beams in a triangular lattice structure. Hague et al (2004), Quintana et al (2010) and Dulieu-Barton and Fulton (2000) investigated the influence of the material orientation on the mechanical properties for standardized tensile test specimens produced with stereolitography. They tested specimen orientations in

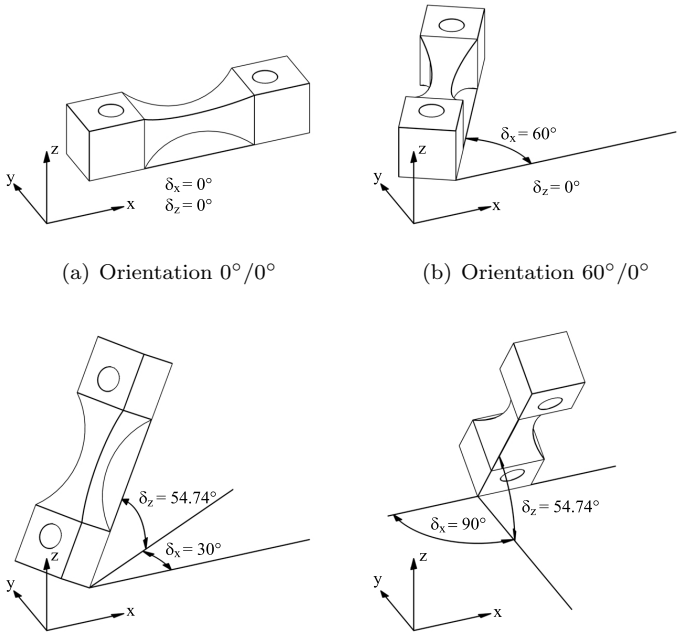

(a) Orientation 0°/0°

(b) Orientation 60°/0°

(c) Orientation 30°/55°

(d) Orientation 90°/55°

Figure 3.6.: Single beam orientations in a triangular lattice

the main directions x, y and z and found differences in the properties dependent on the print orientation. Equivalent investigations for the PolyJet production are not known.

The first angle in the captions of Figures 3.6(a)-3.6(d) corresponds to the orientation angle of the specimen in the x-y-plane (i.e. in-plane) and the second angle corresponds to the out-of-plane angle. The coordinate system is consistent with the system defined in Figure 3.2 which describes the jetted photopolymer production process. A persistent layer is printed in the x-y-plane at which the layers are lying on each other in the z-direction. Two different print direction effects can be studied with this set-up, namely the influence of different in-plane angles (orientation 0°/0° vs. 60°/0°) and the influence of the out-of-plane angle (orientation 0°/0° vs. orientation 30°/55°) on the material properties of the specimens.

The variation of the cross-sectional shape combined with the variation of the print orientation results in sixteen different specimen configurations.

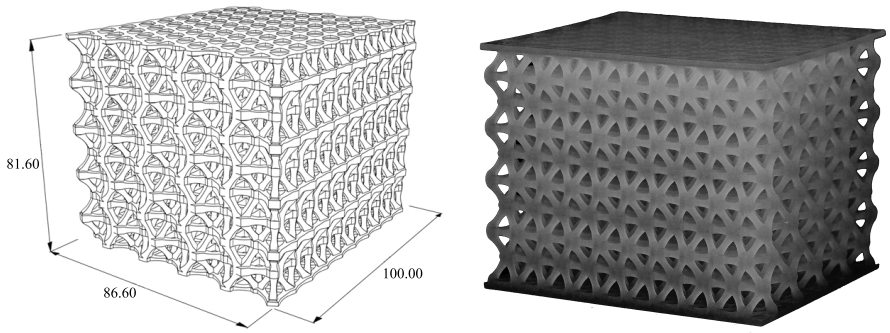

(a) Lattice dimensions

(b) Picture with support plates on the bottom and top of the structure

Figure 3.7.: Lattice geometry containing large square cross-sectional beam elements; Dimensions in [mm]

3.4. Lattice geometry

The tested lattice structures consist of 1′000 nodes and 5′130 beam elements. 10 by 10 node points are arranged in the x-y-plane and 10 layers are stacked in the z-direction in the hexagonal closed packed arrangement (hcp packing, Figure 2.2(a)). The length between the nodes is 10 mm and this results in a lattice dimension of $100 \times 86.6 \times 81.6$ mm. The beam geometries from Figure 3.4 are used for the shapes of the single beam elements in the lattice structures. Figure 3.7 illustrates the constructed lattice structure containing large square cross-sectional beam elements. The illustrations for the lattice structures which contain the other three different beam types are listed in Appendix A.2.

The internal nodes are constructed by rotating the single beam elements in the nodes to the desired orientation. The overlapping areas of the beams that do not intersect are cut off. The removed areas are marked in grey in Figure 3.8(a) for the two dimensional case. The external knots are constructed by cutting off the area at the outer intersection line where the beams cross each other (Figure 3.8(b) for two dimensional case).

Plates with a thickness of $5mm$ are printed directly on the bottom and the top of the lattice structure (Figure 3.7(b)). These plates are used for applying an external load to the global lattice.

3.5. Single beam geometry for new approach

The internal force distribution in the global lattice has to be known to define the boundary conditions for the single beam elements tests. The variation of the boundary conditions leads to different force-deformation curves which are

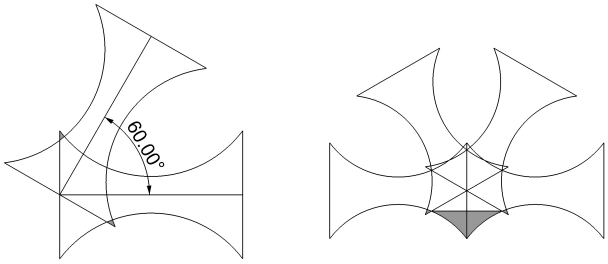

(a) Internal knot construction (b) External knot construction

Figure 3.8.: Construction principles for lattice structures; Grey: Cut off areas

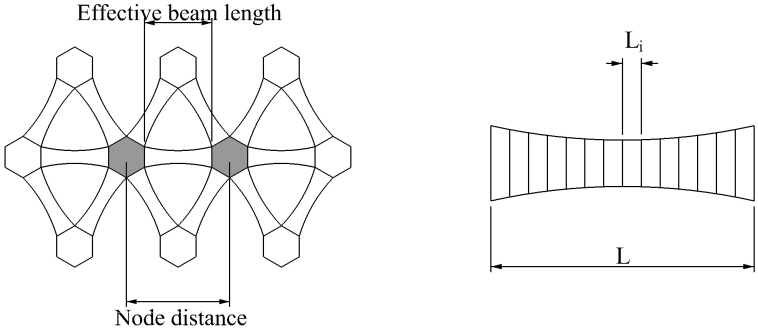

(a) Effective beam length (b) Beam length division

Figure 3.9.: Modelling principles for geometrical property calculation

needed in the new model approach (Figure 2.7). The same beam shapes are used as described in Chapter 3.4. The geometrical parameters, namely the area A, moment of inertia I and beam length L of the single beams have to be identified for a linear-elastic analysis of the lattice structure to achieve the element forces in the beams.

The linear-elastic analysis of the lattice structure was done by defining the bottom plane nodes of the lattice as fixed in x, y and z direction and a uniformly distributed displacement u_z was applied on the top plane nodes. The Poisson's ratio was set to $\nu = 0.3$ in order to substitute the shear modulus G with the modulus of elasticity E according to equation 2.14. The V/N-ratios in the beams are therefore independent of the modulus of elasticity E. Model assumptions are made to evaluate the geometrical parameters.

The main assumption of the model consists in defining the inter-sectional area/ volume in the nodes as completely rigid (areas marked in grey in Figure 3.9(a)).

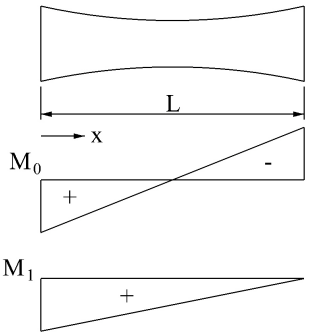

Figure 3.10.: Variable definition for the equation of kinetics

Every beam bordering on a node has a different normal force, a different bending moment and a different shear force. This leads to a complex stress distribution in the nodal areas. Therefore, the amount of the bending stiffness from the nodes with respect to the bending stiffness of the single beam is hard to predict. Also the nodal area, which deforms under normal force cannot be predicted directly. The suggested model assumption avoids making estimates of the deformation ratio of the knot to the global lattice deformation and it simplifies the calculation of the geometrical single beam parameters used in the simulations. This assumption is evaluated by analysing the lattice deformation under tensile and compressive load (Chapter 5) and in the simulations (Chapter 6).

The effective beam length between the rigid node sections (Figure 3.9(a)) is measured from the three dimensional lattice models in the construction software *Rhinoceros* and they are listed in Table 3.2 for every beam shape. The constant equivalent area A_{eq} of the variable cross-sectional beam is calculated by applying a normal force F to the beam. The elongation of the beam is calculated with the following equation

$$\delta l = \sum_{i=1}^{n} \delta l_i = \sum_{i=1}^{n} \frac{F \times L_i}{E \times A_i} \tag{3.1}$$

where the beam is divided into infinite small layers in which the cross-section is assumed to be constant (as indicated in Figure 3.9(b)). The elongation of every layer under the given force F is accumulated. The equivalent area is determined through

$$A_{eq} = \frac{F \times L}{E \times \delta l} \tag{3.2}$$

The calculated area is independent of the assumed modulus of elasticity E and the force F at which the length L corresponds to the values listed in Table 3.2.

The effective moment of inertia is calculated by using the equation of kinetics. The end moments of the single beams in the lattice structures do not have the

Table 3.2.: Geometrical properties of single beams

Cross section shape	Effective beam length [mm]	Area $A_{eq}[mm^2]$	Moment of inertia $I_{eq}[mm^4]$	Radius of inertia $\sqrt{I/A}[mm]$
Large square	4.91	3.82	1.67	0.66
Large Round	5.26	3.83	1.61	0.65
Small square	5.41	2.42	0.80	0.57
Small round	5.66	2.43	0.78	0.57

same value; the shear force is constant over the length of the beam. The moment distribution is simplified by assuming identical end moments at the beam for a given shear force (M_0 Figure 3.10). The end rotation of the beam for a given virtual rotation (leads to a virtual moment distribution M_1) is then

$$\varphi = \int_{L}^{x=0} \frac{M_0(x) \times M_1(x)}{E \times I(x)} \tag{3.3}$$

The variable cross-section is taken into account including the variable moment of inertia $I(x)$. The effective moment of inertia I_{eq} is then calculated by integrating the moment distribution M_0 and M_1 and solving equation 3.3 with respect to I

$$I_{eq} = \frac{M_0 \times M_1}{6 \times E \times \varphi} \times L \tag{3.4}$$

The calculation is independent of the values M_0 and M_1 as well as the modulus of elasticity E. The results for the equivalent area A_{eq} and moment of inertia I_{eq} are listed in Table 3.2.

The normal forces and the shear forces for all elements are calculated with the classical model (Figure 2.6) using the calculated geometrical properties for the global stiffness matrix. The V/N-ratios are independent on the modulus of elasticity. The V/N-ratio distributions in the lattices are illustrated in figure 3.11 for the four different beam shapes where the lattice deformation was set to $0.1mm$. The distributions for the lattices with the large cross-sections (Figure 3.11(a) and 3.11(b)) show some differences. The maximum ratio and the mean ratio over all elements have slightly higher values for the square beams in comparison to the round beams. Based on the smaller beam length (i.e. smaller slenderness) between the nodes ($4.91mm$) of the square beam type compared to the round beams ($5.26mm$), a higher shear force or rather higher end moments with respect to the normal forces are formed. The slenderness is defined as

$$\lambda = L/\sqrt{\frac{I}{A}} \tag{3.5}$$

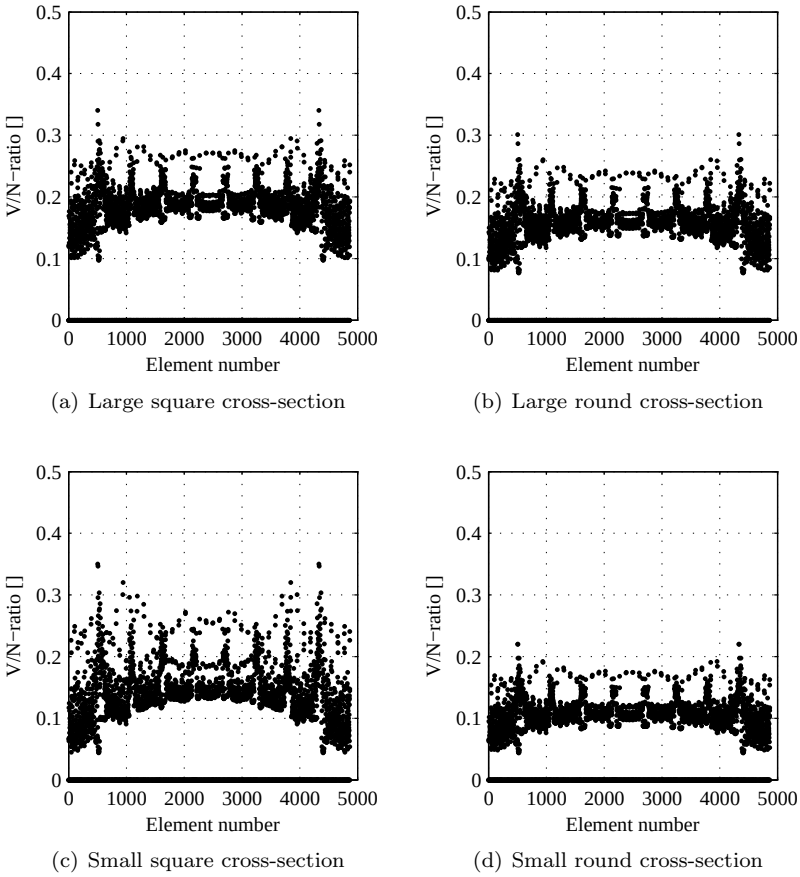

(a) Large square cross-section

(b) Large round cross-section

(c) Small square cross-section

(d) Small round cross-section

Figure 3.11.: Shear/Normal force distribution of single beams in lattice

The radius of inertia $\sqrt{I/A}$ is nearly equal for the large and the small cross-sections. Thus, the beam length between the nodes has the main influence to the slenderness. The influence of the slenderness can be better seen by comparing the V/N-ratio distributions for lattices containing beams with large and small cross-sectional area (Figure 3.11(a) and 3.11(c)). Lattices with small square beams have significantly smaller V/N-ratios than lattices with large square beams due to the higher slenderness. A small difference is also present comparing the two different cross-sectional shapes for the small beams. It is evident at this point of the lattice analysis that the deformation behaviour of the structure is influenced by the single beam slenderness. Using beams with a small slenderness leads to a structure deformation which is more influenced by bending deformations.

Figure 3.12 illustrates the approach used to achieve the desired loading condi-

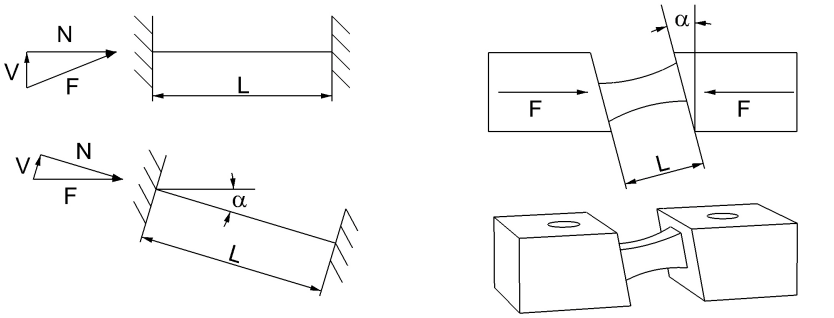

(a) Static system for inclined load (b) Specimen geometry for inclined load

Figure 3.12.: Specimen geometry definition for inclined load cases

tion in the beam. A force F is applied on the beam at a certain angle α. The force F can be split in a shear force part V and a normal force part N with respect to the neutral axis of the beam. The used testing device for single beam elements (described in Chapter 4.2.1) is capable to load the specimens with normal forces. The lateral load is applied by rotating the neutral axis of the beam with respect to the loading direction in the testing device (Figure 3.12(a)). The side view of the specimen geometry (Figure 3.12(b) shows the design of the supports to reach the desired loading case in the beam. The angle α is defined through the V/N-ratio

$$\alpha = \arctan \frac{V}{N} \tag{3.6}$$

Three classes with a different V/N-ratios are investigated for every beam shape to achieve the corresponding force-deformation curves. The first class with a V/N-ratio of 0.2 was chosen due to the fact that the majority of the beams in the global lattice lies in this range. The two other V/N-ratios were selected to 0.4 and 0.6 to respect the behaviour of the beams with a high V/N-ratio. The beams can reach higher V/N-ratios for larger lattice deformations especially when the global lattice has a plastic deformations behaviour. This change in the V/N-ratio distribution will be discussed in detail in Chapter 6.4.1.

4. Micro-mechanical behaviour: Single beams

4.1. Introduction

In order to determine the mechanical properties and the force-deformation curves of the single element beams, a micro-mechanical testing device was developed. The device and the experimental setup will be described in this Chapter. Also the influence of the environmental conditions on the single beam behaviour will be investigated and compared to the effect on the material produced with stereolithography from the literature. The mechanical properties are investigated for the single element beams with different shapes and orientations whereas the specimens were loaded with two different loading rates in order to study the impact on the single beam behaviour. Video image correlation was additionally applied to evaluate the modulus of elasticity of the beams. The force-deformation curves needed for the new model are also presented in this Chapter. Curves of specimens loaded under three different V/N-ratios and two different loading rates are investigated in order to cover the loading conditions which are present in the global lattice structure.

4.2. Testing methods and parameters

4.2.1. Micro mechanical testing device and test setup

A testing device was constructed to measure the beam behaviour under tensile and compressive load for specimens with size in the millimetre range. The development was done to respect the size and the maximum capable force of the specimens. Forces up to $100N$ were expected for the tests in tension and a load cell with an appropriate capacity was chosen. Figure 4.1 illustrates the construction of the testing device. It consists of a stepper motor from *Faulhaber* with a maximal torque of $1.2mNm$ where a gear $(1:1024)$ is mounted. The motor moves a cross beam along two ball screw spindles from *Eichenberger Gewinde* which have an efficiency of more than 80% transmitting the force in contrast to normal threaded rods which have an efficiency less than 25%. The load cell from MTS with a capacity of $\pm 200N$ is placed opposite to the cross beam. The frame of the whole construction consists of stainless steel to prevent corrosion and has a high stiffness to minimise the deformations of the loading stage during the experiment which can influence the measured deformation. A displacement transducer (LVDT) from

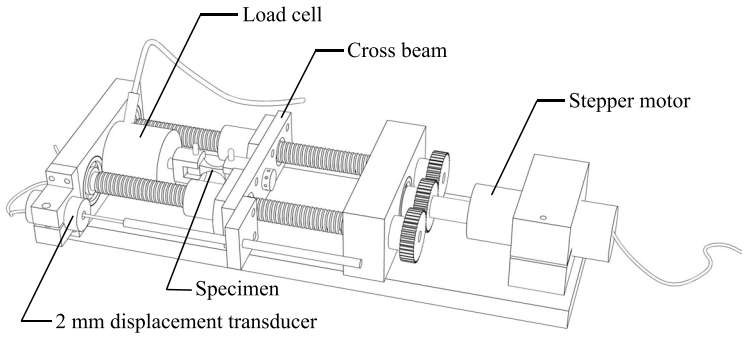

Figure 4.1.: Micro-mechanical testing device

HBM with a range of $\pm 1mm$ is used to measure the displacement of the cross beam which corresponds to the deformation of the specimen in the testing device. The small range of the LVDT was chosen to have a high precision measuring in the elastic range of the specimen. The specimens are fixed to the supports using dowel pins that fit into the supports, which are mounted to the cross-beam and the load cell, as can be seen from Figure 4.1. The stepper motor is capable to load the specimens with a loading rate up to $20\mu m/s$.

Figure 4.2 shows the test setup for the single element tests. The load cell and the LVDT are connected to a signal amplifier $HGCplus$ from HBM which converts the signal from the measuring device to an analogue signal. This signal is converted to a digital signal processed by computer that stores the data. The used software is written with $Labview$. The computer also controls the motor encoder which sends the desired electrical impulses to the motor. The VIC system from $Limess$ consists of two cameras ($Pike\ F421B$) with a resolution of 2048×2048 pixels which are connected to a trigger box. This signal ensures that both pictures are collected at exactly the same time. Using a software trigger with a smaller accuracy leads to imprecision during the correlation. The cameras are also connected to a computer, which records and stores the pictures using the software $VICSnap$. The system is capable of recording the specimen surface with a picture rate of $5Mhz$. The force signal from the HBM amplifier is also recorded by the system used for the video image correlation to synchronise the collected pictures with the force-deformation measurement.

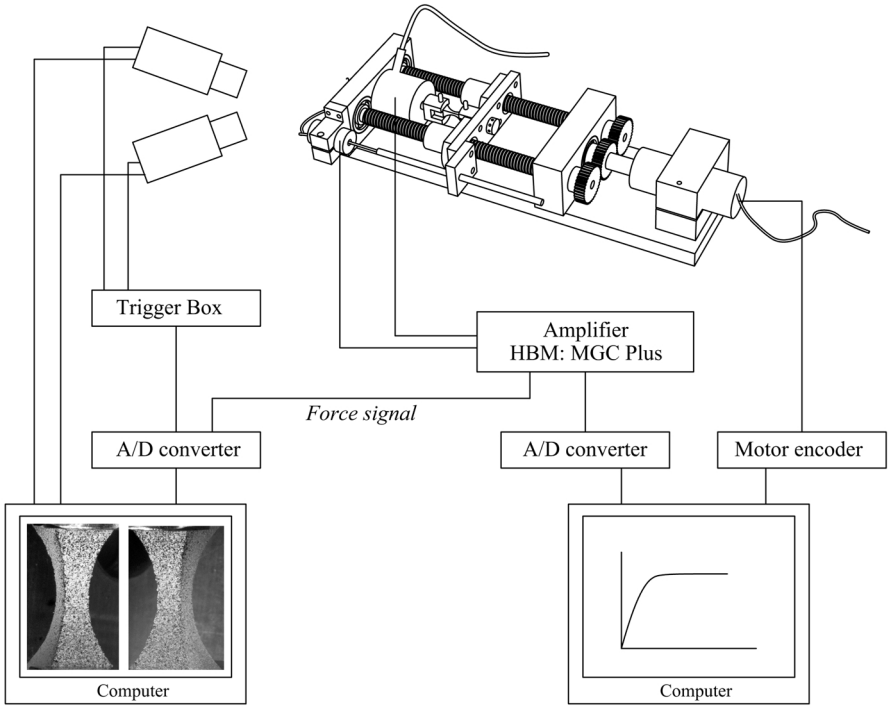

Figure 4.2.: Overview of the Micro-mechanical test setup

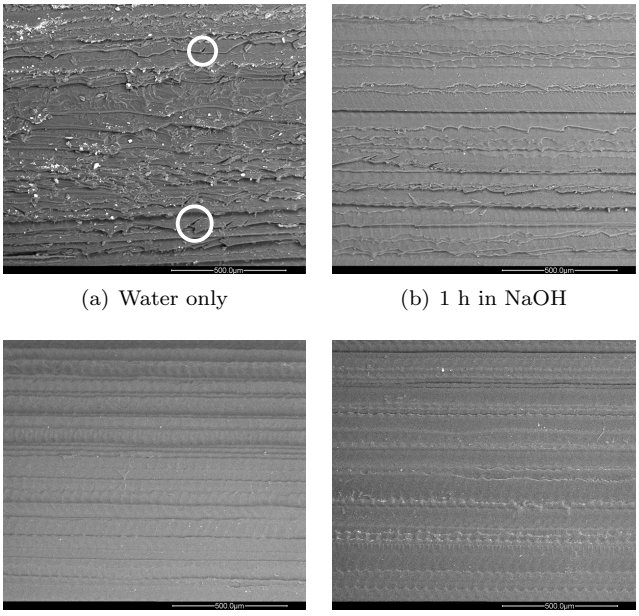

(a) Water only (b) 1 h in NaOH

(c) 3 h in NaOH (d) 6 h in NaOH

Figure 4.3.: ESEM picturs of specimen surface for different treatment times in a $NaOH$ solution

4.2.2. Environmental effects on the single beam behaviour

The preparation and the storage condition of the material until testing was controlled in order to reach the same mechanical behaviour of the produced parts in the single beam elements and the global lattice structure.

The preparation of the specimens consists of cleaning the cured parts from the support material as described in Chapter 3.3. The cleaning was done using a water jet for lattice structures or by hand for single beam elements using the dulled side of a cutter. Pictures of the specimen were made with an Environmental Scanning Electron Microscope (ESEM) to investigate the surface properties after the cleaning process. Figure 4.3(a) shows that the surface is not fully cleaned from the support material and has rough layer borders as well as small cracks in the layers (indicated with circles in Figure 4.3(a)). It was decided to treat the specimens in a 4% sodium hydroxide solution to dissolve the support material and to grind the layer borders. Figure 4.3(b)-4.3(d) illustrate the surface of the specimen for different treatment time in the solution. A treatment for one hour solves the remaining support material but leads to a minor change of the layer border quality. Extending the treatment to three hours produces a smooth border of the layers where no cracks are visible any more due to dissolving of material

residue. The surface starts to show some grooves at this stage of treatment. The grooves occur since the jetting heads of the printer release droplets of the material which immediately hardens until they move on. This production method induces the rugged border and surface of the layers. The characteristic becomes more evident by extending the treatment to six hours. Figure 4.3(d) shows many grooves at the border layers because more hardened material was dissolved. Also gaps between two layers are now visible due to dissolution of the weaker intersection layer material compared with the layer material which can lead to a delamination effect. From these experiments, it was decided to treat the specimens for three hours in the $NaOH$ solution, at which time it was assumed that the specimens were fully cleaned from the support material and rough borders were eliminated. Moreover, a degradation of the material by delamination effect was minimal after this treatment.

The environmental conditions (humidity and temperature) have a large impact on the mechanical properties of the specimens produced by Polyjet technology. The impact of the change in storing temperature and humidity and the storing time was investigated for parts produced by stereolithography. Liu and Jiang (2003) studied the influence of the environmental temperature and humidity on the change of sample dimensions. The effects of ageing in different environments were investigated by Ottemer and Colton (2002), where they stored the samples in different moisture environments at a constant temperature. They recognized a decrease in mechanical properties for specimens exposed at high humidity environments and an increase for specimens exposed at low humidity during a storage time of about 400 hours. Scheirs (2000) studied the influence of the exposure to stray light on the mechanical properties of material parts. A statistical DOE (design of experiments) approach was carried out by Puebla et al (2012) considering the build orientations as well as the effects of ageing and pre-conditioning. The environmental condition according to ASTM D638 (2008) is used to determine the mechanical properties of polymer part fabricated with rapid prototyping. It prescribes the storing conditions to an environmental temperature of 20° with a humidity of 50%. The storing time is not defined. Equivalent studies for specimens produced with the Polyjet technology have not been conducted until now. Consequently, the influence of the environmental temperature and humidity is investigated in order to detect changes in mechanical behaviour and to clearly define the storage conditions for the single element specimens and the lattice structures.

Figure 4.4 shows the influence of storing the specimens at different moisture environments at the same temperature of 20° for 7 days. Four specimens with the same storing condition were tested and representative curves are shown in Figure 4.4. Specimens with large square cross-sections were tested for two different orientations. It is obvious that the storing humidity has a huge influence on the single beam behaviour for both orientations. The loading curves present a descending maximum force while the humidity increases. The curve gradient

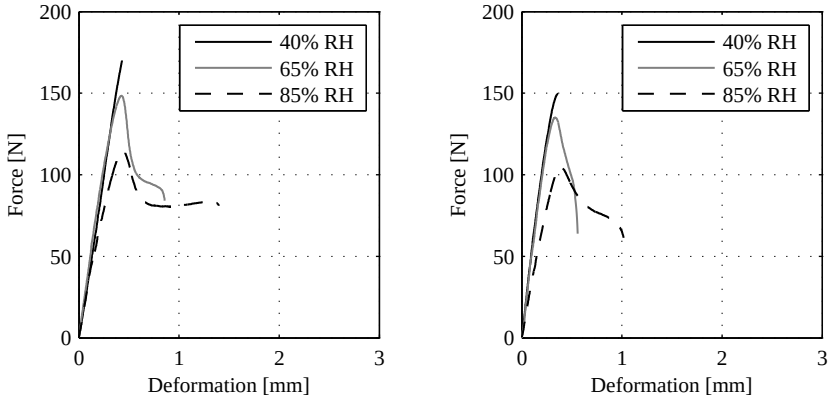

(a) Beam orientation 0°/0° (b) Beam orientation 30°/55°

Figure 4.4.: Loading curves for specimens stored in different moisture environments at a constant temperature of 20° for 7 days

keeps the same value for specimens stored at 40% and 65% RH. Also the maximum force is only slightly reduced between these two environments and the force drop after the maximum indicates a brittle behaviour of the specimen. Increasing the relative humidity to 85% leads to a more obvious reduction of the maximum force and a reduction in the curve gradient, whereas the reduction in the curve gradient is more distinct for element with orientation 30°/55° than for elements with orientation 0°/0°. A higher ultimate displacement is reached for this specimen, which indicates a more plastic behaviour of the specimen stored at 85% RH which was also observed by Bolon et al (1980) for UV-cured polymers.

The observations agree with the study from Ottemer and Colton (2002) where a decrease in mechanical properties of specimens produced by SL, while increasing the environmental humidity, was observed. They also found a difference in the modulus of elasticity measured on specimens stored at low RH (0% and 45%) for 7 days. This change is not present for the current material type between 40% and 65% RH. Ottemer and Colton (2002) determined the mechanical properties on specimens according to ASTM D638 (2008), which have larger dimensions than those used here. Also the used material differs due to the different print process and the selected RH's range. This may explain the difference in the results.

The influence of the storage time respectively ageing on the specimens exposed at 85% RH is illustrated in Figure 4.5. The moisture absorption of the specimens was measured through determination of the weight over a period of 22 days (Figure 4.5(a)). An increase in weight is observed during the first 12 days while the weight stays constant for the rest of the time. The increase in weight indicates that the specimens absorb humidity from the environment which gets bound in

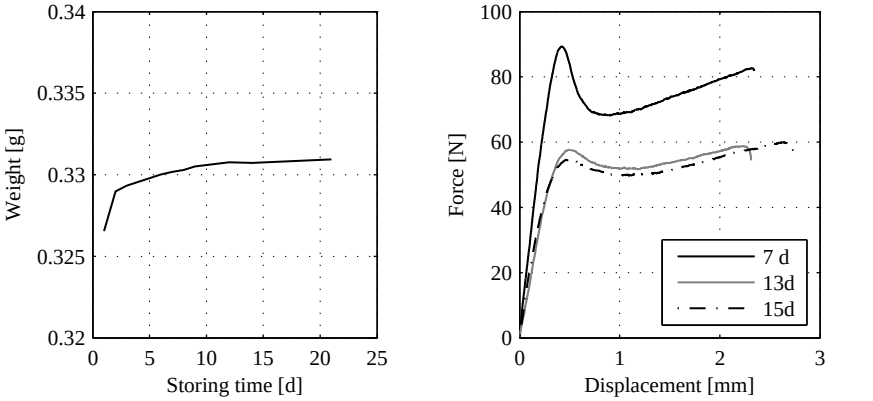

(a) Weight change

(b) Loading curves for different storage times

Figure 4.5.: Influence of the storage time on the mechanical behaviour of single beam elements

the specimen as water. The humidity absorption has an influence on the loading curves, as shown in Figure 4.5(b). It is obvious that the mechanical properties, the curve gradient and the maximum force decrease while increasing the storing time. Only slight to negligible changes are observed for specimens stored between 13 and 15 days. The ultimate displacement gives no indication of any property change due to the high scatter of this value.

Ottemer and Colton (2002) also noticed this behaviour of the investigated polymer parts fabricated with SL on the ageing. They measured the moisture uptake for different polymer types until the weight change was less than 1 per cent of the total weight. The time to reach the saturation depends on the used polymer type. The main absorption and the main decrease of the mechanical properties took place in the first 12 days of storage. Only slight changes of the mechanical properties were recognized until a storing time of 7 weeks.

The investigated influences on specimens produced with the PolyJet technique show the same effects on the mechanical behaviour on specimens produced with SL due to the application of a similar acrylic photopolymer as a part material in both cases. In the end, it was decided that all specimens were to be stored in a controlled environment (20° temperature and 85% RH) for 14 days before testing to reach a ductile behaviour of the material and to have a clearly defined environment which leads to a small scatter in results.

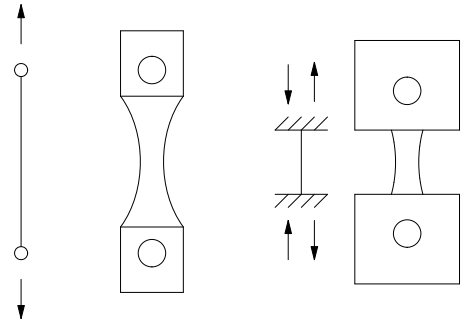

Figure 4.6.: Different boundary conditions for single element experiments

4.2.3. Testing series

The micro-mechanical behaviour of single beam elements was investigated to evaluate the parameters for the classical model approach (modulus of elasticity E_{beam}, yield stress f_{pl} and maximum deformation $\delta_{max,beam}$). The specimens were loaded as shown in Figure 4.6(a) which corresponds to the classical tensile test where the support parts can freely rotate to avoid bending moments in the specimen which can lead to a erroneous calculation of the mechanical parameters.

Four specimens were tested for every different beam shape respectively cross-sectional geometry described in Chapter 3.3. Two different loading rates of the specimens were selected to investigate this influence on the mechanical single beam properties. The variation of the loading rate respects the certainty that the lattice structure may not deform uniformly which leads to different loading rates of every layer in the structure.

The evaluation of the force-deformation curve used for the new approach model was done on the specimens described in Chapter 3.4. Three different classes were tested whereas the specimen geometry respects the V/N-ratio of the elements in the lattice structure. The force-deformation curves were measured for tensile and compressive load with fixed ends which correspond to the loading condition case in Figure 4.6(b). The above-mentioned variation of the loading rate was also investigated in this testing series.

All measured curves in tension and compression show a contact effect at the beginning due to the alignment of the specimen in the testing machine and the use of dowel pins to connect the specimens with the supports. The zero point of the curves was therefore corrected according to ASTM D638 (2008) for a correct calculation of the modulus of elasticity E_{beam}.

4.3. Input parameters for the classical model

The results for uniaxial tensile tests on single beam elements are discussed in this Chapter. The tests were necessary for obtaining the input parameters for the classical model (modulus of elasticity E_{beam}, yield stress f_{pl} and maximum deformation $\delta_{max,beam}$). The procedure to calculate the modulus of elasticity using $VIC3D$ is discussed in detail.

Uniaxial tension tests were performed for the different geometries and build orientations. Figure 4.7 shows typical force-deformation curves for large square beams with different orientations and a loading rate of $15\mu m/s$. The curves for the other three specimen geometries are listed in Appendix B.1. The beam orientation regarding to the print direction i.e. the beam position in the lattice structure is shown in the inset. The grey area represents the envelope of the four measured curves done in a single testing series.

It can be seen from Figures 4.7(a)-4.7(d) that the scatter in the ascending part of the curves is small. The curves show nearly linear-elastic behaviour until the maximum forces are reached. The force drops down for beams with orientations $0°/0°$ and $0°/60°$ i.e. which are laying in the x-y-plane (in-plane orientation). The force then starts to increase again at a certain point until the beam breaks in a brittle fashion. The force-deformation curves for these two orientations correspond to the behaviour of various thermoplastics like polypropylene (PP) or high density polyethylene (HDPE) (Kontou and Farasoglou (1998) and G'sell and Jonas (1979)). No decrease of the force after the initial peak can be found for beams with orientations $30°/55°$ and $90°/55°$ (out-of-plane orientation). The force declines slightly after the maximum force is reached. The beams then also break in a brittle manner. The highest scatter is observed for the deformations when the specimen breaks brittle. The influence of the build orientations on the maximum force is clearly visible. Specimens parallel to the print orientation reach the highest forces, whereas the out-of-plane specimens reach the lowest forces. The values have a high difference in the magnitude. The build orientation must therefore be taken into account in the simulations.

The yield stress f_{pl} was determined by dividing the yield force through the cross-sectional area in the middle of the beam. The areas for the large cross-sectional shapes are the same as well as for the small cross-sectional shapes. Figure 4.8 illustrates the yield stress for every tested series and for the two different loading rates.

The influence of the loading rate on the yield stress f_{pl} is obvious for all specimen geometries. The difference in the values varies from 30% for the in-plane specimens up to 60% for the out-of-plane specimens. This characteristic is typical for thermoplastics. Increasing the loading rate leads to higher yield stresses. A simple material model can be used for this type of material to describe the viscoelastic material behaviour. The Kelvin-Voigt model is appropriate to capture the

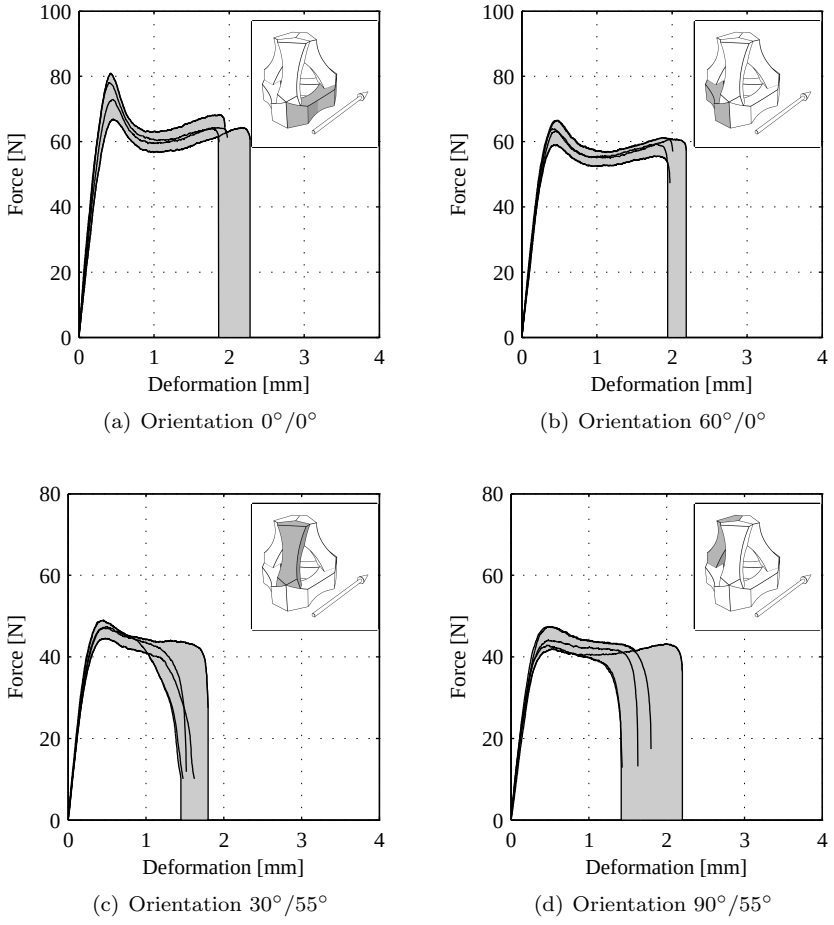

(a) Orientation 0°/0°

(b) Orientation 60°/0°

(c) Orientation 30°/55°

(d) Orientation 90°/55°

Figure 4.7.: Load curves in tension for different beam orientations with large square cross-section and loading rate of $15\mu m/s$

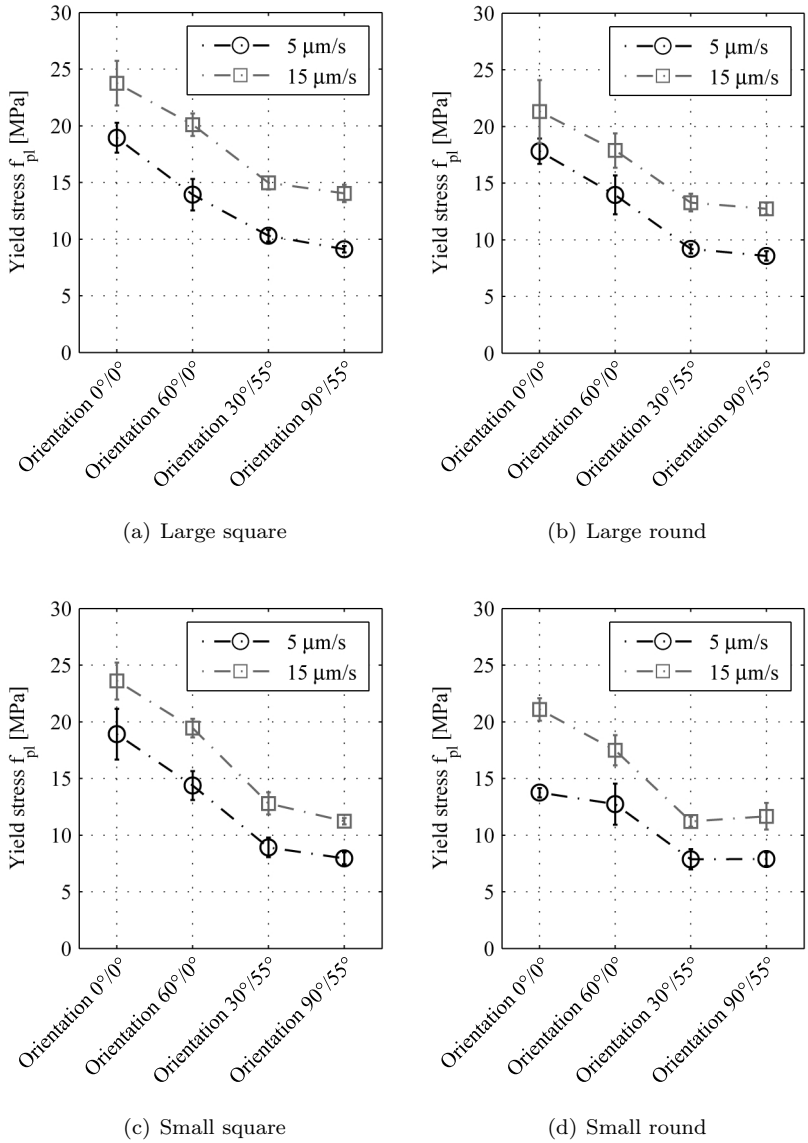

(a) Large square

(b) Large round

(c) Small square

(d) Small round

Figure 4.8.: Yield stress distribution for all cross-sectional geometries depending on the specimen orientation tested in tension

main influences of the material behaviour. The model is described through

$$\sigma(t) = E \cdot \epsilon(t) + \eta \cdot \frac{d\epsilon(t)}{dt} \tag{4.1}$$

where η is the viscosity and $d\epsilon(t)/dt$ refers to the loading rate. The modulus of elasticity E and the viscosity η are specific material parameters whereas the stress at a certain strain level can vary dependent on the loading rate i.e. the strain rate. The specific material parameters E and η are different for the four orientations due to the layered production process. The influence of the loading rate in the model corresponds to the observations of the test results. The information of the strain rate dependency is fruitful for comparing the global lattice experiments with the simulations.

The influence of the orientation is clearly visible for all geometries. The highest yield stresses are reached for the specimen with orientation $0°/0°$. Changing the in-plane angle to $60°/0°$ leads to a decrease of the yield stress of about 20% for all specimens. Specimens which are printed in the out-of-plane orientation have a significantly lower yield stress compared to the in-plane specimens where the difference can reach up to 100%. The stress keeps nearly the same value for both out-of-plane orientations where it is independent of the variable in-plane orientation. Dulieu-Barton and Fulton (2000) observed negligible change of the yield stress between specimens produced with stereolithography with orientations $0°/0°$ and $90°/0°$. A change of 13% was determined between the orientations $0°/0°$ and $0°/90°$. Hague et al (2004) and Quintana et al (2010) observed only slightly changes of the material properties of less than 5% for specimens produced with stereolithography.

Some factors have to be mentioned to describe the observed differences in the measured yield stresses depending on the build orientation. Former researchers used stereolithography for the specimen production whereas Jetted photopolymer technique is used in this thesis. This leads to a variation in the material properties due to the different production processes and the used liquid resin. The aforementioned researchers stored the specimens in a controlled environment of 50% RH and 20° C whereas the specimens in the present study were stored at 85% RH and 20° C. The storing humidity has an influence on the yield stress which was shown in Chapter 4.2.2. Another factor which can lead to differences in the observations is the specimen size. In the mentioned studies, specimens were produced according to ASTM D638 (2008), which have a cross-sectional area of about $50.0mm^2$ in contrary to areas of $3.1mm^2$ respectively $1.8mm^2$ used in this thesis. This decides whether the material can be handled as being isotropic or anisotropic. Hague et al (2004) proposed to consider the material parts produced with stereolithogarphy as isotropic. The tested material in this work for the specific specimen geometry shows an anisotropy which is not negligible. The anisotropy results from the layered production method. The in-plane strength of one layer seems to be higher than the bond between two layers.

The cross-sectional shape and area have an influence on the yield stress. It has nearly the same value for large and small cross-sectional areas for the testing

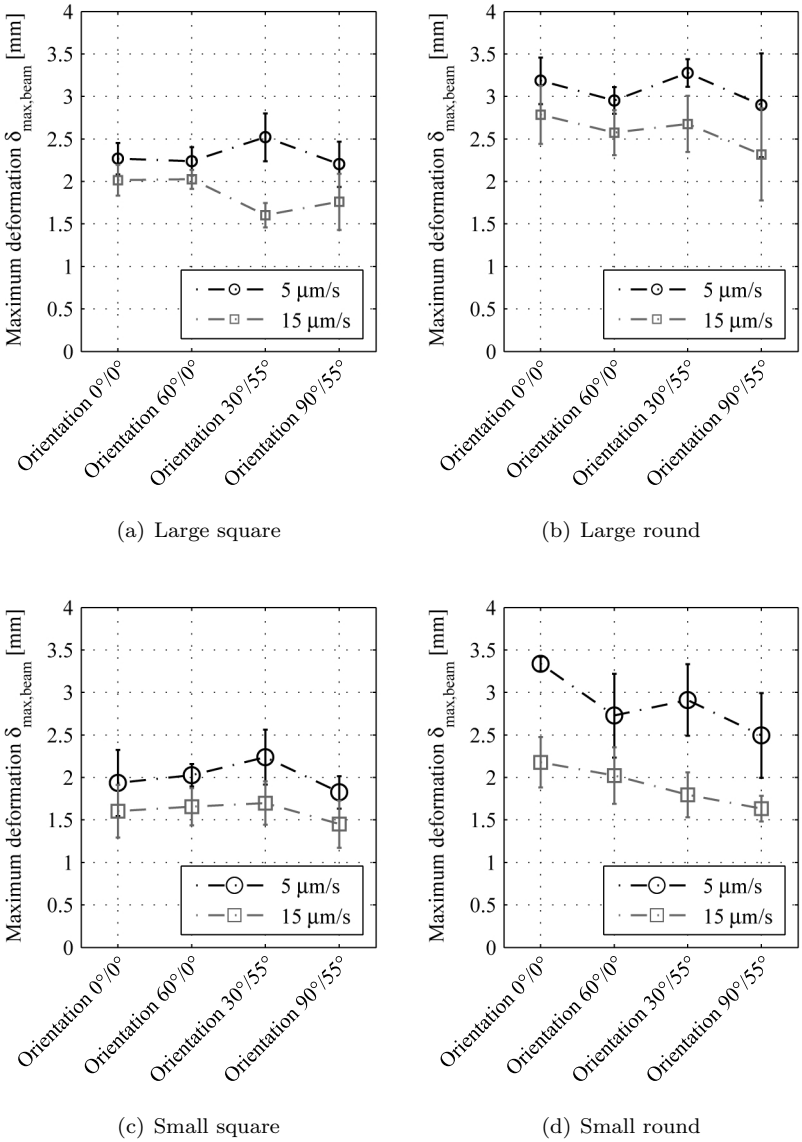

(a) Large square

(b) Large round

(c) Small square

(d) Small round

Figure 4.9.: Maximum deformation distribution for all cross-sectional geometries depending on the specimen orientation tested in tension

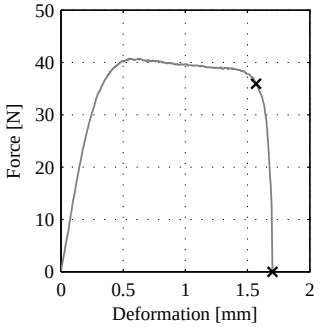

(a) Load curve

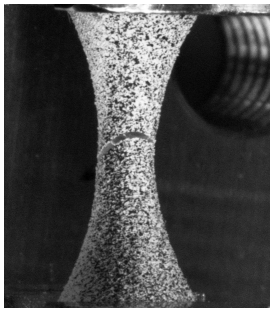

(b) Large round 90°/55° crack initiation

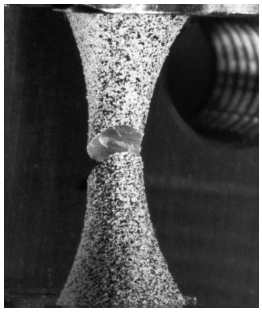

(c) Large round 90°/55° crack orientation

Figure 4.10.: Crack growth and orientation for specimen loaded in tension; crosses indicate the location of the captured pictures

series with orientations 0°/0° and 60°/0° for both square and round shapes. No size effect can be observed by varying the middle area for in-plane oriented specimens. A size effect exists for specimens with orientations 30°/55° and 90°/55°. The yield stress decreases by reducing the cross-sectional area for the out-of-plane specimens. This observation is made for both square and round shapes. Specimens with a square cross-sectional shape have always a higher yield stress than the corresponding specimens with a round cross-sectional shape. Thus, the shape and size effect at this scale of material testing is not negligible and has to be taken into account in the simulations by applying the corresponding yield stresses for the different beam geometries.

Figure 4.9 illustrates the variation of the maximum reachable deformation $\delta_{max,beam}$ when the specimen breaks. It is obvious that in the series with a loading rate of $5\mu m/s$ a higher maximum deformation is reached than in the series with a higher loading rate. Specimens with a square cross-sectional shape break at a lower deformation than the corresponding specimens with a round cross-sectional shape. The geometry of the support structures has to be considered here. The geometry differs for both shapes. The support structure for the round shaped specimens has a smaller cross-sectional area than the square shaped support (see Figure 3.4). This leads to higher strains in the supports during the test which is measured by the LVDT. Thus, this observation cannot be explained only with a shape effect but there is a tendency that the round beams have a higher deformation capacity before they fail in a brittle manner . A clear tendency of the deformation dependency on the build orientation cannot be established. The maximum deformations keep nearly the same value for all orientations, contrary to the yield stresses which varies much more. A size effect is slightly present because only a small reduction of the displacements can be observed from the large to the small cross-sectional geometries.

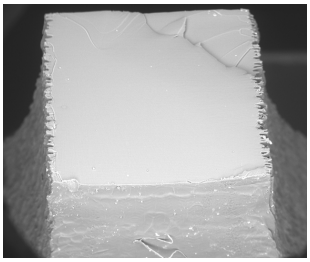

Figure 4.11.: Crack surface of a specimen with orientation $0°/0°$

Figure 4.10 shows a typical crack process of a single beam in tension. The pictures were registered on a beam with large round cross-sectional area and an orientation of $90°/55°$. The crack initiation starts at one side of the specimen when the maximum deformation of the plastic plateau is reached i.e before the rapid decrease of the force (Figure 4.10(b)). Figure 4.10(c) illustrates the crack direction when the specimen is fully broken. It is obvious that the crack is not positioned in the middle of the beam and the orientation of the crack is not perpendicular to the loading direction. The crack occurs between two printing layers which imply that the bond between two layers has a weaker strength than the one in-plane layer itself. The anisotropic behaviour of the material observed from the yield stress characteristics is then obvious when studying the crack patterns.

ESEM pictures of the cracked surface were taken to assess the brittle fracture behaviour. Figure 4.11 shows a crack surface on a beam with large square cross-sectional area and an orientation of $0°/0°$. The surface is planar and shows no dimple patterns which would indicate plastic fracture. Dimple crack patterns are visible on fracture surfaces of steel or plastic with a ductile behaviour. This observation confirms the brittle fracture behaviour of the specimens which was already mentioned from the force-deformation curves.

Evaluation of the modulus of elasticity

The modulus of elasticity cannot be calculated directly from the measured force-displacement curves for different reasons. The measured deformation takes also the deformation of the testing device and the support parts into account while the cross-section of the specimen between the supports is not constant. Therefore, the required strain values were measured by means of video image correlation.

The surface deformations of the specimens were recorded with both cameras during the experiments. An area of $40 \times 40mm$ was examined. Objectives from $Schneider - Kreuznach$ ($Makro - Extension$) with a focal length of $42mm$ were selected to achieve an appropriate resolution of the deformation field. Figure 4.12 illustrates one of the recorded pictures. The deformation and the strain calculation were performed over the bright areas in the figure. The bright areas indicate high strains and dark areas indicate low strains on the surface of the specimen. The

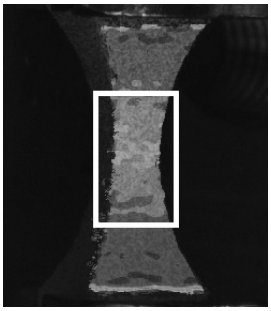

Figure 4.12.: Recorded Picture for video image correlation with marked area for the strain calculation

mean value of the strain was determined over the area within the box shown in Figure 4.12. The height of the box corresponds to the length listed in Table 3.2 to respect the assumption of rigid nodal areas and the variable cross-section over the length. The modulus of elasticity is then calculated through

$$E = \frac{\delta\sigma}{\delta\epsilon} \tag{4.2}$$

and the stress and strain are defined by

$$\sigma = \frac{F}{A_{eq}} \text{ and } \epsilon = \frac{L}{L_0} \tag{4.3}$$

where L is the measured length of the LVDT. The determination of L_0 will be described further on in this Chapter.

The stress is assigned by dividing the force over the equivalent area A_{eq} listed in Table 3.2 which takes the irregular stress distribution over the considered length of the specimen into account.

Figure 4.13(a) shows the stress-strain curve measured with VIC 3D. It is obvious that the used polymeric material behaves as a visco-elastic material which leads to a non-linear elastic behaviour in the ascending part of the curve. DIN EN ISO 527-1 (2012) specifies the strain levels at which the secant modulus of elasticity has to be calculated. The strain levels are set to $\epsilon_1 = 0.05\%$ and $\epsilon_2 = 0.25\%$. Applying these levels to calculate the secant modulus on the developed material leads to an overestimation of the material stiffness due to the soft deformation behaviour. ASTM D638 (2008) contains advices to calculate the secant modulus for materials with no linear regions whereby stress levels are defined instead of strain levels. The calculation of the secant modulus through defining stress levels was chosen in this thesis due to the application of different specimen shapes and loading rates contrary to DIN EN ISO 527-1 (2012) and DIN 53504 (2009).The distribution of the secant modulus of elasticiy in subjection to the stress level is illustrated in Figure 4.13(b). The non-linear trend is clearly visible which is

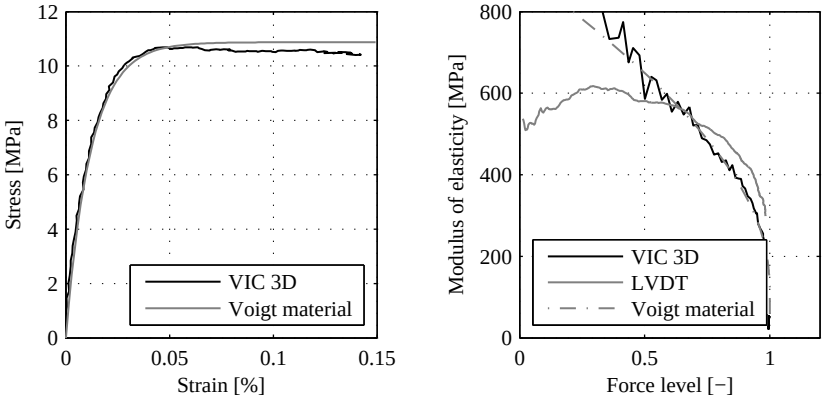

(a) Measured strain with VIC 3D (b) Modulus of elasticity gradient

Figure 4.13.: VIC 3D measurement for modulus of elasticity calculation

Table 4.1.: Different values for the initial length dependent of the specimen shape

	Tension	
	Large	Small
Square	11.5	10.0
Round	12.0	11.0

characteristic for a visco-elastic material. The secant modulus in this thesis was determined using the stress and the strain values at stress levels of 0% and 60% relating to the maximal stress due to preserve a mean value i.e. not to over- or underestimate the secant modulus of elasticity for the use in the simulation.

The measured force-deformation curves were converted to stress-strain curves using the equivalent area A_{eq} and a certain initial length L_0. The initial length L_0 was determined empirically because the influence of the support deformation and the deformation of the beam sections outside the investigated equivalent length cannot be calculated directly due to the visco-elastic material behaviour and the unknown stress distribution in the support structures. The initial length L_0 was chosen that the curve of the VIC-analysis and the curve of the measurement with the LVDT intersect at a stress level of 60% (Figure 4.13(b)). Figure 4.13(b) also illustrates the calculated distribution of the modulus of elasticity as a function of the stress level. The visco-elastic material behaviour cannot be detected for the experiments with the measurement of the LVDT because the support deformations and the non-constant specimen shape over the length distort the real material behaviour .

Four different initial lengths L_0 could be calculated. Two main observations are

obvious. The initial length L_0 is smaller for specimens with square cross-sectional areas than with round areas. The reason for the determination of the different lengths is that the support structure of the round beams has a larger deformation during the test as mentioned before, which leads to a larger deformation measurement of the LVDT. Thereby, the initial length L_0 has to be higher for round shapes than for square shapes to calculate the correct strain over the observed specimen length. This fact agrees with the observation that the initial length is smaller for small cross-sectional areas than for large areas due to the fact that the specimen has a smaller deformation outside the observed length of the specimen for small middle areas. It can be said that the smaller the initial length is, the smaller are the deformations of the specimen outside the observed area i.e of the support structures.

Figure 4.14 shows the determined modulus of elasticity for all specimen shapes and orientations. The same trends are obvious as seen before when discussing the results of the yield stress measurements. Specimens tested with a small loading rate show a smaller modulus of elasticity than with a larger loading rate. The differences vary between 20% for the in-plane specimens and 30% for the out-of-plane specimens. This change in the modulus is also a characteristic of thermoplastics. An increase of the loading rate leads to a higher modulus of elasticity, independent at which stress or strain levels the modulus is calculated. The difference in the modulus of elasticity, dependent on the build orientation, is also clearly visible from the diagrams. Specimens with an orientation of $0°/0°$ have the highest modulus whereas a change in the in-plane orientation to $60°/0°$ leads to smaller values. Specimens which are printed in the out-of-plane orientation show also smaller modulus of elasticity than the in-plane specimens whereas the values of both orientations $30°/55°$ and $90°/55°$ are nearly the same.

A shape effect is visible for the in-plane specimens. Specimens with square cross-sectional areas have higher modulus of elasticity than with round areas for both orientations $0°/0°$ and $60°/0°$. This effect is only slightly present for out-of-plane specimens with large areas whereas for small areas, no significant change in the value can be observed. The modulus of elasticity lies in the range of $400 - 500$ MPa for all out-of-plane specimens and the scatter in the measurements can be up to 20% which relativises the shape effect for this specimens. The existence of the shape effects for in-plane specimens i.e. beams with square cross-sectional areas have higher modulus of elasticity than with round areas proves the observation that beams with square shape have smaller deformations until they fail comparing with the round shape. The square beams have a more rigid behaviour than the round beams which leads to a smaller deformation capacity until failure. This observation shows that the influence of the support structure to the ultimate deformation at failure is small as mentioned before.

A size effect can be observed by comparing values of specimens with large and small cross-sectional areas. Specimens with a small area and in-plane orientations $0°/0°$ and $60°/0°$ have a higher modulus of elasticity than specimens with large areas. This effect is not present for out-of-plane specimens.

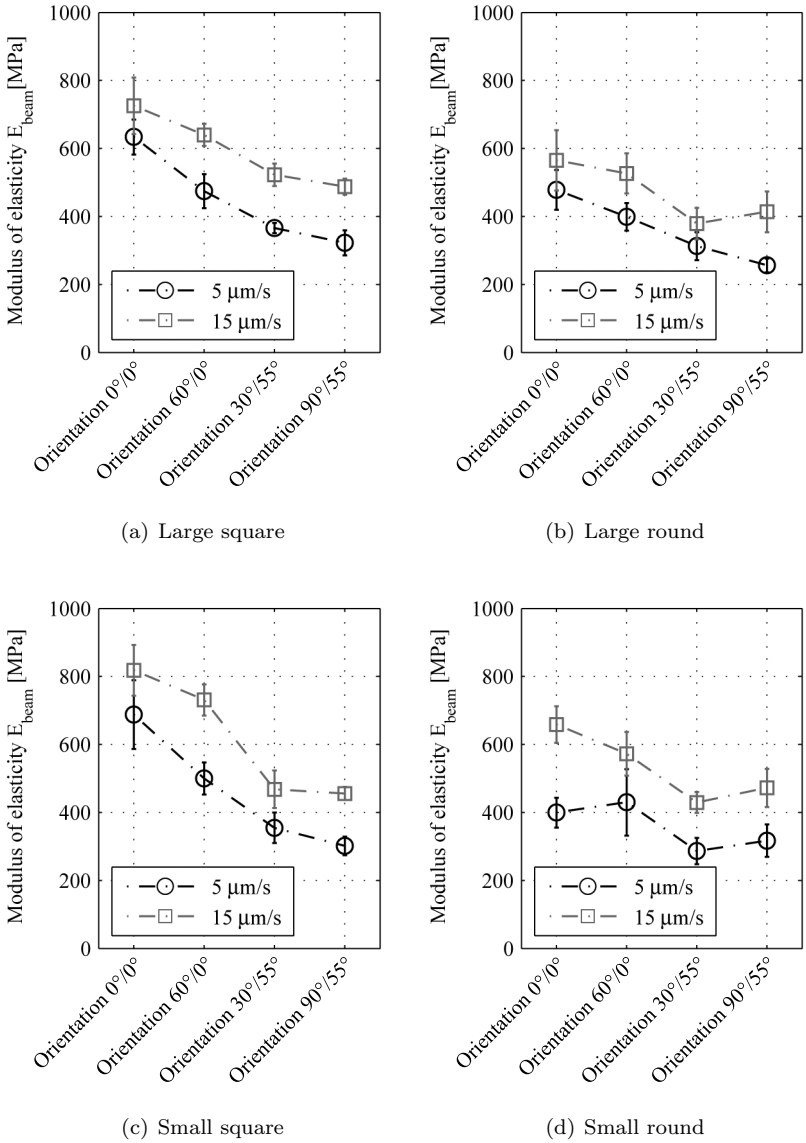

(a) Large square

(b) Large round

(c) Small square

(d) Small round

Figure 4.14.: Modulus of elasticity distribution for all cross-sectional geometries depending on the specimen orientation tested in tension

4.4. Input parameters for the new model

Tensile and compressive tests on single beam elements with different V/N-ratios and two different loading rates were performed in order to determine the input data i.e. the force-deformation curves for the new model approach. The geometries of the specimens are described in Chapter 3.4. The presented curves in this Chapter are generated by calculating the mean curve from four experiments. The curves are measured on specimens with an orientation of 30°/55°. The force-deformation curves for specimens with orientation 90°/55° can be found in Appendix B.2. The curves and the tendencies show no differences regarding to the curves for specimen with the presented orientation 30°/55°.

Figure 4.15 shows the measured curves for all four specimen geometries in tension for V/N-ratios of $0.0, 0.2, 0.4$ and 0.6. The experiments were performed on specimens with an orientation of 30°/55° and a loading rate of $15\mu m/s$. The force-deformation curves with a V/N-ratio of zero derive from the experiments for the classical model described in the previous Section.

It is clearly visible from the diagrams that the beam elements have the same deformation behaviour for all V/N-ratios. The stiffness in the elastic range is only slightly influenced by changing the V/N-ratio. Also the yield force is in the same range for the ratios of 0.0 and 0.2 for all beam shapes. No tendency is present whether the specimens with a high or low V/N-ratio reach a higher deformation. The observation, that the deformation behaviour of the elements in tension is not affected by the magnitude of the end moments i.e. the V/N-ratio between 0.0 and 0.2, is in agreement with the fact that the second order effect under tension has a minor influence on the deformation behaviour of a system. The second order effect causes a reduction of the end moments under tensile load and the system acts nearly the same way like under pure tensile load conditions. The system or specimen is stabilized when loaded under tension.

Differences are visible for the yield force for all elements which were loaded with a V/N-ratio of 0.4 and 0.6. They have about 50% higher values than specimens loaded with ratios of 0.0 and 0.2. These differences can be explained from the fact that the end moments for the specimens are higher with a V/N-ratio of 0.4 and 0.6. The higher end moments lead to a higher strain rate in the outer fibres of the beam cross-sections which leads to a higher strength in these fibres for visco-elastic materials. The higher strength increases the cross-sectional loading capacity and the measured yield force also increases. This effect is present for all beam geometries. The specimens tested with a V/N-ratio of 0.4 and 0.6 have higher forces over the whole length of the deformation compares with the specimens tested with a V/N-ratio of 0.0 and 0.2 until they break brittle.

Figure 4.17 shows the measured curves for large square and round specimen geometries in compression for V/N-ratios of $0.2, 0.4$ and 0.6. The experiments were performed on specimens with an orientation of 30°/55° and loading rates of $5\mu m/s$ and $15\mu m/s$.

It is visible that the V/N-ratio has no influence on the stiffness in the elastic range for specimens with large cross-sections and two different loading rates. The

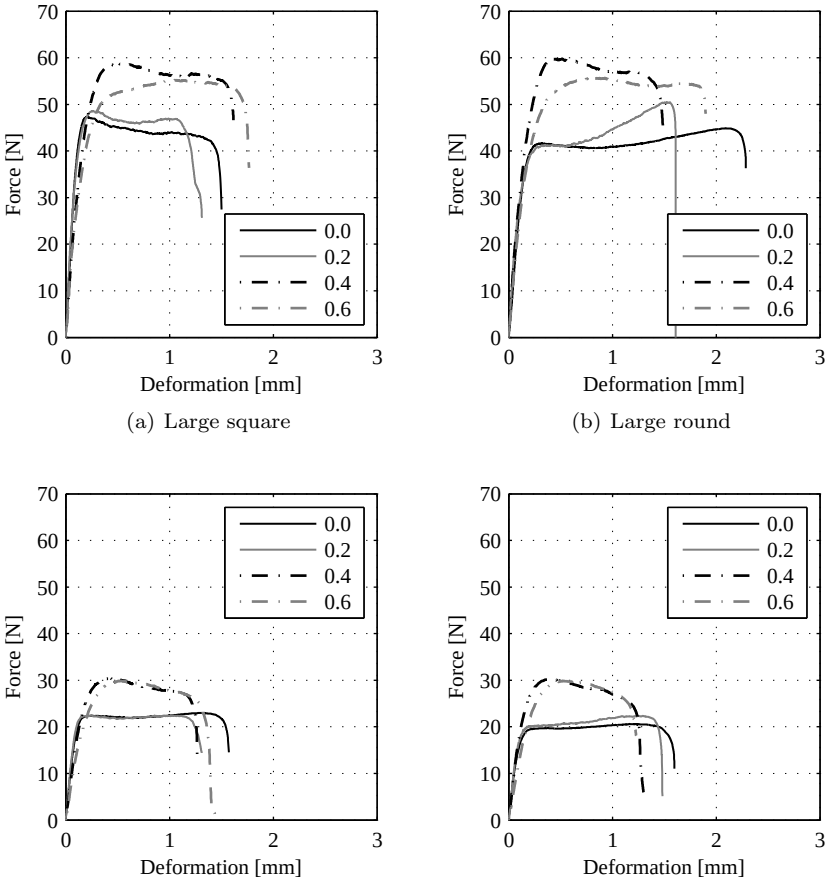

(a) Large square (b) Large round

(c) Small square (d) Small round

Figure 4.15.: Force-deformation curves for specimens with different V/N-ratios and orientation of 30°/55° and a loading rate of $15\mu m/s$ tested in tension

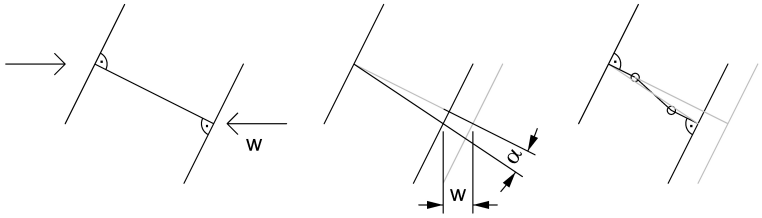

Figure 4.16.: Deformation behaviour of specimens during compressive test: (a) initial state, (b) after the elastic regime, (c) start of non-linear regime

force in the curves, where the linear elastic regime ends, is not influenced by the different V/N-ratios for specimens compressed with a loading rate of $5\mu m/s$ (Figure 4.17(a) and 4.17(b)). However, the load is influenced by the loading rate for ratios of 0.2 and 0.4 where specimens with higher loading rates reach higher loads. Specimens with a ratio of 0.6 start to behave non-linear at the same force level for both loading rates. It is obvious that the force increase i.e the stiffness of the element is reduced after the linear elastic region where the reduction is more distinct for specimens with higher V/N-ratios. This effect cannot be described by only taking the second order effect into account which leads to higher moments in the beam and to a continuous reduction of the stiffness during the experiment.

The effect of the stiffness reduction can be investigated by looking at the beam deformation during the test. Figure 4.16 illustrates schematically the deformation of the beam at different stages. Only the centre axis of the beam is shown. Figure 4.16(b) shows the beam deformation after the linear elastic regime. The centre axis keeps linear and the V/N-ratio changes only slightly. The experiments show a straight linear-elastic regime between these two deformation states. The middle axis has rotated to a certain angle α from its original state during the deformation. This rotation is basically prevented due to the fixed ends of the beam and this leads to a reorientation of the middle axis at a force level where the linear elastic regime ends. The beam ends are rectangular to the support structure after the reorientation and two hinges are generated in the beam as indicated in Figure 4.16(c). The V/N-ratio has rapidly changed at this instant where the moments in the beam have increased due to the second order effect which leads to a higher V/N-ratio. This is indicated in the experimental curves with the plain increase of the curve where the non-linear regime begins. Increasing the deformation leads then to a stiffening of the specimen which is indicated with a curved trend in the experiments.

The stiffening indicates a change in the V/N-ratio at which the amount decreases i.e. the normal force has a higher increase than the shear force. The stiffening can be explained by looking at Figure 4.18(a). The beam is modelled

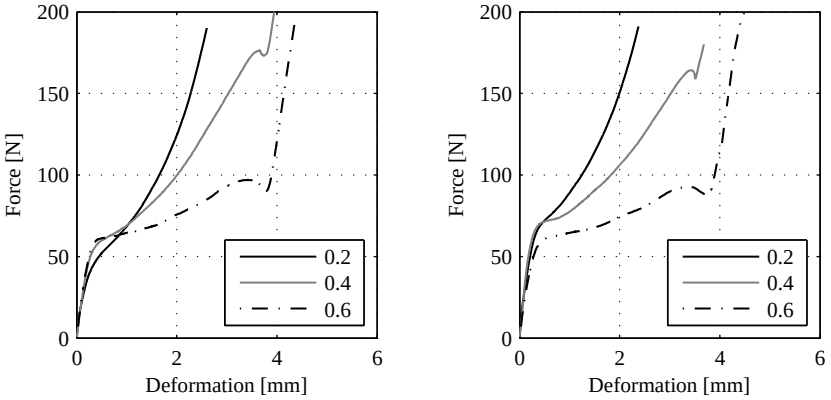

(a) Large square cross-section/ loading rate $5\mu m/s$

(b) Large square cross-section/ loading rate $15\mu m/s$

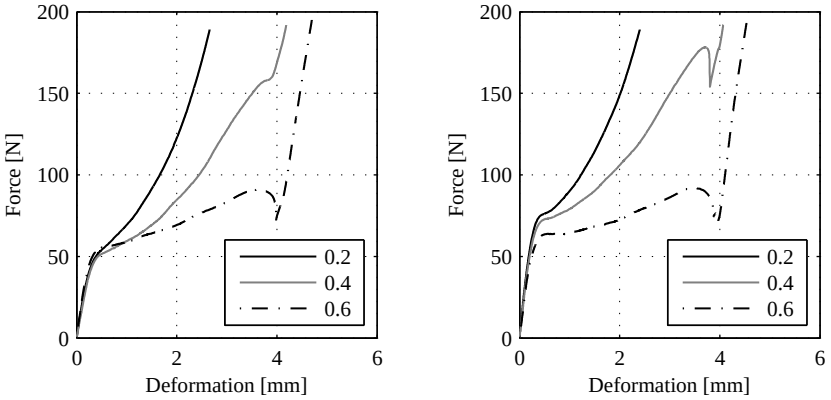

(c) Large round cross-section/ loading rate $5\mu m/s$

(d) Large round cross-section/ loading rate $15\mu m/s$

Figure 4.17.: Force-deformation curves for beams with large cross-section, different V/N-ratios and orientation of 30°/55° tested in compression

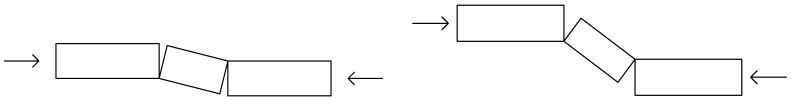

(a) (b)

Figure 4.18.: Possible mechanism developing in specimens loaded under different V/N-ratios in compression: (a) stable condition for low V/N-ratios, (b) unstable condition for high V/N-ratios

with three segments where the interceptions indicate the provision of the hinges and it is assumed that no tensile force can be carried. The three segments have only contact under compression in the edges. It is obvious that the system is stabilised in this state. Deforming the system under compression leads to a reduction of the interception, and as a consequence it is forced to a more stable state. The same happens in the experiment where the beam starts to stabilise itself when the moments compared to the normal force are reduced, which corresponds to the reduction of the interception. This will lead to stiffening in the force-deformation curve up to the point where the deformation capacity of the middle part of the beam is reached and the specimen fails, which occurs when the force drops. This effect is visible for both ratios of 0.4 and 0.6, but the decrease in force is more clearly visible for specimens with a ratio of 0.6. The force increases rapidly after this drop because the specimen parts touch the support structure which leads to purely material compression. This behaviour corresponds to the structural behaviour of the global lattice structure when the layers start to touch each other under compressive load which is described in Chapter 5.4.2.

Figure 4.19 illustrates the measured curves for beams with small cross-sections and two different loading rates for all ratios. The main observations are the same like before for the beams with large cross-sections. The effects on the beam behaviour are more visible for the small beams because they have a higher slenderness. This leads to a more distinct non-linear behaviour of the beams. Specimens with a ratio of 0.2 show a larger non-linear regime until the specimen reacts like under full compression. Specimens with a ratio of 0.4 have a significantly smaller force increase after the linear elastic part until they reach the point where the specimen fails because the deformation capacity of the middle part is reached. The force decrease is more distinct than for specimens with large cross-sections and the amount of the deformation until the specimen fails is nearly the same for ratios of 0.4 and 0.6. The force increase after the beam fails corresponds to the same behaviour like the beams with large cross-sectional areas.

The main difference in the behaviour between large and small beams is visible for specimens tested with a ratio of 0.6. They show a plastic regime where the force remains constant to a deformation at about $4mm$. This can be explained by looking at Figure 4.18(b). The system is not stable any more because the position of the contact points lies outside of the specimen dimension. This leads to a generation of plastic hinges at the location of the interceptions, whereas the moment resistance is given by the material and geometrical beam properties. The value of the moment keeps then the same value while increasing the rotation of the hinge during the deformation in the experiment. The plastic deformation at the same force level in the experimental curves indicates this behaviour.

4.5. Conclusion

The mechanical properties, namely the modulus of elasticity E_{beam}, the yield stress f_{pl} and the maximum deformation $\delta_{max,beam}$ of single beam elements under

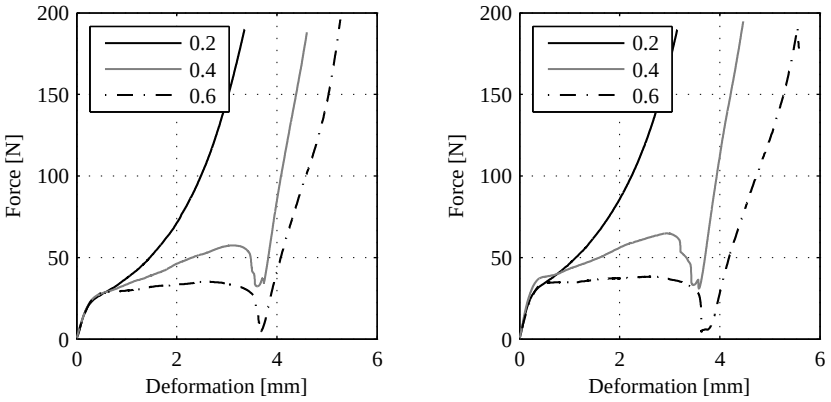

(a) Small square cross-section/ loading rate $5\mu m/s$

(b) Small square cross-section/ loading rate $15\mu m/s$

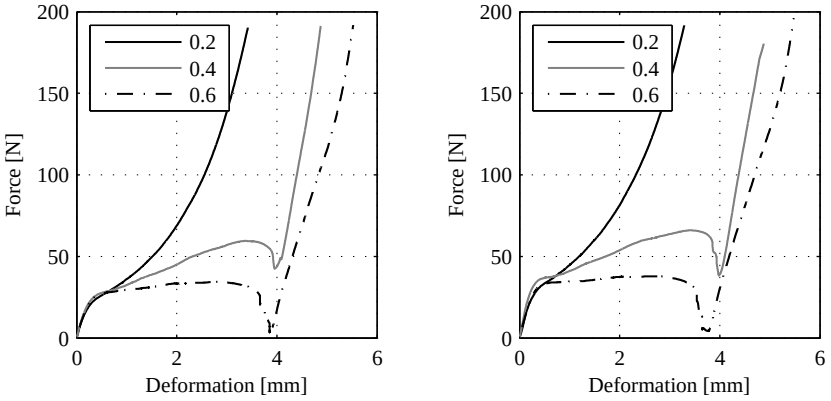

(c) Small round cross-section/ loading rate $5\mu m/s$

(d) Small round cross-section/ loading rate $15\mu m/s$

Figure 4.19.: Force-deformation curves for beams with small cross-section, different V/N-ratios and orientation of 30°/55° tested in compression

tensile load were investigated in this Chapter to determine the input parameters for the classical lattice model. The influence of the environmental conditions on the single element properties produced with the PolyJet technology were studied in order to preserve the same material behaviour in single element experiments and in the global lattice experiments. The observation that the mechanical properties decrease while increasing the environmental humidity agrees with a study by Ottemer and Colton (2002). The storing time from the production until the experiment of the specimen decreases the mechanical properties significantly, which agrees again with the investigation by Ottemer and Colton (2002). The parts used in their study were produced with the stereolithography process, whereas no equivalent studies are available for parts produced with the Jetted photopolymer technology, which has been used in this Thesis.

The build orientation has a remarkable influence on the modulus of elasticity E_{beam} and the yield stress f_{pl} whereas the maximum deformation $\delta_{max,beam}$ is not influenced. The differences in the measured yield stress f_{pl} can add up to 50%. Ottemer and Colton (2002) noticed a difference of maximum 5% in the strength by changing the build orientation. In contrast to the presented results, the parts used by Ottemer and Colton (2002) were produced with stereolithography, they were stored in different environmental conditions and the specimen size was more than 10 times larger. This can lead to the observed differences. The material used in this work has to be described as an anisotropic material.

The influence of the loading rate was investigated in order to estimate the influence of different layer deformations in the lattice structure to the global lattice behaviour. The single beam properties are highly dependent on the loading rate which is typically for thermoplastics. Increasing the loading rate leads to an increase of the modulus of elasticity as well as the yield stress and to a reduction of the maximum deformation at failure. This behaviour can be described with a simple visco-elastic material model; the Kelvin-Voigt model is sufficient to characterise the main characteristics of the material.

A size and shape effect on the yield stress f_{pl} was observed at this scale of material testing for specimens which were not produced parallel to the build orientation. The yield stress decreases by reducing the middle area of the tested specimens. Beams with a square cross-sectional area show a slightly higher yield stress than the corresponding beams with a round cross-sectional shape. With the presented study, the influence of this effect can be respected in the simulations by applying the corresponding single beam properties for the different beam geometries.

A method using video image correlation was presented to measure the modulus of elasticity E on parts with dimensions in the millimetre range. It is more appropriate to measure the strain over the whole surface of the investigated specimen part during the experiment than using the measurements from the external LVDT to calculate the modulus of elasticity. The LVDT records additional machine displacements and the deformation of the support structure during the experiments, which will lead to a significant underestimation of the modulus of elasticity. The

advantage using video image correlation is that the material behaviour is not influenced while recording the surface deformation.

It is necessary to determine the mechanical properties directly on specimens with a geometry corresponding to the elements in the global lattice structures. This means testing specimens in the millimetre range. Identifying the mechanical properties on specimens with dimensions defined in different codes for polymers would lead to different results than determined here. Using these values for the simulation would not respect the shape and size effect of the investigated single beam elements which leads to a wrong interpretation of the global lattice structure behaviour.

Single element force-deformation curves for different V/N-ratios were also determined in this Chapter in order to simulate the lattice behaviour by means of an alternative model based on this information. The loading curves of the tensile experiments show the same behaviour for the different V/N-ratios when studying beams with large middle cross-sectional areas. Beams with small middle cross-sectional areas achieve higher maximum forces during the experiments by increasing the V/N-ratio. This effect can be explained from the fact that the end moments in the beams are higher, which leads to higher strain rates in the outer fibres of the beam cross-section. This also leads to a higher single beam strength due to the visco-elastic material behaviour, which increases the maximum measured force. The influence on the global lattice behaviour in tension will be investigated in the simulations in Chapter 6.

The curves for the different V/N-ratios under compressive load show a strong non-linear behaviour and the curve trend varies significantly by changing the V/N-ratio. The main observations are that the beams behave the same at small deformations i.e. in the linear elastic regime until a point where the moments in the beam rapidly increase based on the second order effect. The curve trend i.e. the increase of the force after this point then differs depending on the V/N-ratio. Higher V/N-ratios lead to smaller increase of the force. Stiffening of the force-deformation behaviour can be observed for all specimens in this regime until they fail. The curve progression cannot be described with a single theory like the second order theory or the plastic hinge theory. The force-deformation behaviour of the single beam elements has to be described with different mechanism to investigate the curve trend. The different mechanism can take effect in different stages of the beam deformation or interact at the same time. This makes it difficult to identify the main mechanical influence on the curve trend during the different deformation stages where assumptions have to be made. Taking the force-deformation curves directly into account in the simulation process circumvents these difficulties and the single element behaviour is respected effectively.

It is obvious that much more effort is needed to establish the mechanical properties for the classical model than to preserve the force-deformation curves in the new model approach. The classical model is based on the simplification using linear elastic-purely plastic material behaviour whereas the new model can respect the visco-elastic material behaviour in a simple way and no further assumptions

are necessary. The determination of the modulus of elasticity constitutes the mayor challenge that the stress levels for the calculation have to be assigned empirically to gain an acceptable value for the simulation. These calculation steps are lapsed for the new model input data.

5. Macro-mechanical behaviour of lattice structures

5.1. Introduction

The macro-mechanical behaviour of lattice structures with four different beam shapes described in Chapter 3.4 was investigated under tensile and compressive load in order to compare the results with the two different simulations. The setup for both type of tests and the results will be discussed in this Chapter. Video image correlation was additionally used to investigate the local deformation of single beams and of the different layers in the lattice.

5.2. Test setup and boundary condition

The lattice structures were loaded under tensile and compressive load according to Figure 5.1. Figure 5.1(a) illustrates the boundary condition chosen for the tensile experiments. Freely rotating supports were used to measure the lattice behaviour under tension which features degrees of freedom in all directions. Uniaxial tensile tests can be performed with fixed or with freely rotating supports whereas no standardised method exists for this type of test. Experiments and simulations were performed in the past where larger maximum loads and fracture energies were measured using fixed supports than freely rotating supports (Vervuurt and Van Mier (2000), Van Mier et al (1996) and Van Mier (1997)). There is a higher possibility that a bending moment is induced in the specimen during the mounting process in the testing device with fixed supports. This can lead to erroneous measurements. A testing setup with freely rotating supports was therefore chosen to reach a well-defined stress distribution over the cross-section of the specimen and to minimise the influence of the boundary condition on the results.

Figure 5.2 shows the test setup with the freely rotating supports for the tensile tests. The test-setup is similar to the principle in Van Vliet and van Mier (2000), which was later also applied by Stähli (2008) and Rieger (2010). Steel plates are glued at the top and the buttom of the lattice structure shown in Figure 3.7(b) which are fixed centrically to the supports with screws. The centres of the joint heads lie in the same plane as the intersection of the lattice structure to the plastic plates which were printed directly on it. Four LVDTs are installed at the edges of the specimen which are mounted on the steel plates. The LVDTs allow to measure only the deformation of the structure without any machine or support

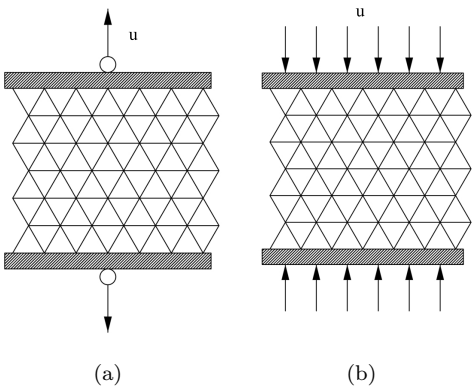

Figure 5.1.: Boundary conditions for tests in (a) tension and (b) compression

deformation during the experiments and to verify a homogeneous elongation of the structure. The freely rotating setup is mounted to the loading machine using massive steel cylinders and bolts.

The boundary condition illustrated in Figure 5.1(b) was chosen for the compressive experiments on the lattice structures. The specimen is loaded between two non-rotating rigid loading plates which ensure that every point of the top plane of the structure has the same deformation during the loading. This boundary condition can be modelled in a simple way which would reduce the complexity of the model. One rotational loading plate would be needed in compressive experiments where the specimens' top and bottom plane are not parallel to each other. Using two rigid plates in this case would produce zones in the specimen which are higher loaded than others and this leads to a erroneous measurement of the modulus of elasticity, the compressive strength and the post-peak behaviour of the material. Using rapid Prototyping, it can be guaranteed that the top and the bottom plates are parallel, which makes a rotational plate at one side obsolete. The production technique produces accurate specimens where the variance of specimen height measured on every edge of the specimen lies in the range of less than $0.1mm$.

Figure 5.3 shows the test setup for the compressive experiments in the loading frame. Four LVDTs are placed at the edges of the specimen to measure the deformation of the lattice. They are fixed at the lower cross beam of the testing frame. The tips of the LVDTs are placed on a rigid steel plate which lies between the specimen and the upper loading plate. The most important factor is to ensure that the lower and the upper cross beam of the testing frame are parallel to each other to prevent an irregular deformation of the specimen.

The setup for the macro-mechanical experiments is illustrated in Figure 5.4. An electro-mechanical testing machine from *Zwick&Roell* with a loading capacity of $200kN$ was used to perform the experiments. The tests were controlled

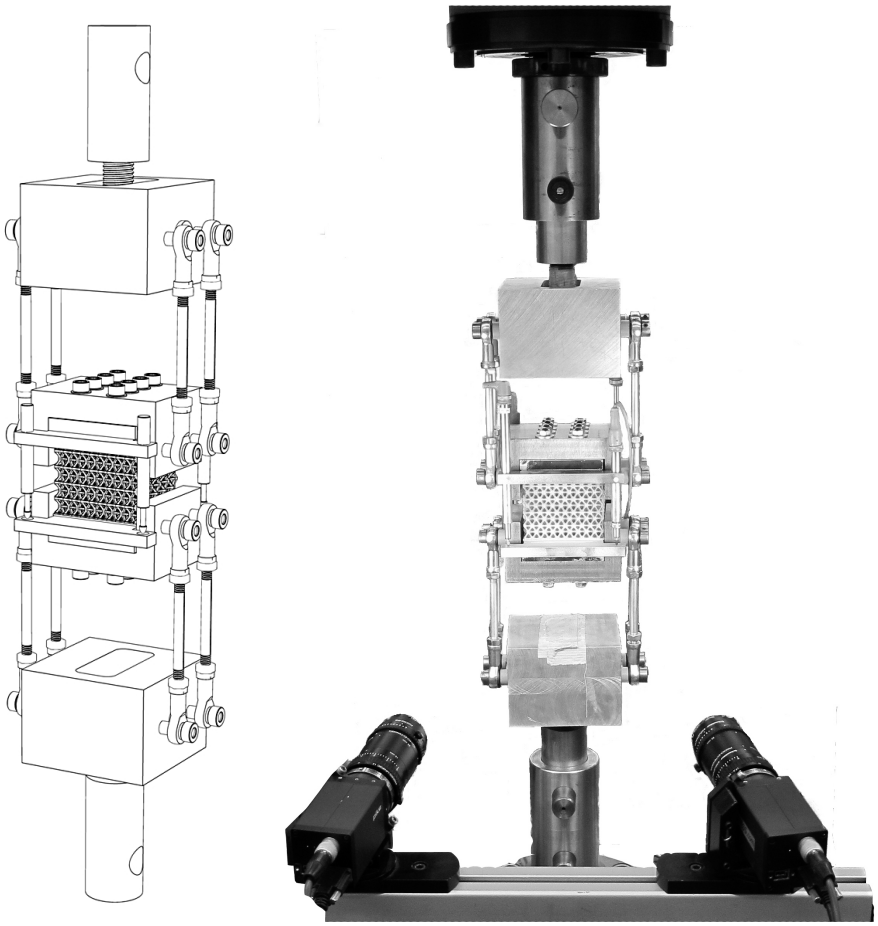

(a) (b)

Figure 5.2.: Tension test device

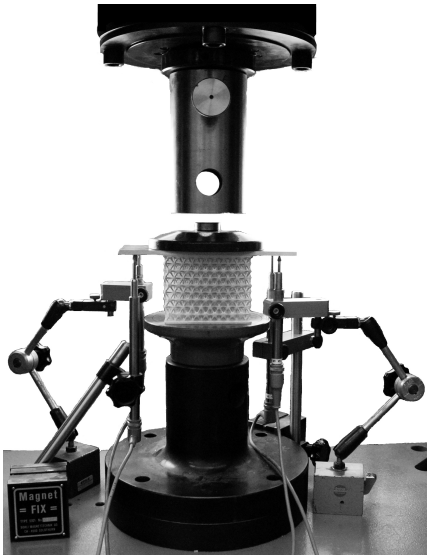

Figure 5.3.: Compression test device

over the cross-beam of the testing machine where the displacement velocity was $45\mu m/s$. The force and the cross beam displacement signal is controlled from the *Zwick* controller whereas the software $TestExpert\ V2.0$ was used to set the displacement velocity. The signals from the LVDTs are processed with a signal amplifier $MGCPlus$ from HBM. The force signal from the testing machine was again used to synchronise the measured displacements from the LVDT and the collected pictures from the video image correlation system like for the single beam element test setup (see Figure 4.2).

5.3. Testing series and specimen preparation

Four specimens for every single beam geometry (see Section 3.3) were produced where two global lattices were tested under tension and two under compression.

The same steps from the production until the experiments were followed for the lattice structures like for the single beam elements to provide the same properties for both types of test. Six single elements were additionally printed with the structures and tested to verify no change in the single properties. The support material was washed out using water jet directly after the production of the global lattice structures. The specimen were then cleaned in a 4.0% $NaOH$ solution for three hours to dissolve the remaining support material. They were stored for 14 days in a controlled environment of 20° and a RH of 85% until the experiments. The steel plates used for the tensile test support were glued on the specimens three days before testing and also the surface painting was done one day before

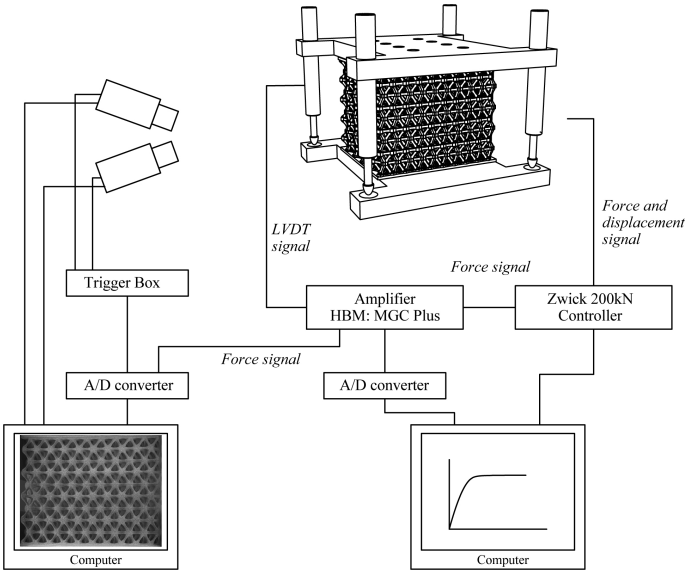

Figure 5.4.: Overview of the macro-mechanical test setup

testing in the controlled environment.

5.4. Results

The results from the global lattice experiments will be discussed in this section. The data from the video image correlation measurement are used to describe the non-uniform deformation behaviour of the structure and to verify model assumptions which were introduced in Chapter 4.2 i.e.the nodal areas can indeed be assumed to act as rigid bodies. All measured curves show a contact effect at the beginning of the measured curve due to the alignment of the specimen in the testing machine for the tensile experiments. The contact effect in compression occurs from the difference of the height of the specimen in the edges of maximum $0.1mm$. The zero point of the curves was therefore corrected according to ASTM D638 (2008) for a correct calculation of the stiffness $K_{lattice}$.

5.4.1. Tension

Figure 5.5 shows the results of the tensile experiments of global lattice structures with the four different beam geometries. The deformation of the lattice was measured by calculating the average of the four LVDTs measurements. The values had a maximum difference of $0.2mm$ among each other at the point where the specimen failed in the experiments, except of two tests where a maximum difference of $2.0mm$ i.e. $1.6mm$ was measured. Figure C.3 in the Appendix show the curves

for a good and for a worse measurement. Using the deformation measurement from the cross beam of the testing machine would lead to a softer ascending part of the curves due to the additionally measured deformation of the rotational-free test setup at this part of the curve.

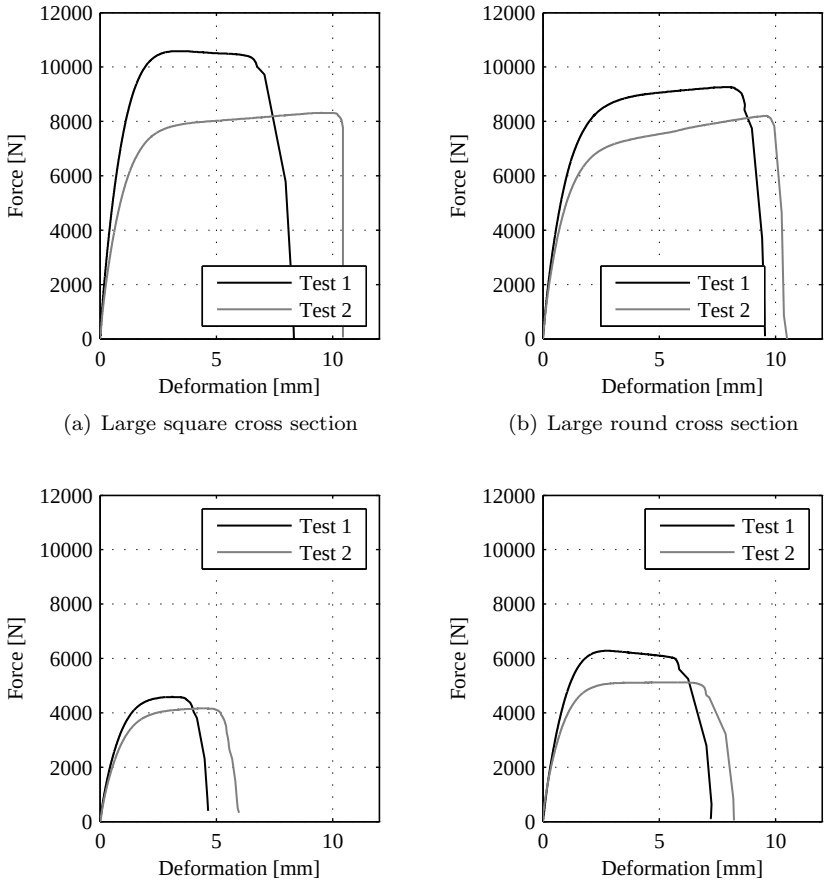

(a) Large square cross section

(b) Large round cross section

(c) Small square cross section

(d) Small round cross section

Figure 5.5.: Load diagrams for lattice structures in tension

Figure 5.5(a) illustrates typical force-deformation behaviour of the lattice structure which contains large square cross-sectional beams. It is obvious to see that the specimens behave nearly linear elastic up to a force level of about 75% where the stiffness starts to decrease rapidly. After this force level, the stiffness decreases gradually to a point where the structure behaves in a plastic way i.e where the force stays constant or increases slightly by increasing the deformation. The spec-

imen then fails in a brittle manner where the force drops rapidly to zero. The whole curve of one experiment describes a typical visco-elastic material behaviour which was already mentioned for the single element deformation behaviour (see Chapter 4.3). It is clearly visible for all experiments that the higher the maximum force of a structure is, the lower the deformation is until the specimen fails. This global lattice behaviour corresponds to the observations for the single beam elements.

The scatter of the measured force in the plastic region can reach up to 30% for the specimen with large square cross-sectional beams in only two experiments which is quiet high. The high scatter can be explained by looking at Figure 5.6. It illustrates the measured strain of beams in the lattice during one experiment which are lying in different layers. The analysed beams are indicated in Figure 5.6(a) where the strain of in-plane and out-of-plane beams was calculated using video image correlation. It is obvious that the strain of the different out-of-plane beams (black lines in Figure 5.6(b)) vary strongly over the height of the structure where the difference at the maximum lattice deformation is more than 60% between the lowest and the highest measured strain. No tendency is present where the lowest and the highest values over the height of the specimen occurs. This indicates that the lattice deformation is not constant over the whole height and the single layers can have different deformation rates. When respecting the results of the single element behaviour, where it was shown that the modulus of elasticity and the yield stress reach higher values while increasing the deformation rate, leads to the assumption that the layer with the lowest deformation rate in the lattice dictates the global lattice behaviour. A lattice with a homogeneous deformation i.e. all layers have the same deformation rate, leads to higher measured loads and a stiffer behaviour in the ascending part of the lattice than with a non-uniform deformation. In structures with a non-uniform layer deformation, the force capacity of a layer with a high deformation rate cannot be reached because the layer with a lower deformation rate already started to behave plastic and the whole deformation of the lattice is then concentrated in this layer. Based on this assumption, the high scatter of the macro-mechanical lattice results can be interpreted. Simulations with different single beam properties in different layers will be presented in Chapter 6.3.1 to verify the assumption.

The mean value of the measured maximum forces reaches a higher value for structures with large square beams (about $9'000N$) than for structures with large round beams (about $8'000N$). This observation corresponds with the results from single beam experiments where large square beams show higher yield stresses than large round beams (Figure 4.8). Also a slightly higher deformation behaviour of structures with large round beams can be observed, which also agrees with the single beam results (Figure 4.9).

Lattices with small square beams show a mean value of the maximum force of about $4'000N$ whereas structures with small round beams reach a mean force of about $5'500N$. The high difference of the maximum forces does not agree with the results from the single element tests where small round beams have slightly

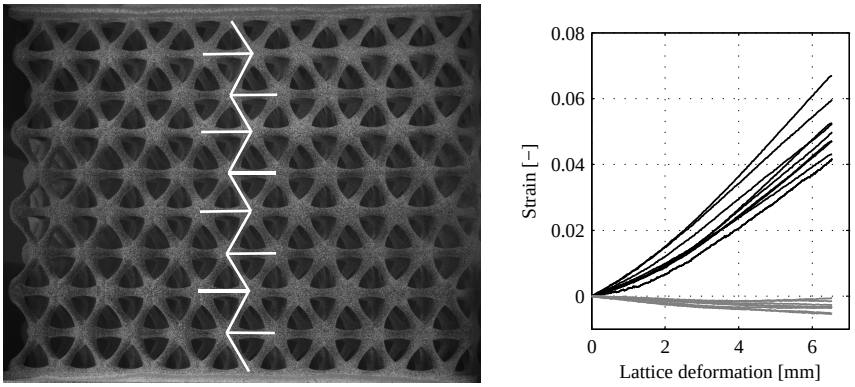

(a) (b)

Figure 5.6.: Analysed strain distribution of beams in the lattice structure: (a) Analysed beams, (b) Strain distribution (out-of-plane beams: black lines, in-plane beams: grey lines)

Table 5.1.: Stiffness $K_{lattice}$ $[N/mm]$ and maximum force $F_{max,lattice}$ $[N]$ for lattice structures in tension

Cross section shape	$K_{lattice}$ Test 1	$K_{lattice}$ Test 2	$F_{max,lattice}$ Test 1	$F_{max,lattice}$ Test 2
Large square	8'869	6'077	10'585	8'319
Large round	6'503	5'292	9'264	8'204
Small square	4'295	3'588	4'585	4'164
Small round	5'528	4'844	6'278	5'122

smaller yield stresses than small square beams. On the other hand, this difference can be explained by looking at the force-deformation diagrams measured under different V/N-ratios (Figure 4.15). Specimens with higher V/N-ratios show a higher force than those with small V/N-ratios for small round beams. This could explain the contrary observation of single element tests under pure tension for the classical model and the global lattice experiments. This observation will be discussed further when analysing the simulation results from both models in Chapter 6.4.

Structures with small round beams show a significantly higher deformation capacity than structures with small square beams. Structures with small square beams fail at the lowest deformation in comparison to all other specimen geometries.

The measured stiffness and maximum forces are listened in Table 5.1. The stiffness was again calculated between the force levels of 0% and 60% which corresponds to the chosen levels of the calculation for the single beams (Chapter 4.3).

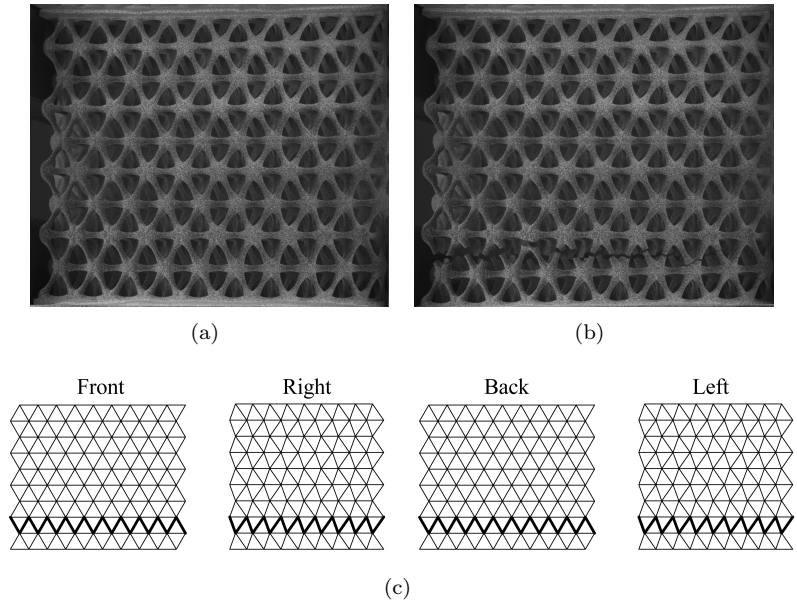

Figure 5.7.: Crack pattern of lattice structure in tension: (a) Lattice before fracture, (b) partly notched lattice, (c) schematical drawing of final crack pattern

Lattice structures with large square beams show higher values than those with large round beams. This observation corresponds with the results from the single beam experiments where a smaller stiffness was measured for round beams. Lattices with small square beams have significant smaller values which agrees with the measurements from the single element test that the stiffness is higher for large beams. The values for lattices with small round beams have a significant higher value than those with small square beams but are smaller than the values from lattices with large beams. This observation does not agree with the measurements from the single beam tests where the value lies in the same order like for small square beams. No explanation for this observation can be given at this point. A detailed investigation will be made with the numerical simulations in Chapter 6.3.

Figure 5.7 shows a typical failure pattern for a lattice structure failed under tensile load. Picture 5.7(a) was captured directly before the lattice starts to break and picture 5.7(b) was captured 0.4 seconds thereafter. It is visible that the whole specimen is intact and no single beam failed before collapse i.e. no indication is given from the lattice surface that the structure will begin to break. The specimen fails in a brittle manner: between two captured pictures nearly one complete layer is broken i.e. in a short time period. It is also visible from picture 5.7(b) that

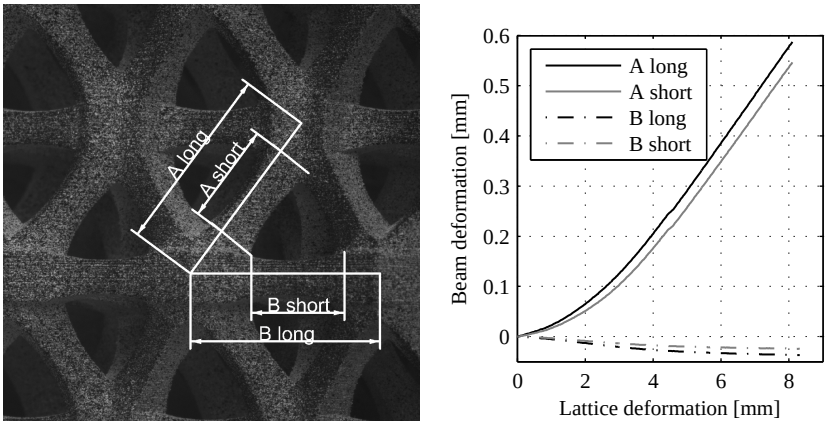

(a) (b)

Figure 5.8.: Beam deformation for different length in a lattice structure with large square cross-sectional beams: (a)Definition of the length, (b) Deformation curves

not every beam broke in the middle part between two node regions. There are several beams which failed in the node region. No tendency of the crack position in the beam could be found for all experiments. There seems to be randomness in the position since the crack started to propagate at the edge of the specimen.

A constant orientation and position of the whole crack in the lattice can be found for all lattices. Figure 5.7(c) illustrates the position and the orientation of the crack after the specimen has fully failed. The crack pattern for the other specimens can be found in Appendix C.3. All specimen break in the first or the second layer from the top or the bottom support plates and the crack propagates through only one layer in more than 50% of the experiments. This observation indicates that the lattice geometry induces the position of the highest loaded beams in structure. The cracks which propagate through one layer also indicate a homogeneous loading condition where no moment occurs during the experiment in the specimen. The specimen where the crack propagates through two layers indicate a slightly eccentric loading condition of the lattice. However, the crack started at one edge and propagated through the whole specimen without any crack arrest. Using fixed supports would lead to bending moments in the specimen after the first crack starts to propagate. The moment leads to a crack arrest and another crack can start to grow at the opposite side of the specimen (Van Mier (1997)). The crack position will be further investigated in the simulations in Chapter 6.3.

In order to verify the model assumption from Chapter 3.4 that the node area can be modelled as a rigid body and only the beam section between the node areas would deform, the deformation of beams with a length between the centres of two nodes and beams with a length between two node areas were analysed.

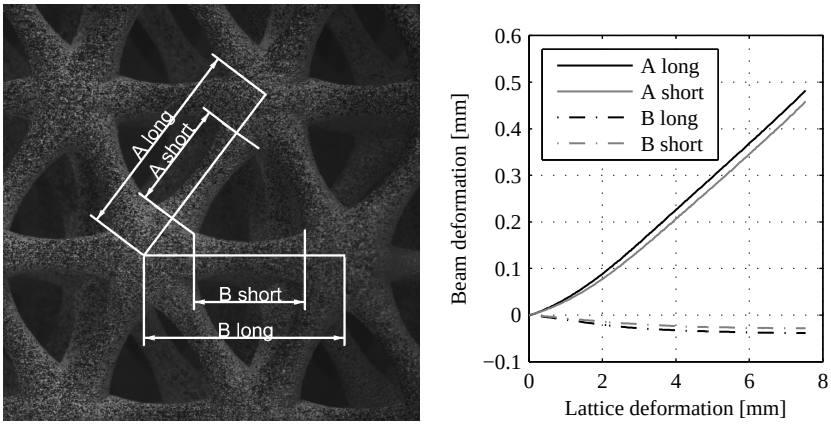

(a) (b)

Figure 5.9.: Beam deformation for different length in a lattice structure with small round cross-sectional beams: (a)Definition of the length, (b) Deformation curves

Figure 5.8 shows single beam deformations during a tensile experiment. The example relates to the lattice with large square cross-sectional beams. This beam geometry represents the worst case for the model assumption due to the smallest inter-sectional beam length of $4.91mm$ compared with the other beam geometries. The node area deformation would have the largest influence for this case due to its dimension. It is obvious to see from Figure 5.8(b) that the inter-sectional beam (A short) reaches nearly the same deformation as the beam between two node centres (A long). The long beam reaches a slightly higher deformation at the highest lattice deformation whereas the difference between both curves is only 7% at the maximum lattice deformation. Therefore, the model assumption seems to be applicable due to the small measured difference, where uncertainties of the stress distribution in the nodes and the amount of the node stiffness to the beam stiffness can be neglected, which reduces the complexity of the model and the uncertainties of the parameter assignment.

Figure 5.9 shows the same analysis for the lattice with small round cross-sectional beams. This case represents the best case where the node area has the smallest dimension compared to the inter-sectional beam length of $5.66mm$. The inter-sectional beam deformation reaches nearly the same value as the beam between two node centres in this case which is illustrated in Figure 5.9(b). The difference between the two curves is only 5% at the maximum lattice deformation. The deformation difference is reduced to 2% as expected between the two cases i.e. between the beam deformation in lattices with large square and small round cross-sectional areas. The measured difference between the long and the short beam will therefore not exceed 7% for all tested lattice geometries. Increasing the

inter-sectional beam length i.e the slenderness would lead to even smaller deformation difference. This makes the model assumption also applicable for foams where the slenderness of the beams or cell walls is higher than for lattices used in this thesis. Producing lattices with higher or lower beam slenderness with the PolyJet technology and keeping the distance between the node centres $10.0mm$ is not applicable due to cleaning process of the structures which was mentioned in Chapter 3.3. The deformation difference of the beam between two node centres and the inter-sectional beam would increase with lower beam slenderness where the influence of the nodal area on the structural deformation behaviour could be investigated more detailed.

The difference for the in-plane beams can reach more than 50%. Different points have to be mentioned for the interpretation of this result. The measured deformations for the in-plane beams are in the range of less than $50\mu m$. Measuring values in this range with VIC can lead to differences between the real deformation and the measured deformation because the scatter of the measurement lies in the μm-range and a certain linearity error can be present. This relativises the validity of the presented measurement. The amount of the in-plane beam deformation does not influence the vertical lattice deformation in the linear elastic regime, whereas the non-linear regime is affected by the in-plane stiffness (see Chapter 6.3.1 for the classical model and Chapter 6.4.1 for the new model). The in-plane beams are also much less loaded than the out-of-plane beams and have smaller V/N-ratios i.e. they are mostly loaded with a normal force.

5.4.2. Compression

Figure 5.10 illustrates the results for the experiments in compression of the lattice structures with the four different beam geometries. The deformation of the lattices was calculated from the measurements of the LVDTs in the same way as in the tensile tests. The difference between the measured deformations of the LVDTs among each other was less than $0.2mm$ and no difference of the deformation measurement from the LVDT and the testing machine was present. The specimen were therefore compressed centrically with no or just little bending moment occurring during the experiment. The experiments show a small scatter in the measurement The two experiments for the lattices with the small beams show nearly exactly the same deformational behaviour.

Figure 5.10(a) shows the deformation curve for the specimen with large square cross-sectional beams. It can be clearly seen that the specimens behave nearly linear elastic at the beginning of the deformation up to a force level of about 50% where a decrease in stiffness starts. The stiffness keeps nearly the same value in this regime up to a deformation of about $22mm$ where the maximum force is reached. A clear force drop is visible before the force starts to increase rapidly after the minimum of the force drop is reached, which implies that the structure is fully compressed and the different layers are touching each other (see Figure 5.11(b)). The maximum force before the force drop is about $8'500N$ for lattices with large square beams. The lattice structures with large round cross-sectional

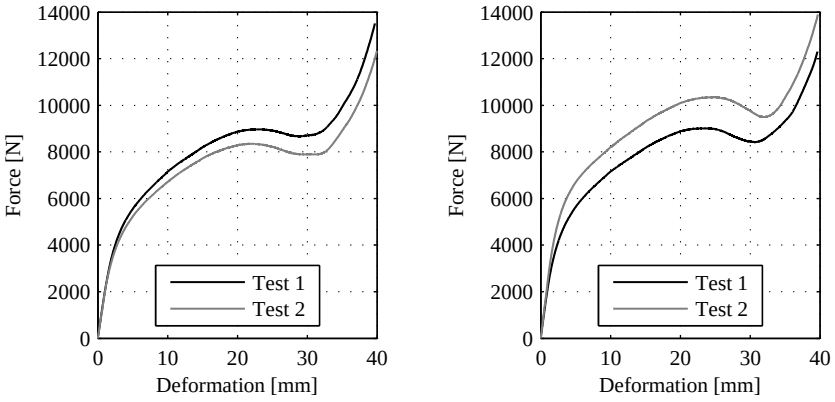

(a) Large square cross section

(b) Large round cross section

(c) Small square cross section

(d) Small round cross section

Figure 5.10.: Load diagrams for lattices in compression

beams show the same curve trend (Figure 5.10(b)). The force level, where the stiffness decrease starts, the maximum force peak at about $24mm$ and the force drop are in the same region for both square and round large cross-sectional beam geometries. The mean difference is that the large round lattice structures reach significant higher forces. The maximum forces before the force drop reach a value of about $9'700N$ which is 14% higher than for specimens with square cross sections.

Figures 5.10(c) and 5.10(d) illustrate the deformation behaviour for lattices with small cross-sectional beams. The linear-elastic regime is followed by a stiffness decrease. The stiffness change occurs at a force level of about 80%. The stiffness after the linear-elastic regime is much smaller than for the lattices with large beams. The deformation where the force reaches the maximum and starts to drop lies in the region of $15mm$ and the force drop is more distinct for the small beam lattices. A nearly ascending plastic plateau is visible after the force minimum is reached. Increasing the deformation after the plastic plateau leads to a rapid increase in force. This is also the point where the layers of the lattice start to touch each other and the structure is fully compressed. The point where the force increase starts is located at a deformation of about $37mm$ in contrast to the lattices with large beams where the force starts to increase at a deformation of about $32mm$. This observation occurs from the difference of the inter-sectional beam length where small beams have a larger length which leads to a higher deformation capacity before the layers begin to touch each other.

Open- or close-cell plastic or metallic foams show the same deformation behaviour under compressive loading (Gibson and Ashby (1997), Jang and Kyriakides (2009a)). The main difference between the presented curves in this thesis and the curves of foams is that the decrease in stiffness after the linear-elastic regime is not present for open- or close-cell foams. The force decreases slightly after the linear-elastic regime and the plastic plateau starts directly afterwards. This difference appears because the beams and the cell walls in the investigated foams have a much higher slenderness than the beams investigated in this work. This could lead to the formation of plastic hinges in the elements and the force will keep constant while increasing the deformation. No stiffening of the elements occurs which would lead to a decrease in the global stiffness of the structure before it deforms purely plastic.

The values of the stiffness are listed in Table 5.2 for every beam geometry. The values lie in the same region for every beam geometry expected for the lattices with small round cross-sectional beams which are 25% higher. The stiffness of the structures under compressive load are significant smaller than under tensile load (less than 25%). The high difference could be occurred from geometrical imperfections of the beams in the global lattice whereas the imperfections could not be detected. This would lead to a small global lattice stiffness under compressive load together with the second order effect. A difference 75% between the modulus of elasticity in tension and compression seems unrealistic.

Figure 5.11 shows the lattice deformation for two different deformation levels

Table 5.2.: Stiffness $K_{lattice}$ $[N/mm]$ and maximum force $F_{max,lattice}$ $[N]$ for lattice structures in tension

Cross section shape	$K_{lattice}$ Test 1	$K_{lattice}$ Test 2	$F_{max,lattice}$ Test 1	$F_{max,lattice}$ Test 2
Large square	1'248	1'183	8'970	8'350
Large Round	1'292	1'673	9'013	10'352
Small square	1'324	1'281	5'078	5'029
Small round	1'673	1'581	5'542	5'588

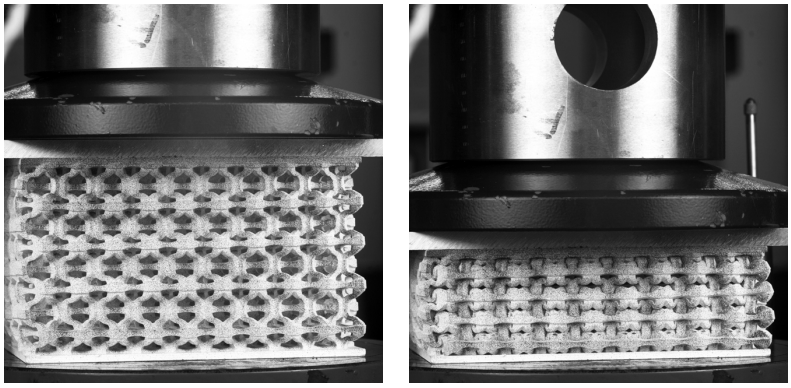

(a) (b)

Figure 5.11.: Deformed global lattice in compression: (a) at 50% strain, (b) at 100% strain

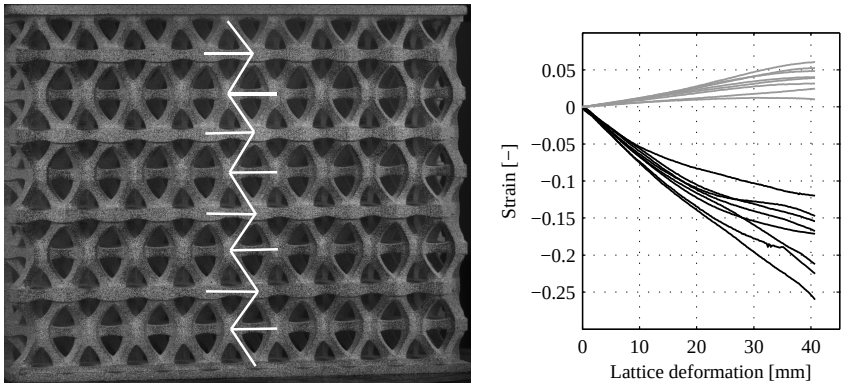

(a) (b)

Figure 5.12.: Analysed strain distribution of beams in the lattice structure: (a) Analysed beams, (b) strain distribution (out-of-plane beams black lines, in-plane beams grey lines)

for a lattice structure with small square cross-sectional beams. It can be seen from Figure 5.11(a) that at a strain level of 50%, not every layer has deformed at the same amount. Figure 5.11(b) shows the structure at 100% strain where the specimen is fully compressed. The hollow space between the beams has vanished and the layers touch.

The measured strains in the beam elements in different layers of the lattice structure during an experiment in compression are illustrated in Figure 5.12. VIC was used to calculate the strains. It is obvious that the strain of the out-of-plane beams also varies strongly over the height of the structure and the lattice deformation is considered as non-uniformly. Also no tendency is present where the lowest and the highest values over the height of the specimen occurs. The difference in the strain at the maximum lattice structure deformation occurs from the fact that the layers have different in-plane deformations which lead to a difference in the maximum measured strain of the beams although the maximum vertical compression is given from the layer distance. The difference in strain of the beams among each other is more than 100%. The lattice therefore behaves in the same manner under tensile and compressive load where the beams have different loading rates during the test. However, the scatter in the deformation behaviour is much smaller for tests in compression. This can be explained from the fact that it is more convenient to adjust the testing setup for a centric compressive experiment than for a centric tensile experiment. The deformation measurement of the LVDTs indicates the accuracy of the experiments at which the maximum difference of the LVDTs among each other is $2.0mm$ during the tensile test and $0.2mm$ during the compressive test. The difference of $2.0mm$ can lead to this higher scatter in the measurements because the lattice has not the

same deformation rate in every edge.

5.5. Discussion and conclusion

The deformation behaviour of lattice structures with four different beam geometries was investigated under tensile and compressive load in this Chapter. The lattice structures show the same visco-elastic material behaviour for all beam geometries under tensile load with a higher deformation capacity for lattices with round beams than those with square beams. Structures with large square beams reach higher maximum forces than those with large round beams. This observation corresponds in a first qualitative analysis to the single beam element behaviour where square beams reach higher yield stresses. The contrary is present for the lattices with small cross-sectional beams where lattices with square beams reach significantly smaller maximum forces than with round beams although the measured yield stress in the single element experiments is also higher for square beams. This qualitative observation cannot be explained only by taking the single beam properties like the yield stress into account. However, the force-deformation behaviour of small round beams with different V/N-ratios shown in Chapter 4.4 indicates an increase of the maximum force by increasing the V/N-ratio. This could explain the difference in the measured maximum force of the lattice structures. A quantitative analysis will be performed with numerical simulations in Chapter 6.3 to prove the hypothesis.

All lattice structures show the same deformation behaviour under compressive load. A decrease in stiffness is observed after the linear-elastic regime. The decrease in stiffness is more distinct for lattices with small beams. The force then starts to drop after the maximum force is reached, until it begins to increase rapidly at a certain deformation for lattices with large beams due to contact between the layers. Lattices with round beams reach a slightly higher maximum force than lattices with square beams. A "longer valley" is only visible for lattices with small beams after the force drop. The structure deforms in a plastic manner while keeping the force nearly constant with an increase of the deformation until the layer starts also touching each other at a certain deformation which leads to a rapid force increase. The behaviour of lattices with small beams corresponds more to the compressive behaviour of open- or close-cell plastic or metallic foams. Foams offer a long plastic plateau before the force rapidly increases but a decrease in stiffness after the nearly linear-elastic regime is not present.

The strain distribution of beams in different layers of the structure was studied using VIC. These results show that the lattice deformation over the whole height is not constant i.e. the deformation rate of the layers differs from each other. This can result in a high scatter of the measured behaviour because the layer with the lowest deformation rate dictates the maximum reachable force of the structures due to the visco-elastic behaviour of the beams for lattices loaded under tension. This leads to the qualitative conclusion that the higher the differences in the deformation rate among the layers, the lower the maximum force would be. A

homogeneous deformation of the specimen would increase the maximum force capacity while keeping the global deformation of the structure constant.

The tests in tension show a higher scatter than the tests in compression. The influence of the non-uniform layer deformation would explain a higher scatter in the tensile experiments. Another reason for the scatter in the results could be found in the test setup. The adjustment for compressive tests is more convenient to load the specimen centrically. The experiments in compression show a high accurateness based on the centric loading where the LVDTs measure the same deformation with a maximum difference of $0.2mm$ among each other in every edge of the specimen for the worst experiment. A more accurate justification is needed for tensile experiments. The inaccurate assembly of the specimen at the test setup will lead to an eccentric loading of the specimen and to a high scatter in the results. This could be achieved by using a set of additional bars to fixate the pendulum bars in the hinges to obtain a rigid system to fix the specimens centrically between the platens. However, the non-uniform global lattice deformation over the height leads also to a high scatter in the tensile experiments which will be investigated in Chapter 6.3.

The deformation difference of beams with a length between the centres of two nodes and an inter-sectional length between two node areas was analysed in order to check the model assumption of a rigid node area. The analysis on out-of-plane beams shows only a small difference of 7% between the beams with a large square cross-section. This beam geometry represents the worst case due to the highest content of the node area to the beam length from centre to centre. The difference is reduced to 5% when analysing beams with small round cross-sectional areas where the node area has the smallest content to the total beam length between two nodal centres. It can be concluded that the model assumption seems to be appropriate for the characterisation of the global lattice deformation behaviour in the numerical simulations. The model assumption is also convenient to design the specimen geometry of the single element experiments with different V/N-ratios due to the small difference in the deformation measurements.

6. Numerical investigation of lattice structure behaviour

6.1. Introduction

The results from the two different models and the global lattice experiments under tensile and compressive load will be compared in this Chapter. The comparison of the lattice deformation behaviour between the different models and the experiments enables to make statements about the practicability of the models. The influences of different single element parameters on the global behaviour of the structure like the maximum deformation of one element $\delta_{max,beam}$ and the plastic modulus of elasticity E_2 (see Chapter 2.1.3) are investigated in order to evaluate the sensitivity of the models. The single beam properties for the two different loading rates are taken into account for centric and eccentric simulations to describe the scatter of the tensile experiments.

6.2. Procedure for tensile simulations

The boundary and loading conditions for both models are set equal (Figure 6.1): the nodes of the lowest layer have zero displacement ($u_{x,y,z} = 0$) and an infinitely large rotational stiffness ($\varphi_{x,y,z} = 0$) in all directions. The nodes in the topmost layer cannot displace in the $x-$ and $y-$direction ($u_{x,y} = 0$) and have an infinitely large rotational stiffness ($\varphi_{x,y,z} = 0$) in all directions. A displacement in the $z-$direction ($u_z = \delta$) is applied at the nodes in the topmost layer: a uniform distribution is applied for centric simulations and a non-uniform distribution for

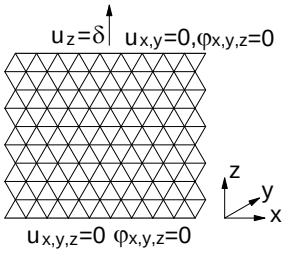

Figure 6.1.: Boundary conditions for the lattice simulations

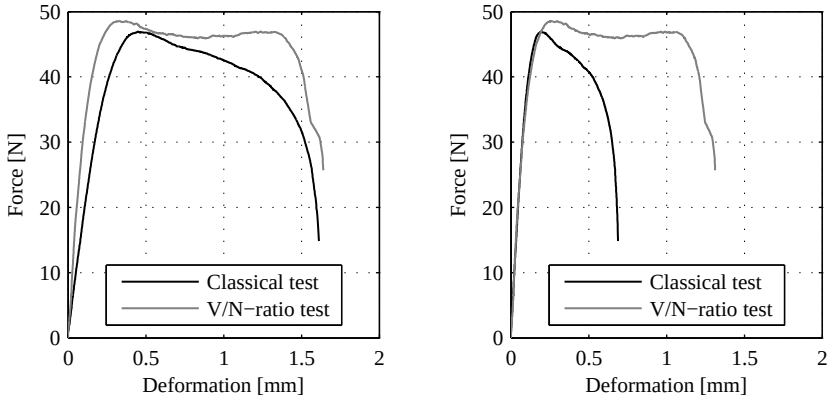

Figure 6.2.: Correction of the force-deformation curves for the new model for a beam with large square cross-sectional area and an orientation of 30°/55°: (a) measured curves, (b) curves corresponds to the measured modulus of elasticity

eccentric simulations.

The geometrical parameters of the single beams (moment of inertia I_{eq}, cross-sectional area A_{eq} and length L) are equal in both models and correspond to the values listed in Table 3.2. The single element properties for the classical model (modulus of elasticity E_{beam}, yield stress f_{pl} and maximum deformation $\delta_{max,beam}$) correspond to the results in Chapter 4.3 and the input values are listed in Appendix D.1 for both loading rates.

The force-deformation curves of the single beam elements under different V/N-ratios which are used for the new model correspond to the curves shown in Chapter 4.4 whereby the deformation from the origin point to the maximum force had to be scaled with a factor to respect the deformation of the support structures in the experiment. The example for the calculation of the factor is given for a beam element with large square cross-sectional area and an orientation of 30°/55°. Figure 6.2(a) illustrates the measured curves of the classical tensile experiment and the force-deformation curve with a V/N-ratio of 0.2 for the new model approach. The support deformations are included in these curves. It is visible that the curve from the classical tensile experiment has larger deformations in the ascending part than the curve for the new model approach. The curve from the classical experiment has to be scaled that the ascending part is identical with the calculated modulus of elasticity (Chapter 4.3) as follows:

$$Deformation_{new} = \frac{Deformation}{L_0} \cdot L \tag{6.1}$$

where L_0 corresponds to the initial length listed in Table 4.1 and L corresponds to the effective beam length between the nodal areas listed in Table 3.2. Figure 6.2(b) shows the curve after the scaling. The force-deformation curve for the new approach has also to be scaled to reach the same stiffness in the ascending part like the curve from the classical model. The scaling factors are determined empirically for the best agreement between both curves. It has to be mentioned that the deformation after the maximum force keeps the same which is not the case in Figure 6.2 where the procedure is only shown schematically.

Only the force-deformation curves with an orientation of 30°/55° are used in the simulations because this orientation is two times more present in one layer and the curves with an orientation of 90°/55° are nearly equal. Only the force-deformation curve with a V/N-ratio of 0.0 was used for the simulations with an loading rate of $5\mu m/s$ because no difference between the curves with a V/N-ratio of 0.0 and 0.2 are present with a loading rate of $15\mu m/s$ (see Figure 4.15). Additionally, the majority of the beams have a V/N-ratio of 0.2 (Figure 3.11) which makes it redundant to have the the force-deformation curves for V/N-ratios of 0.2-0.6.

The behaviour of the in-plane oriented beams in the lattice structure (orientation 0°/0° and 60°/0°), which are loaded in compression, was chosen as linear-elastic. The compressive modulus of elasticity was assumed to be equal to the tensile modulus of elasticity. A linear-elastic behaviour was selected because the measured strain in the in-plane beams are small (Figure 5.6) where it is assumed that the beams do not start to yield in compression over the whole lattice deformation. No stability problems of the in-plane beams were apparent in the lattice experiments in tension described in Chapter 5.4.1 which makes the assumption acceptable.

The simulation processes for both models are described in Chapters 2.1.3. The single beam elements in the classical model were divided into 0.2mm segments (see Figure 3.9(b)) with varying cross-sectional areas and equal lengths from which the segment with the highest stress was determined. The whole beam starts to yield when the highest loaded segment reaches the yield stress. The simulations are stopped at the point where the global force drops below $50N$.

6.3. Comparison between experiments and classical model in tension

Figure 6.3 and 6.4 show the comparison between the classical model results and the measured lattice deformation behaviour under tensile load. The simulations were performed with the measured single beam parameters for the loading rates of $5\mu m$ and $15\mu m$. It is obvious that the results from the simulations describe a nearly linear-elastic, purely-plastic structural behaviour. The force increase between yielding of the first beams and the maximum force of the lattice ($F_{max,lattice}$) is about 25% for every lattice geometry. The transition from the linear elastic to the purely plastic regime of the lattice takes place in a small deformation

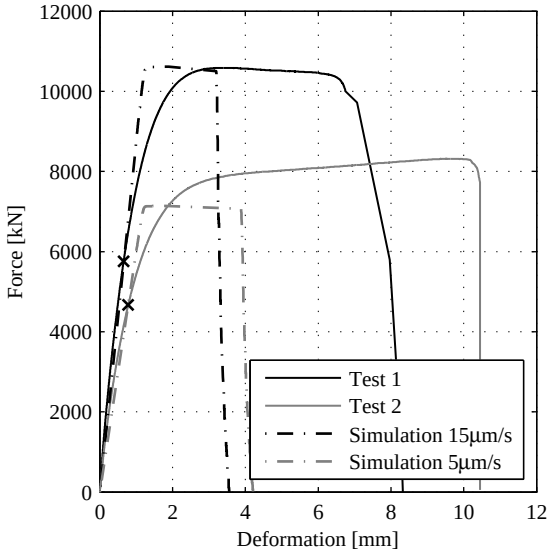

(a) Large square cross-section

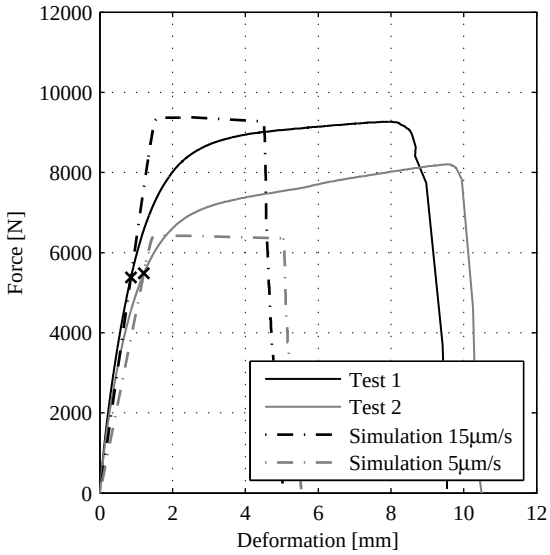

(b) Large round cross-section

Figure 6.3.: Comparison between tests and classical model results for lattices with large beams in tension; small crosses indicate the inter-section points between the experimental and the simulated curves

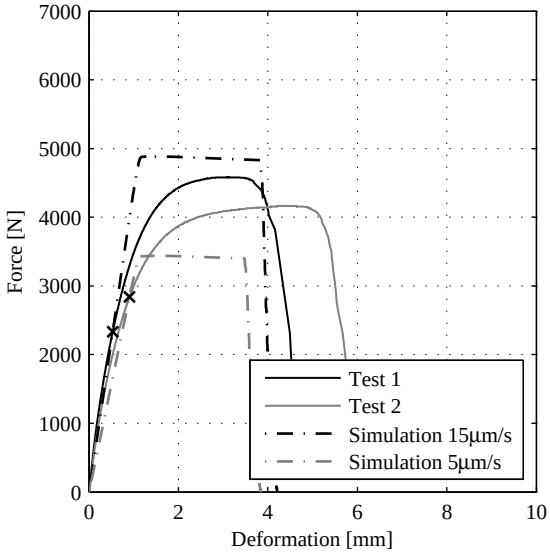

(a) Small square cross-section

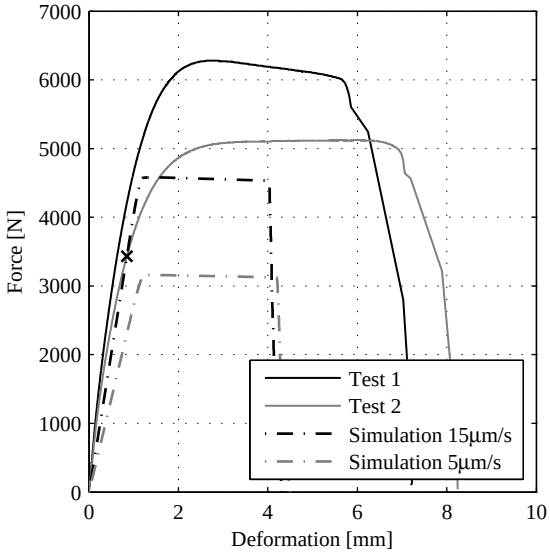

(b) Small round cross-section

Figure 6.4.: Comparison between tests and classical model results for lattices with small beams in tension; small crosses indicate the inter-section points between the experimental and the simulated curves

range of $0.3mm$ which leads to the observed linear elastic-purely plastic structure behaviour. No distinct gradual yielding of the beams is present which would lead to a more visco-elastic lattice behaviour. Thus, the input characteristics of the single beams dictate directly the system response where the composition of the beams in the lattice does not change the global lattice behaviour.

It can be seen from Figure 6.3 that the two simulations with the different loading rates prescribe a lower and upper force limit of the experiments where the tests lie between these two extremes. This observation is also valid for the lattice with small square cross-sectional beams (Figure 6.4(a)). The large scatter of the experiments can then be explained with the two different simulations and the fact that the layer deformations are not equal over the height of the structure which was already mentioned in Chapter 5.4.1. The layer with the lowest deformation rate dictates the maximum reachable force of the lattice, whereas a non-uniform deformation distribution of the layers in the lattice leads to a layer with a small deformation rate. However, the lattice can reach a higher maximum force $F_{max,lattice}$ if the deformation distribution of the layers is uniform. This statement corresponds to the simulations where the single element properties for a deformation rate of $15\mu m$ are used. The effect of varying layer properties will be investigated in Chapter 6.3.1.

The experiments are compared with both simulations which respect the single beam behaviour from the measurements with the loading rates of $5\mu m/s$ and $15\mu m/s$. It has to be mentioned that both loading rates are based on the deformation between the frame and the cross beam of the micro testing device (see Figure 4.1). The effective deformation rate of the beam with the length used in the simulations (Table 3.2) is thereby smaller than the measured deformation. The deformation rate of the beam could not be determined very accurately due to the visco-elastic material behaviour, the unknown stress distribution in the support structures and the unknown deformation of the testing frame during the single beam experiment. An approximation of the loading rate can be given when neglecting the deformation of the testing frame and assuming an uniform shape of the beam. The whole length of one beam between the centres of the support structures is 15mm. This would lead to loading rates for a beam with a length of $5mm$ which are three times smaller i.e. $1.7\mu m/s$ and $5\mu m/s$. The non-uniform shape will lead to an increase of these values. The global lattices were loaded with a loading rate of $45\mu m/s$ whereas every lattice structure has 9 layers. A uniform deformation of the structure is given when every layer deforms with a loading rate of $5\mu m/s$ i.e. with $15\mu m/s$ in the single beam experiments. Thus, the upper force limit can be calculated using the the single beam behaviour which was measured on the specimens with a loading rate of $15\mu m/s$. A non-uniform deformation of the lattice structures leads to layers with a small deformation rate ($1.7\mu m/s$) and all other layers are deformed with higher deformation rates than measured. Thus, it can be seen from Figure 6.3 that all experiments reach higher maximum forces than the simulations with a loading rate of $5\mu m/s$ which implies that no beams in the structure have a smaller deformation rate than in the single

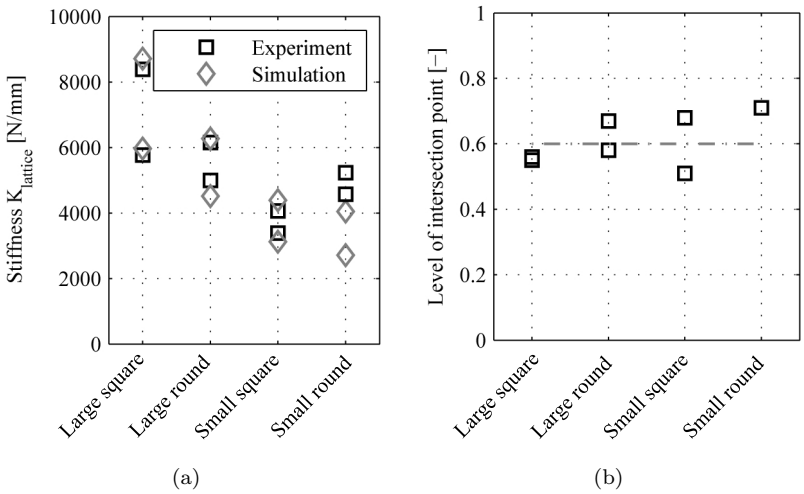

Figure 6.5.: Comparison of the global stiffness $K_{lattice}$: a) Values for all geometries, b) Intersection point of the simulated and measured curves in relation to $F_{max,lattice}$

beam experiment for a loading rate of $5\mu m/s$.

The curves from the experiments can be characterized with a visco-elastic behaviour like the single beam elements (Chapter 4.3 Equation 4.1). This leads to intersection points between the experimental curves and the simulated curves due to the linear-elastic model behaviour. The calculated stiffness for the tests and the simulations are shown in Figure 6.5(a). They are calculated between the point of origin and the point where the first beam starts to yield for the simulated curve and between the force levels $0 - 0.6 \times F_{max,lattice}$. It is obvious that the stiffness from the experiments and the simulations lie in the same range for all lattice geometries except for the lattice with small round cross-sectional beams. Lattices with this type of beam geometry reach higher values. This observation will be discussed later. The comparison confirms the model assumption that the nodal areas can be modelled as a rigid section. This reduces the complexity of the model because the stress distribution and the deformation in the nodal areas can be neglected. Another possibility to prove the assumption and to verify the calculation method of the modulus of elasticity for the single beam elements is to analyse the position of the intersection points. The curves from the experiments and simulations should intersect at a force level of $0.6 \times F_{max,lattice}$ because it has to be mentioned that the modulus of elasticity for the single beam elements was calculated between the stress levels $0 - 0.6 \times f_{pl}$ (Chapter 4.3). Figure 6.5(b) illustrates the force level where the intersection points are present for all lattice geometries. The values lie in the range of 60%; no clear tendency of a underestimation or overestimation exists. This result also points out the practicability of

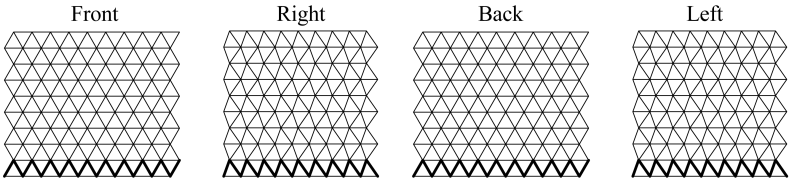

Figure 6.6.: Crack pattern of simulated lattice structure in tension

the model assumption.

It can also be seen from the comparison between the tests and the simulations that the maximum deformation at failure is substantially smaller for the simulated lattices. The large difference occurs because the main deformation in the simulated lattice takes place in the layers where the first beams start to yield due to the linear elastic-purely plastic input behaviour of the single elements. The first beams start to yield in the lowest and the topmost layer where stress concentrations are present. This results in a deformation concentration of the global lattice in these two layers. The maximum lattice deformation corresponds therefore nearly to two times of $\delta_{max,beam}$ (see model input values Appendix D.1). In the next Chapter it will be discussed which input parameters influence the maximum lattice deformation $\delta_{max,lattice}$. It is also obvious that all simulated lattices break brittle, which corresponds to the observation from the experiments. Figure 6.6 shows a typical crack pattern from a simulated lattice. The crack occurs in one layer and passes through the whole layer where it can be present at the top or the bottom of the structure. This result is in agreement with the observed crack pattern from the experiments (Chapter 5.4.1 Figure 5.7(c)). Note however that the position of the crack in the experiments varies between the first and the second layer which can be a result of a slightly eccentric loading condition.

The experimental curves from the lattices with small round cross-sectional beams show a significant difference to the simulated curves. The simulated lattice behaviour with a loading rate of $15\mu m/s$ reaches nearly $F_{max,lattice}$ of the lowest experimental curve. The values $K_{lattice}$ and $F_{max,lattice}$ are significantly higher for the experimental curves which leads to a first estimate that the loading rate of the beams in the lattice is higher than the used loading rate for the single beam experiments. This can explain the observed difference for $K_{lattice}$ and $F_{max,lattice}$. Both values increase for a visco-elastic material with increasing loading rate. This estimate has to be proven by investigating the sensitivity of the model when varying different single beam properties. The influence of an eccentric loading condition and the influence of different layer properties in the lattice has to be analysed to mark out the reason for the differences in the measured and simulated curves.

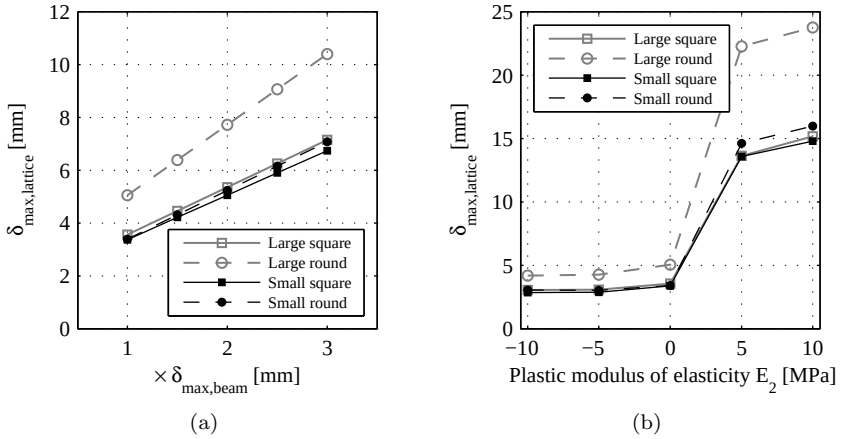

Figure 6.7.: Parameter study for varying input parameters: (a) Influence of $\delta_{max,beam}$ on $\delta_{max,lattice}$, (b) Influence of E_2 on $\delta_{max,lattice}$

6.3.1. Parameter study

The influence of several input parameters on the global lattice behaviour for the classical model will be investigated in this section in order to verify the sensitivity of the model. The influence of an eccentric loading condition and different layer properties in the lattice will be studied to evaluate the main influences on the global lattice behaviour. The geometrical model parameters stay constant in all the analyses due to the observation that the model assumption seems to be applicable (rigid node area) when comparing the modulus of elasticity from the experiments and with simulations.

Figure 6.7(a) illustrates the change of the maximum lattice deformation $\delta_{max,lattice}$ when the maximum single beam deformation $\delta_{max,beam}$ is increasing for the out-of-plane beams (30°/55° and 90°/55°). $\delta_{max,lattice}$ increases proportionally with $\delta_{max,beam}$ whereas this variation appears to have no influence on the modulus of elasticity and the maximum force of the structure for all geometries. The single beam maximum deformation shows a high scatter in the single beam element tests and could be chosen higher than assumed in the simulations in section 5.3 (see Table 3.2). This could explain the significant difference between the experiments and the simulations. The maximum deformation in the simulations is about 50% of the measured deformations. This difference corresponds to a three times higher single beam deformation capacity which is quite high. It is therefore unrealistic that this parameter has the most important influence on the deformation capacity of the global lattice.

The modulus of elasticity for the in-plane beams was set in the model according to the measured values in the single beam experiments with its specific loading

rates. It was observed in the global lattice experiments that the in-plane beams have a significant smaller deformation rate compared to the out-of-plane beams. The small deformation rate can therefore lead to a smaller modulus of elasticity due to the visco-elastic behaviour of the single beam specimens. It is clearly visible from Figure D.2(a) that a reduction has only a small effect on $F_{max,lattice}$ for all beam geometries in the lattice. The maximum force decreases at about 5% when decreasing the modulus of elasticity of the in-plane single beams to 20% of its original value. Both parameters $K_{lattice}$ and $\delta_{max,lattice}$ do not change significantly by changing this parameter. This leads to the conclusion that the modulus of elasticity for the in-plane beams has a subordinate influence on the global lattice behaviour in tension when the classical model is used.

The plastic modulus of elasticity E_2 (see Figure 2.5(b)) for the single beams was set to zero for all simulations. However, a few single beam curves show a slightly ascending plastic plateau. The influence of a varying plastic modulus of elasticity E_2 on $\delta_{max,lattice}$ is illustrated in Figure 6.7(b) where E_2 varies between $-10MPa$ to $10MPa$. It is visible from Figure 6.7(b) that a negative E_2 has a minor influence on the maximum lattice deformation whereas only a small reduction of the deformation is present for all lattices. On the other hand, $\delta_{max.lattice}$ increases rapidly between the values $0MPa$ and $5MPa$ of the plastic modulus E_2. A further increase has a minor influence on the maximum lattice deformation. This observation agrees with the statement that the whole lattice deformation is localized in the layers where the first beams start to yield when the single beam element has a linear elastic-purely plastic behaviour. An increase of E_2 for the single beams leads to an activation of the deformation capacity of the other layers. The layers where all beams have started to yield can now further increase their load whereas the beams in the other layers will reach the yield stress. All layers in the lattice will have a plastic deformation until the first beam fails which leads to a higher $\delta_{max,lattice}$. It was also observed in the experiments that every layer of the structure had a plastic deformation before the maximum deformation was reached.

The maximum force before the lattice fails varies also linearly with the change of the plastic modulus of elasticity E_2 (Figure D.2(b)). A negative value reduces the maximum force whereas a positive value increases the maximum force. This observation is clear because the global lattice behaviour corresponds to the single lattice behaviour as mentioned before. The global modulus of elasticity and the force, when the first beam starts to yield, are not influenced by the change of E_2.

The deformation behaviour of the lattice structure has therefore a linear dependency on the model input parameters apart from $\delta_{max,lattice}$ which is sensitive to small changes of E_2. This sensitivity describes a disadvantage of the classical model due to the fact that a small change in the input parameters leads to a significant change in the global lattice behaviour. The sensitivity complicates the evaluation of accurate input parameters which would lead to appropriate results.

The parameter α, which controls the amount of the beam end moments to the yield stress of an element (see Equation 2.5), was set to 1 for all simulations

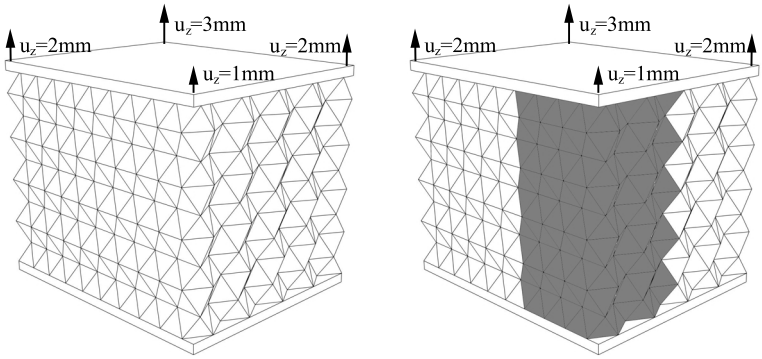

(a) (b)

Figure 6.8.: Eccentric loading condition: (a) Same single beam behaviour for all beams for a loading rate of $15\mu m/s$, (b) Beams in the grey area have single element behaviour for a loading rate of $5\mu m/s$

i.e. the moments in the beams are fully respected in the model. Neglecting the moments in the beams ($\alpha = 0$) leads to an increase of the maximal force of the lattice and a slightly increase of the maximum global lattice deformation. The modulus of elasticity is not influenced by this parameter (see Appendix D.2 Figure D.1(a)). It is not fruitful to set the parameter α differently from 1; otherwise the statics of the system are not characterised correctly.

The influence of an eccentric loading condition was investigated on a lattice with two different configurations (Figure 6.8). All single beam elements have the same properties (which corresponds to the properties measured with a loading rate of $15\mu m/s$) in one configuration (Figure 6.8(a)). One fourth of all beam elements have a smaller modulus of elasticity and yield strength (which corresponds to the single element properties measured with a loading rate of $5\mu m/s$) in the edge of the lattice with the smallest deformation rate due to the eccentric load in the second configuration ((Figure 6.8(b)). The eccentric load was applied on the lattice with a linearly changing deformation field where the maximum difference of the deformation between the edges was set to $2mm$, which corresponds to the maximum measured difference in the experiments. Figure 6.9(a) illustrates the change in the deformation behaviour of the lattice structure for both configurations. Applying an eccentric load to the lattice while leaving the single beam properties equal for all beams in the lattice leads to a slight reduction in the global modulus of elasticity. The maximum force is almost similar to these centrically loaded lattices, whereas the maximum lattice deformation is reduced when an eccentric load is applied. The maximum force and the global modulus of elasticity reach a significant lower value for the simulation in the second configuration. It can be concluded that the weakest zone in the lattice determines the global lattice

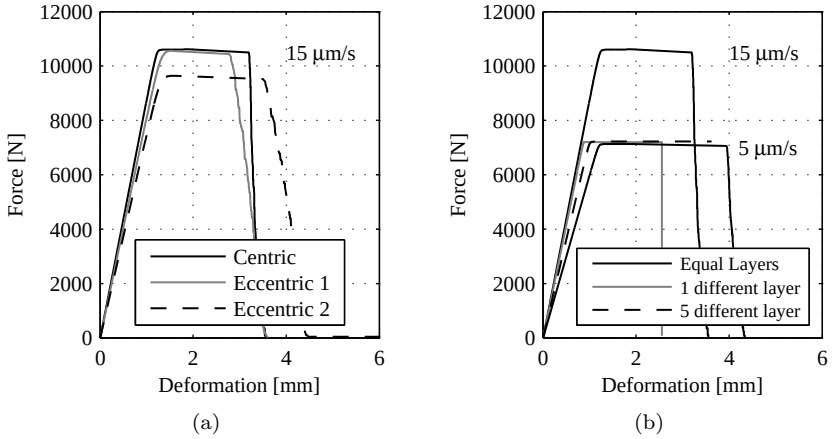

Figure 6.9.: Simulated lattice behaviour for different test configurations: a) Influence of an eccentric loading condition, b) Influence of different layer properties

behaviour, which was already mentioned. Using larger values of single element properties for the beams in the edge with the highest deformation rate does not influence the global lattice deformation significantly. The main influence on the lattice deformation has the position of the zone where the lowest deformation rate i.e. the beams with the lowest E_{beam} and f_{pl} are present.

It was observed in the experiments that the different layers in the lattice do not have the same deformation rate (Chapter 5.4.1). This circumstance can be simulated in the model by varying E_{beam} and f_{pl} for all the beams in one layer of the lattice. Figure 6.9(b) illustrates the lattice deformation where different configurations are studied. One weaker layer (E and f_{pl} corresponds to the values for a loading rate of $5\mu m/s$) is introduced in the lattice in the first configuration where the position of the weaker layer is irrelevant on the result. It is clearly visible that the structure reaches the same maximum force like the lattice which contains only weak beams. The stiffness has nearly the same value like for the lattice where the parameters for the beams with the higher loading rate are used. Changing the configuration that only one strong layer is present in the lattice reduces the stiffness to the value, corresponding to the lattice including beam properties for the smaller loading rate: the maximum force is also not influenced. Alternating the beam properties from layer to layer i.e. one weak layer is followed by a strong layer, does not change the maximum force which is defined by the weakest layer. The global modulus of elasticity for this second configuration lies in the range between the simulations for the two different loading rates. These results correspond with the conclusion from the analysis of an eccentric loading condition that the weakest zone defines the lattice behaviour, mainly $F_{max,lattice}$.

The high scatter of the maximum forces in the experiments can very likely be explained with this observation. A uniformly deformed lattice will reach a higher maximum force than a non-uniformly deformed lattice which includes one layer with a smaller deformation rate while the global deformation rate is equal for both cases. It is not possible at this time to reach a uniform deformation for the whole lattice even with a centric loading condition and a regular and precise defined lattice geometry. A small scatter in the single beam properties i.e. of E_{beam} leads already to a non-uniform deformation of the lattice. Producing a material for the single beams with exactly the same behaviour would solve the circumstance, but this seems to be hard to reach with the current production processes.

All simulations were performed without respecting the second order effect. Figure D.1(b) in Appendix D.2 illustrates the influence of the second order effect to the global lattice behaviour. It is clearly visible that the system behaves stiffer i.e. $E_{lattice}$ increases in contrary to the first order simulations. The increase of $F_{max,lattice}$ is distinct which is a result of the small modulus of elasticity for the single beam elements. Increasing E_{beam} would produce a smaller difference. It was shown from the comparison between the experiments and the simulations that the parameters from the single beam tests with two different loading rates cover the scatter of the experiments without respecting the second order effect. This solution is favourable due to an avoiding of iterations in the simulation and to keep the model as simple as possible. The impact of the second order effect in the experiment cannot be determined directly. A simulation respecting the second order effect and using input parameters for a low deformation rate would have the same result as well as a simulation without respecting the second order effect and using input parameters for a high deformation rate. The second order effect could be analysed in case of a uniform lattice deformation which is not possible in the presented experiments.

6.4. Comparison between experiments and new model in tension

Figure 6.10 and 6.11 show the comparison between the results from the new model and the measured lattice behaviour under tensile load. It is obvious that the visco-elastic behaviour of the global lattice is correctly simulated with the new model. The ascending part of the curves shows a decreasing stiffness and the simulations fit well with the experiments in this region. The two simulations with the different loading rates also describe the lower and upper force limit of the experiments except from the lattice with small round cross-sectional beam which was already mentioned before. The shape of the simulated curves matches well with the experimental curves. The slope of the curves in the plastic region of the lattice, where the force rises only slightly by increasing the global deformation, can be simulated much better than with the classical model. Especially the simulated curves from the lattices with large round cross-sectional beams (Figure 6.10(b)) fit

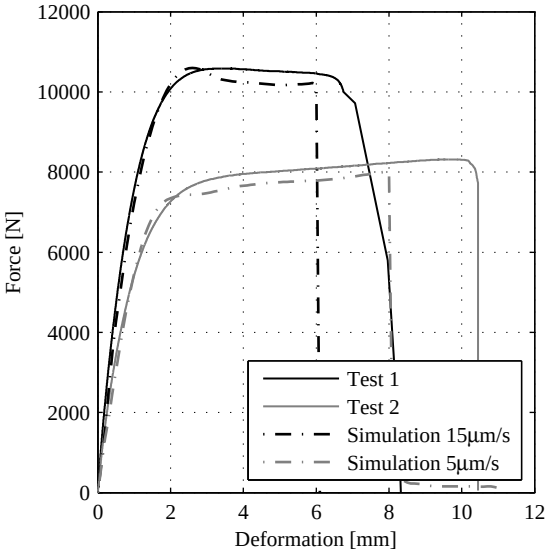

(a) Large square cross-section

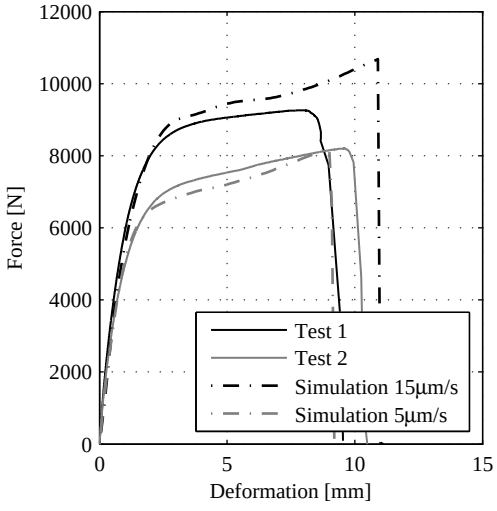

(b) Large round cross-section

Figure 6.10.: Comparison between tests and new model results for lattices with large beams in tension

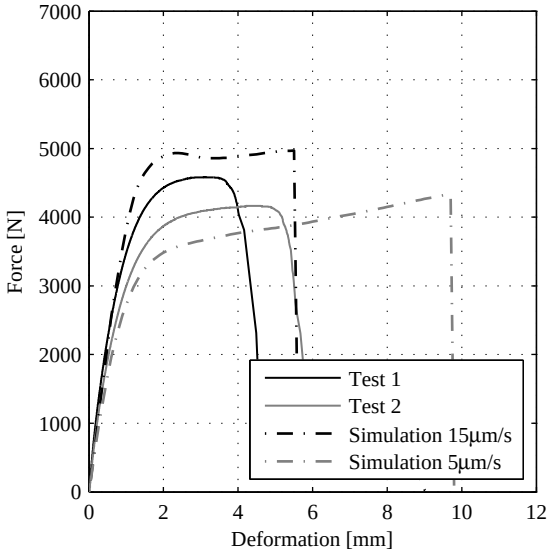

(a) Small square cross-section

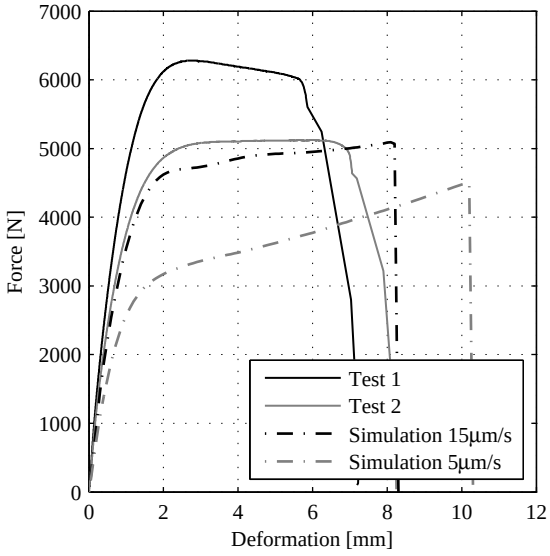

(b) Small round cross-section

Figure 6.11.: Comparison between tests and new model results for lattices with small beams in tension

better to the experimental curves i.e. result in a better curve characterisation. It is obvious that the new model approach provides the better results in comparison to the classical model whereas also the input informations for the new model can be determined much easier than for the classical model.

Also the simulated $\delta_{max,lattice}$ is more in the region of the experiments than with the classical model. The maximum deformations in the classical model had nearly the same value for the simulations with both deformation rates. They are significantly smaller than measured in the experiments. In the new model, the lattice deforms more uniformly over the whole height of the specimen which agrees with the observations from the experiments. The model does not lead to a deformation localisation in the layers where the critical beams are located. Considering directly the force-deformation curve of a single beam describes the global lattice behaviour and the deformation in the layers more accurately than in the classical model. The scatter of the measured $\delta_{max,lattice}$ and $\delta_{max,beam}$ is in general high: these values cannot be predicted very well with the models. The maximum deformation of the lattice is dependent on the first beam which reaches $\delta_{max,beam}$ and fails. The lattice will have a large maximum deformation if the beam has a high deformation capacity. Contrary, the global lattice fails at a low $\delta_{max,lattice}$ if the beam, which fails first in the lattice, has a small $\delta_{max,beam}$. A statistical distribution of the maximum deformation in the single beams would result in a scatter of the global lattice deformation where the measured deformation would be located in this scatter.

The calculated stiffness for the experiments and the simulations are shown in Figure 6.12(a). The stiffness were calculated again between 0% and 60% of the force level related to $F_{max,lattice}$ for every curve. The values are in a good agreement whereas a tendency is present that the simulations have a slightly smaller value than the experiments for all lattices with different beam geometries.

6.4.1. Parameter study

There is one parameter in the new model which can change the results apart from varying the input force-deformation curves for the single beams. The modulus of elasticity of the in-plane beams, which deform linear-elastic under the compressive load, can vary due to the small deformation rate of these beams. Figure 6.12(b) shows the dependency on the stiffness $K_{lattice}$ on a varying modulus of elasticity of the in-plane beams. The reduction of $K_{lattice}$ is obvious for all lattice geometries whereas it is more reduced for the lattices with large cross-sectional beams than for lattices with small cross-sectional beams. The value changes only slightly between $0.5 - 1.0\times$ the in-plane modulus of elasticity. A variation in this region seems appropriate for the single beam modulus of elasticity whereas a further decrease would lead to values away from the measured values.

The maximum force of the global lattice is not influenced by the variation between $0.5 - 1.0\times$ the modulus of elasticity of the in-plane beams (Figure D.3(a)) for all lattice geometries. The value $\delta_{max,lattice}$ has only a small variation between $0.5 - 1.0\times$ the in-plane modulus of elasticity (Figure D.3(b)). The dependency is

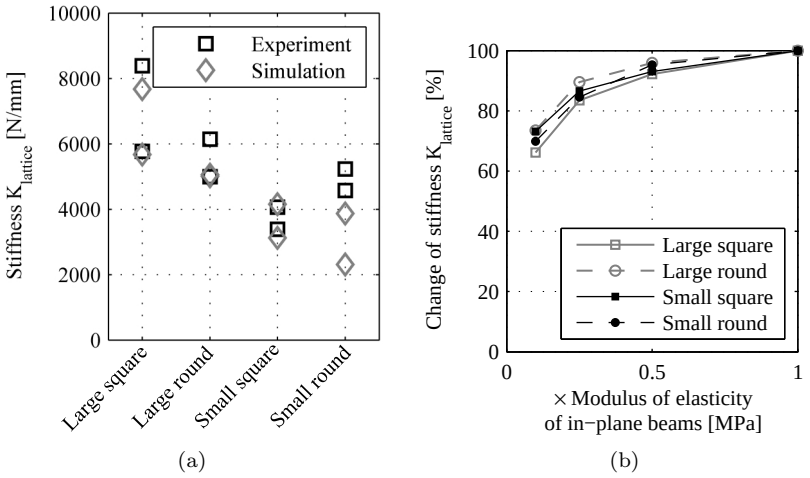

Figure 6.12.: (a) Comparison of the stiffness $K_{lattice}$ for all geometries, (b) change of stiffness $K_{lattice}$ dependent on the modulus of elasticity of in-plane beams

more distinct in the region between 0.1-0.5 where a higher deformation reduction is visible for larger lattice deformations. A modulus of elasticity for the in-plane beams in this region $(0.1-0.5)$ is again not appropriate due to the high reduction of $K_{lattice}$ as mentioned before. It is obvious that the new model is more reliable because the global lattice behaviour is not very sensitive to changes in the input parameters like in the classical model (see Figure 6.7(b)).

The V/N-ratio in all elements changes significantly while reducing the modulus of elasticity for the in-plane single beams. Figures 6.13(a) and 6.13(c) show the V/N-ratio distribution for all elements in the lattice at the beginning of the global lattice deformation depending on the in-plane single beam stiffness. It is clearly visible that more elements have higher V/N-ratios when the modulus of elasticity of the in-plane beam is reduced. It leads therefore to higher moments in the beams. Different force-deformation curves have to be used in the simulation when the V/N-ratio increases. This mechanism is negligible for a simulation of lattices under tensile load because it was shown in Chapter 4.4 that the effect of a varying V/N-ratio has a small influence on the force-deformation curve of the single beam element. It is also an explanation why the global lattice behaviour does not change significantly while varying the in-plane beam stiffness.

The V/N-ratio of the elements also changes during the simulation. Figures 6.13(b) and 6.13(d) illustrate the distribution at a global lattice deformation level of $0.5 \times \delta_{max,lattice}$ for two different in-plane beam stiffness values. The pattern of the distribution changes significantly compared to the pattern at the beginning of the global lattice deformation (Figure 6.13(a) and 6.13(c)). The scatter increases whereas lower and higher V/N-ratios are reached at this stage of deformation.

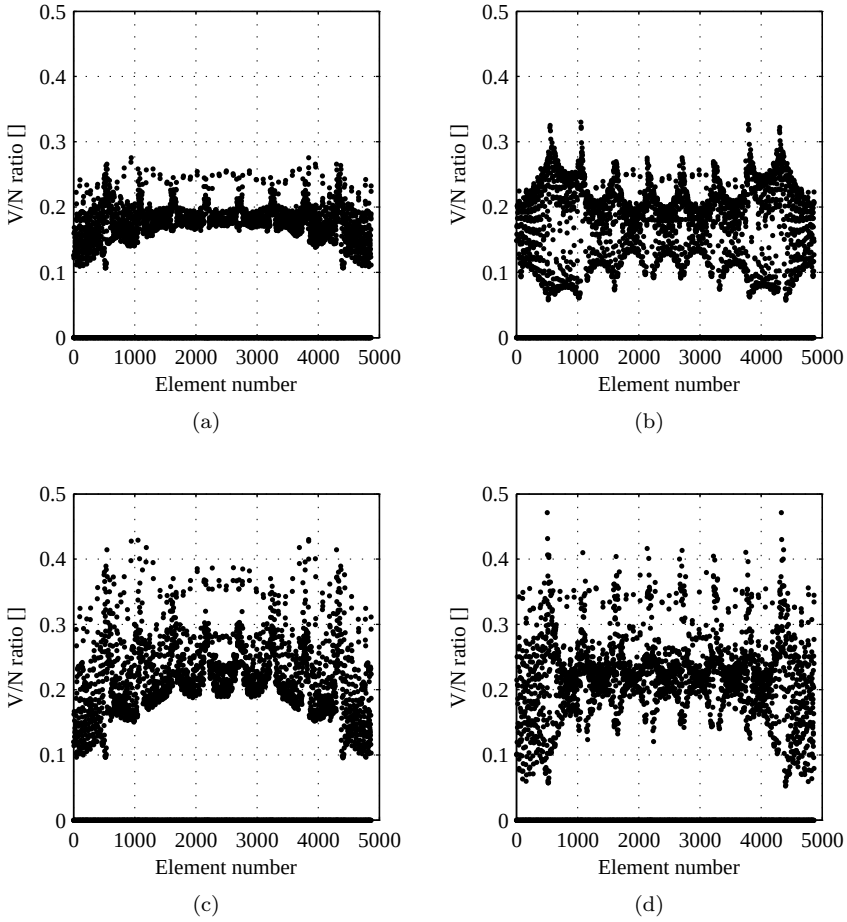

Figure 6.13.: V/N-ratio distribution at different lattice deformation levels and with varying in-plane beam stiffness: (a) 1% deformation and 100% in-plane stiffness, (b) 50% deformation and 100% in-plane stiffness, (c) 1% deformation and 50% in-plane stiffness, (d) 50% deformation and 50% in-plane stiffness

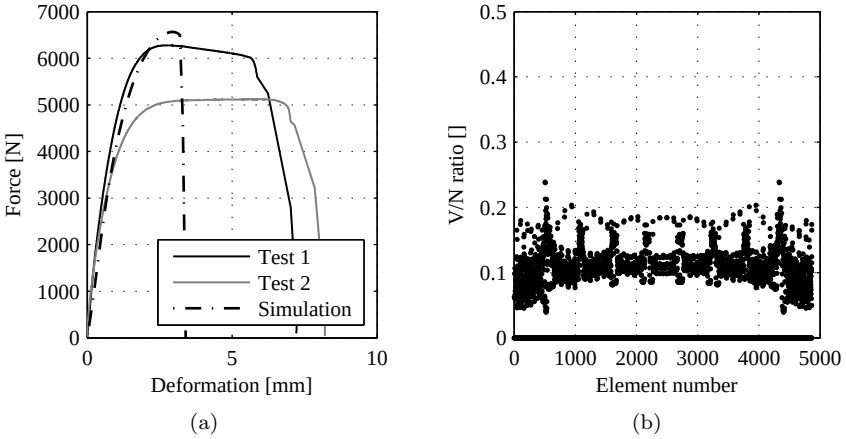

Figure 6.14.: Modified simulation for the lattice behaviour with small round cross-sectional beams: a) comparison of the lattice behaviour, b) V/N-ratio distribution at a global deformation of $0.2mm$

This behaviour is typical for lattices with a visco-elastic or linear elastic-purely plastic beam behaviour. A lattice where the beams behave only linear elastic has no change of the V/N-ratios in the elements during the whole deformation. An iterative simulation process is therefore necessary to respect the visco-elastic or linear elastic-purely plastic element behaviour since the single beam modulus of elasticity is reduced when increasing its deformation. Also this mechanism is negligible for the simulation of lattices under tensile load like mentioned before.

The influence of an eccentric loading condition and the influence of different layer properties have the same effect in the new model as in the classical model. The reduction of the parameter α would reduce the V/N-ratio in all beam elements because a reduction implies also a reduction of the end moments in the beams. This parameter can also be neglected in the new model to simulate the tensile behaviour of the lattice structures because the single beam behaviour does not change significantly while varying the V/N-ratio. It is not needed to take the second order effect into account during the simulation because it is already included in the force-deformation curves of the single beams. It is obvious that the number of parameters with an influence on the global lattice behaviour is significantly reduced in the new model due to the used input data, which reduces the complexity of the model.

The simulations for the lattice with the small round cross-sectional beams also do not reach the maximum forces of the experiments like in the classical model (Figure 6.11(b)). The simulation with the higher loading rate reaches nearly the same value for the measured maximum force and the stiffness $K_{lattice}$ like the values from the second experiment. But generally, also the high values from

the experiments can not be found with the new model. Using only the force deformation-curves of the single beam experiments with a V/N-ratio 0.4 or 0.6, which have higher maximum forces, leads to a significant increase of the reached maximum force (Figure 6.14(a)). The result of the simulation represents the measured curves better than the results from the classical and the new model as shown before. The existence of bending moments in the beams and the visco-elastic element behaviour leads to a higher reachable f_{pl} which results in higher $F_{max,lattice}$. On the other hand, it is not clear at this point why the force-deformation curves with a V/N-ratio of 0.4 have to be used to reach the measured values because the V/N-ratios in the elements lie in the region of less than 0.2 (Figure 6.14(b)). Reducing the modulus of elasticity of the in-plane beams to 25% of its original value increases the V/N-ratio of only 63 elements from 5130 elements to the desired level of 0.4 which is not sufficient to reach a global force higher than $5'000N$. It is concluded from the different investigations that the layer deformation over the whole height of the structure has to be very uniform, so that the beams were loaded with a higher deformation rate than in the single beam element tests. This results in a higher modulus of elasticity and yield strength of the single beams which leads to the measured lattice behaviour. Another possibility is that the beams in the structures had a production-related higher modulus of elasticity E_{beam} and a higher yield stress f_{pl} than in the single beam element test. More experiments on structures with small round cross-sectional beams have to be done to identify the difference between the experiments and the simulation more satisfying.

6.5. Procedure for compressive simulations

The boundary and loading conditions are set equal for both models according to the tensile simulations described in Section 6.2 (see Figure 6.1). The geometrical parameters of the single beams for both models, the single element properties for the classical model and the force-deformation curves under different V/N-ratios for the new model also correspond to the values described in Section 6.2. It has to be mentioned that the compressive modulus of elasticity was set again equal to the tensile modulus of elasticity.

The behaviour of the in-plane beams in the lattice structure (orientation $0°/0°$ and $60°/0°$), which are loaded in tension, was chosen as linear elastic-purely plastic for the classical model. The measured single element properties (modulus of elasticity E_{beam}, yield stress f_{pl} and the maximum deformation $\delta_{max,beam}$) were used to describe the behaviour where the values are listed in Appendix D.1. The yield stress f_{pl} and the maximum deformation $\delta_{max,beam}$ were set to the same values like for the out-of-plane beams ($30°/55°$,$90°/55°$) due to the small deformation rate of the in-plane beams. The measured force-deformation curves in tension for a V/N-ratio of 0.2 were applied for the new model approach.

The simulation processes for both models are described in Chapter 2.1.3. The simulation process for the new model approach could be adopted for the compressive simulations. The described classical model without modification is not

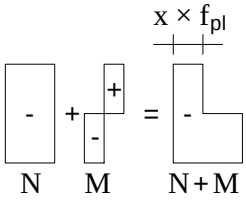

Figure 6.15.: Stress distribution in one beam segment

capable to simulate the behaviour of the lattice structures in a constructive way. The described process has one failure criterion which calculates the maximum tensile stress in all elements (Equ. 2.5). The element with the highest tensile stress is then removed from the lattice. No compressive failure criterion exists. Loading the lattice under compression leads to a failure in the in-plane beams which are loaded in tension. The load of the structure increases further even when the first in-plane beams have failed. This behaviour leads to non-realistic high maximum forces of the lattice structure until the first out-of-plane beams (orientation 30°/55° and 90°/55°) reach the failure criterion and start to yield. All beams are also divided into 0.2mm geometrical segments (Figure 3.9(b)) where the stress is calculated in every segment from the local forces of the equivalent beam in the lattice. Even taking the second order effect into account, where the moments in the out-of-plane beams are increased, leads to the same mechanism. The beams in the lattice structure have a small slenderness (see Chapter 3.4) which leads to too high forces until the beams start to buckle using linear-elastic material behaviour.

It was therefore decided to introduce a stiffness reduction of the out-of-plane beams when one segment has reached a certain stress limit. Figure 6.15 illustrates the stress distribution for the normal force N and the moment M in one segment. The stress from the moment was again calculated by dividing the moment with the plastic modulus of resistance W_{pl}. This leads to a stress distribution in the beam where the beam fibres on the tensile side can have negative or positive stresses dependent on the amount of the moment relative to the normal force. The stress on the tensile side of the beam is defined as

$$f_t = x \cdot f_{pl} \tag{6.2}$$

Six different ranges for x were chosen whereas the modulus of elasticity of the beam changes dependent on the current stress in the beam on the tensile side. Table 6.1 shows the classification of the six different ranges. No reduction of the modulus of elasticity is present when the stress on the tensile side is below $-f_{pl}$. A decrease of the modulus of elasticity is present between the stresses $-f_{pl}$ and f_{pl}. The modulus of elasticity is set to zero when the yield stress is exceeded f_{pl} which corresponds to the standard process in the classical model.

The reduction of the modulus of elasticity in the negative stress range of f_t

was chosen because only a reduction in the positive range of f_t leads to a overestimation of the maximum force of the lattice structure $F_{max,lattice}$. The stiffness reduction in the elements was calculated for a vertical lattice deformation of 10mm. The maximum moment at the end of the single element was applied over the whole length of the beam to respect the point that only one beam between two nodes is used in the simulation instead of several beams which would lead to the correct moment gradient in the element. No iterations during the simulations are necessary with this modification. Avoiding iterations in the simulation leads to an overestimation of the lattice stiffness which will be described in the next Section.

Table 6.1.: Varying modulus of elasticity dependent on x: Definition of the six different ranges

$\times E_{beam}$	x
1.0	$< (-1)$
0.75	$(-1) - (-0.5)$
0.5	$(-0.5) - (0)$
0.25	$(0) - (0.5)$
0.1	$(0.5) - (1)$
0.0	$> (1)$

6.6. Comparison between experiments and classical model in compression

Figure 6.16-6.17 show the comparison between the classical model and the measured lattice deformation under compressive load. The simulations were performed with the measured single element properties for the loading rates of $5\mu m/s$ and $15\mu m/s$. The modulus of elasticity of the in-plane beams was set to 50% for the lattices with large cross-sectional beams and 100% for the lattices with small cross-sectional beams in the Figures. It is clearly visible that the stiffness of the lattice structures is overestimated with the simulations whereas different reasons can cause this difference. The compressive modulus of elasticity was set equal to the tensile modulus of elasticity where the compressive modulus of elasticity was not measured on single beam elements and no statement can be made at this point if it is smaller than the tensile modulus of elasticity. Comparing the tests with the new model, where the force-deformation curves were measured under compression, will lead to a better estimate of this type of influence.

Figure 6.18 shows the comparison of the global lattice stiffness for the experiments and the simulations. It is visible that the values from the experiments lie in the same region for all beam geometries. A decreasing tendency is visible for the values of the simulations. The lattice with large square cross-sectional beams reaches the highest values whereas this type of beam has the smallest length be-

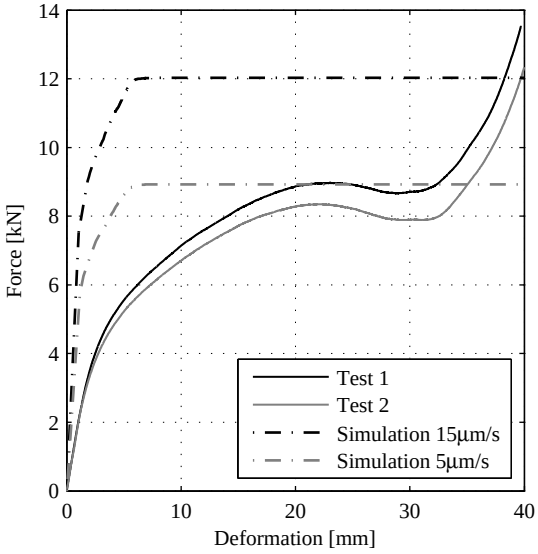

(a) Large square cross-section

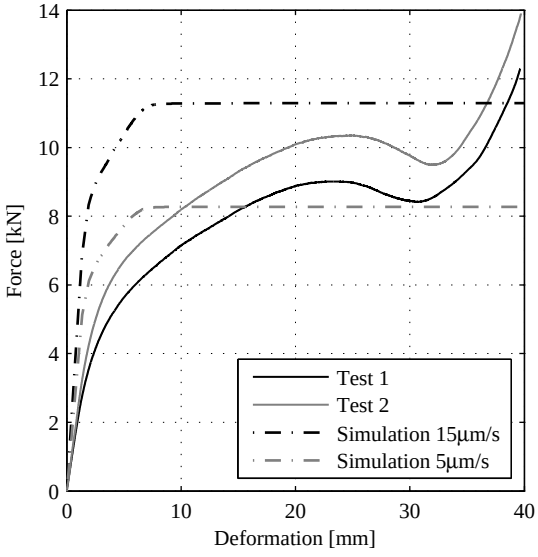

(b) Large round cross-section

Figure 6.16.: Comparison between tests and classical model results for lattices with large beams in compression

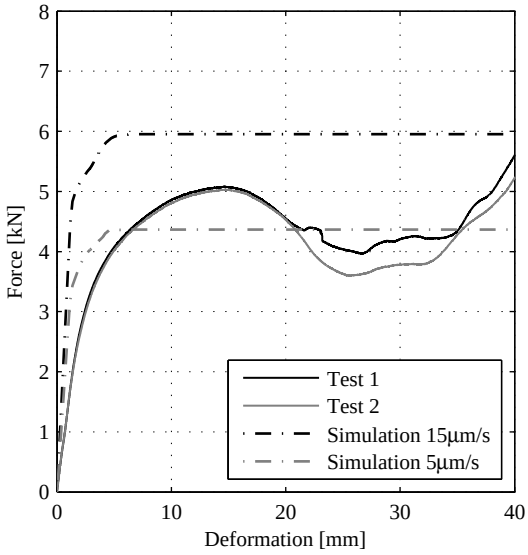

(a) Small square cross-section

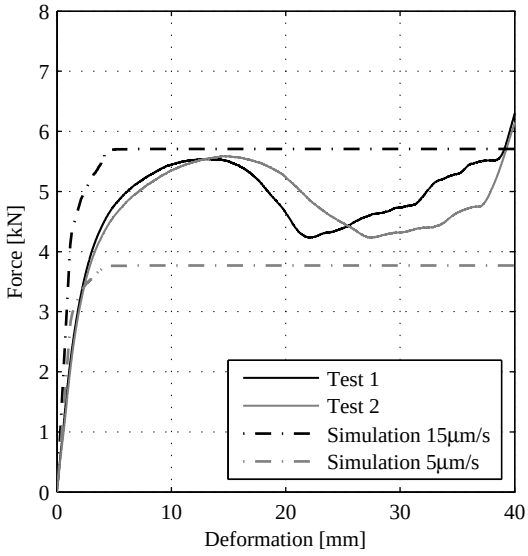

(b) Small round cross-section

Figure 6.17.: Comparison between tests and classical model results for lattices with large beams in compression

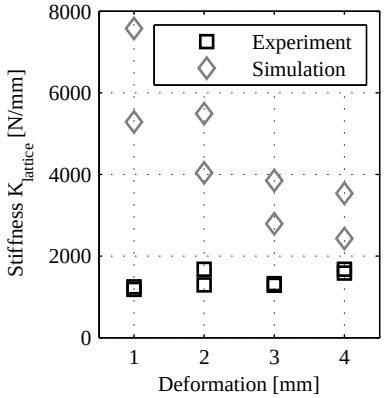

Figure 6.18.: Comparison of the global stiffness $K_{lattice}$

tween the nodal areas i.e. the smallest slenderness. Increasing the slenderness leads to a smaller lattice stiffness where the lattice with the small round cross-sectional beams has the smallest stiffness. It has to be mentioned that the modulus of elasticity of the beam E_{beam} with a small round cross-section has nearly the same value than for small square and large round cross-sections. However, the smaller length of these two beams leads to a higher lattice stiffness. It is visible from the comparison in Figure 6.6 that the stiffness from the simulation of the lattice with small round beams reach nearly the same values like the experiments. It seems that lattice structures, which include beams with a higher slenderness than used in this thesis would reach the same stiffness in the experiments and in the simulations.

The simulation process of the classical model does not use iteration processes. This leads to the fact, that no change of the modulus of elasticity of the out-of-plane beams occurs until the first beam in the lattice starts to yield. The first beam which starts to yield can be an in-plane beam under tension or an out-of-plane beam under compression. The reduced modulus of elasticity of the out-of-plane beams are taken into account in the next step. An iteration process where the reduced modulus of elasticity of the out-of-plane beams are taken into account before the first beam starts to yield could reduce the lattice stiffness. This behaviour is present for all simulated curves in Figure 6.3-6.4. A steep force increase is followed by a flattening of the simulated curves. This curve progression corresponds in general to the measured curves where a nearly linear-elastic region is followed by a flattening until the maximum force is reached. However, the curve part with the decreased stiffness proceed over a larger deformation range in the experiments whereas the deformation range between the end of the linear elastic regime and the maximum force is smaller in the simulated curves.

The mechanism after the linear elastic regime is mostly based on the yielding of the in-plane or out-of-plane beams. The modulus of elasticity of the out-of-

plane beams can be reduced every time one beam reaches the yielding stress f_{pl}. The global stiffness keeps nearly the same value over the whole flattening curve until the plastic plateau of the curve is reached. The reduction of the modulus of elasticity to zero of all out-of-plane beams occurs in a small deformation range of the lattice before the plastic plateau is reached. This region is indicated with a high curvature in the simulated curves. The out-of-plane beams can not increase their load further and the force stays constant over the whole deformation of the lattice.

All simulations do not show an ascending part after the plastic plateau. There is no implementation of a material contact behaviour in the model. The implementation would lead to a higher complexity of the model and the aim of a simple model would be missed.

The two simulations with the different loading rates prescribe again nearly a lower and upper force limit of the experiments where the simulation with the lower loading rate prescribes the force limit of the experiments for lattices with large cross-sectional beams quite well. This might indicate that the deformation of the lattice over the height was non-uniform which was already mentioned for the tensile experiments in Section 6.3. It was also observed that the strain distribution of the out-of-plane beams on the surface of the lattice under compression is non-uniform (see Figure 5.12 Chapter 5.4.2). It has to be mentioned that the beams at the surface can freely deform perpendicular to the loading direction which increases the measured strains of the beams and the scatter. The strain of the beams inside the lattice structure can not be measured. It is not possible in the case of a compressive load that the layer with the lowest loading rate prescribes the deformation behaviour of the lattice structure. The layer with the highest deformation rate first reaches the loading condition that the modulus of elasticity of the out-of-plane beams is reduced. This layer then prescribes the maximum reachable force. The layers with a low deformation rate do not reach first the loading condition i.e. a high moment at the beam ends due to the second order effect. It is however assumed that the deformation over the height is nearly uniform due to the small scatter of the experimental results. It was mentioned in Chapter 6.3.1 that the beam properties with the high loading rate are used to prescribe an uniform deformation. The simulations with a high loading rate of the single beam elements show a too high maximum force. It will be discussed in the next Section which parameter influences the force of the plastic plateau.

6.6.1. Parameter study

The influence of varying input parameters on the global lattice behaviour for the classical model will be investigated in this Section to describe the sensitivity of the model in compression. The influence of an eccentric loading was investigated for the model in tension where the characteristics keep the same in both loading conditions. All experiments in compression were loaded centrically which is indicated with the small differences between the four LVDTs in Chapter 5.4.2 which makes an analysis obsolete. An analysis of different layer properties would not

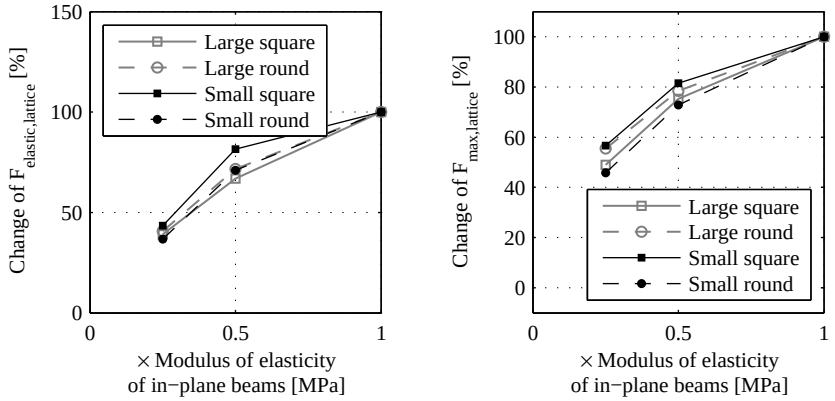

Figure 6.19.: Influence of a varying modulus of elasticity of the in-plane beams on: (a) $F_{elastic,lattice}$ and (b) $F_{max,lattice}$

lead to new insights of the mechanism different from the tensile simulations. The geometrical model parameters stay constant over all analyses.

Figure 6.19 illustrates the dependency of the force in the lattice, when the first beam starts to yield $F_{elastic,lattice}$, and the maximum force of the lattice $F_{max,lattice}$ to a varying modulus of elasticity of the in-plane beams. The analysis was performed on lattices with the single beam properties measured with a loading rate of $15\mu m/s$. It is visible that the force at the end of the elastic regime $F_{elastic,lattice}$ decreases while reducing the modulus of the in-plane beams (Figure 6.19(a)). The decrease of $F_{max,elastic}$ is constant between 25% and 100% of the original modulus of elasticity of the in-plane beams. The stiffness of the lattice structure is only slightly influenced.

The reduction of the maximum force $F_{max,lattice}$ while decreasing the modulus of elasticity of the in-plane beams is clearly visible for all lattice geometries (Figure 6.19(b)). The reduction in $F_{max,lattice}$ for all lattices occurs due to the reason that the moments in the out-of-plane beams are increasing while reducing the modulus of elasticity of the in-plane beams. The out-of-plane beams in the global lattice will preserve a larger reduction of the modulus of elasticity between the yielding of two beams i.e. two steps of the classical model. This leads therefore to smaller maximum forces of the global lattice.

It was mentioned in the last Section that the lattice deformation could be uniform where the single element properties with the higher loading rate of $15\mu m/s$ must be used. The simulation with this single element parameters leads to an overestimation of the maximum force when simulating the behaviour with the original value of the modulus of elasticity of the in-plane beams. Reducing this value leads therefore to the desired reduction of the maximum force. A reduction of the modulus of elasticity of the in-plane beams is permitted because the

strain rate is small which leads to a reduction of the modulus of elasticity for a visco-elastic material.

6.7. Comparison between experiments and new model in compression

Figures 6.20-6.21 illustrate the comparison between the results from the new model and the measured lattice behaviour under compressive load. The loading curves with different V/N-ratios show the same deformation behaviour for both loading rates (see Figure 4.17). It was therefore decided to apply the curves measured with a loading rate of $5\mu m/s$ in the model. The loading rate was also chosen from the fact that the whole structure was compressed with a loading rate of $45\mu m/s$ which results in a loading rate of $5\mu m/s$ for one layer.

The in-plane beams have a linear elastic-purely plastic behaviour whereas the modulus of elasticity and the yield stress f_{pl} were set to 50% of their original value for the calculated curves in the Figures. It was already seen from the classical model that a reduction of the modulus of elasticity of the in-plane beams leads to more accurate results. The maximum deformation at failure was set to $3.5mm$ which is higher than the measured values in the single beam element tests (see Figure 4.9). The round cross-sectional beams reach nearly the value with the loading rate of $5\mu m/s$. It is assumed that the maximum deformation at failure is higher by trend than measured when considering the small deformation rate of the in-plane beams.

It can be seen from Figure 6.20(a) that the stiffness is overestimated with the new model for lattices with large cross-sectional beams. A flattening of the calculated curve is not present and the maximum force of the structure is also overestimated. The force drop occurs at a small deformation level of the structure whereas the curves from the experiments show a decrease in force at a large deformation level. The force drop occurs in the simulation at the point when the first in-plane beams fail. This results in a change of the V/N-ratios in the out-of-plane beams whereas the V/N-ratio is increasing for the critical beams. It was seen in Figure 4.17 that an increase of the V/N-ratio leads to a reduction of the force at a certain beam deformation. The increase of the V/N-ratio leads to this steep force drop. It also has to be mentioned that only three classes of different V/N-ratios were determined i.e. the V/N-ratios of 0.2, 0.4 and 0.6. Every beam in the lattice which has a V/N-ratio below 0.3 is handled as a beam with a V/N-ratio of 0.2. The beams between the V/N-ratios of 0.3-0.5 are handled as a beam with a V/N-ratio of 0.4 etc. Only a slight change of the V/N-ratio of one beam in the lattice i.e. a change from 0.29 to 0.31 leads to a class change of the beam and therefore to a large reduction of the force.

There is only a small plateau present where the force stays nearly constant until the force starts to increase with a slightly smaller stiffness than at the beginning of the curve. The increase of the force does not occur from the material compression

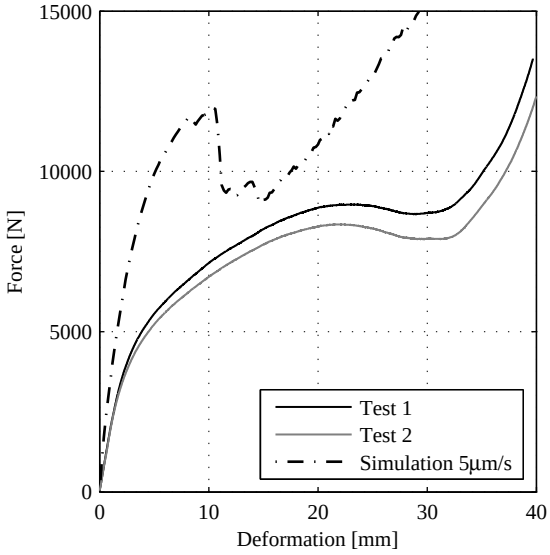

(a) Large square cross-section

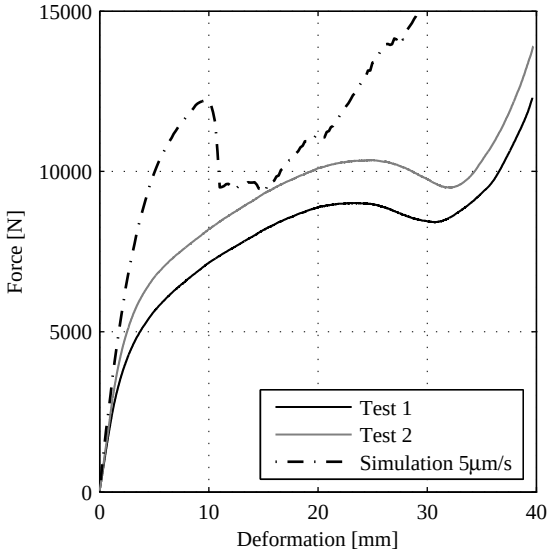

(b) Large round cross-section

Figure 6.20.: Comparison between tests and new model results for lattices with large beams in compression

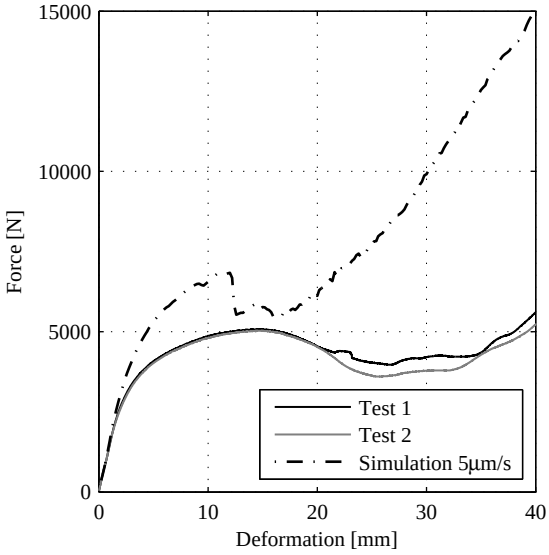

(a) Small square cross-section

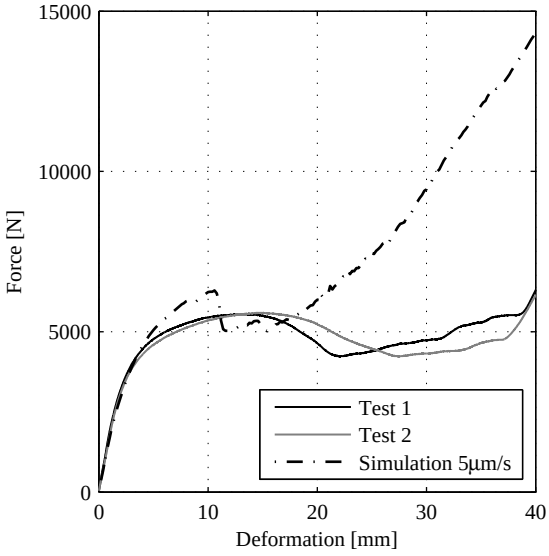

(b) Small round cross-section

Figure 6.21.: Comparison between tests and new model results for lattices with small beams in compression

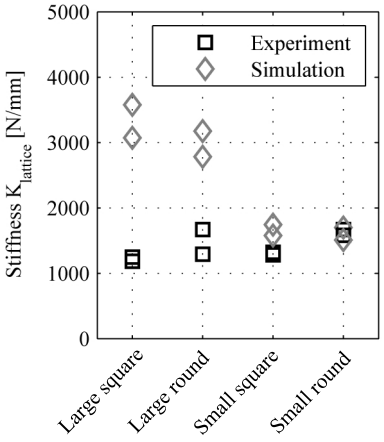

Figure 6.22.: Comparison of the global stiffness $K_{lattice}$

at this deformation level of about $15mm$ which would be the case at a deformation level of $35mm$ like in the experiments. The increase is a result from the point that most beams remain at a V/N-ratio of 0.2 whereas this single beam curve has a high increase in force also at a low deformation level (see Figure 4.17). The difference in the measured and calculated curves occurs from the fact that the beams in the lattice have a too small V/N-ratio. An increase of the values would lead to a better approximation of the simulations to the experiments. The V/N-ratio distribution for different in-plane beam properties will be discussed in the next Section.

Figure 6.21 illustrates the comparison between the experiments and the simulations for lattices with small cross-sectional beams. It is obvious that the curves fit better than for the lattice with large cross-sectional beams. The stiffness is in the same range for all curves. The maximum force is slightly overestimated for the lattice with small square cross-sectional beams whereas the maximum force from the simulation fits quite well with the experiments for the lattice with small round cross-sectional beams. The force drop in the simulations occurs again at a too small deformation level and only a small plateau with a constant force is present whereas the experiments show a long plateau. The mechanism of this observation is the same as described above. It is also visible here that the increase in force after the plateau occurs at a too small deformation level of the lattice. This is again an indication that too many beams in the lattice remained in the class with a V/N-ratio of 0.2.

Figure 6.22 shows the calculated stiffness of the experiments and the simulations. It is clearly visible that the simulations of lattices with small cross-sectional beams have nearly the same value like for the experiments. On the other hand, the simulations of lattices with large cross-sectional beams have a high difference

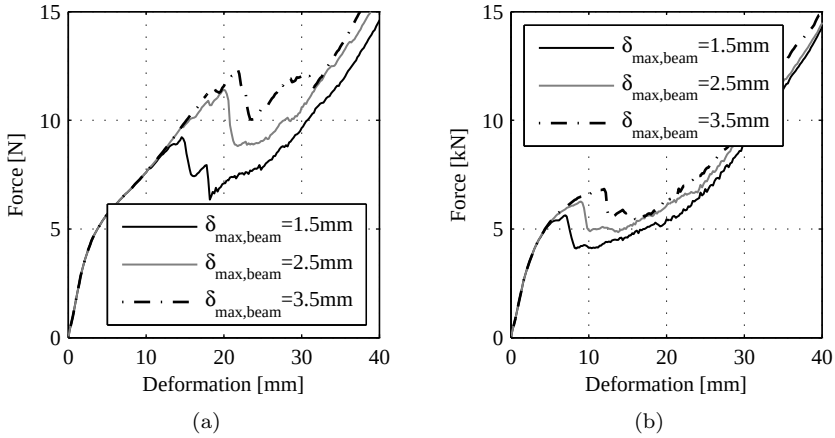

Figure 6.23.: Loading curves for varying f_{pl} of the in-plane beams: (a) $1 \times f_{pl}$, (b) $0.5 \times f_{pl}$

to the measured values. Global lattices, which contain beams with a high slenderness, show a better agreement between the experiments and the simulations than the lattices which contain beams with a small slenderness. It was also seen in Figure 6.7 that the stiffness calculations of the classical model show the same tendency. Both lattices which contain large cross-sectional beams show too high calculated stiffness with the classical model which are higher than calculated with the new model. The values from the classical model can be a product of the abstinence of an iteration process and that the compressive modulus of elasticity is smaller than the tensile modulus of elasticity. Nevertheless, this is an indication that the model assumption, where the nodal area is described as a rigid body, is not applicable in compressive simulations for lattices which contain beams with a small slenderness.

6.7.1. Parameter study

The influence of two parameters on the global lattice behaviour will be investigated in this section namely the yielding stress f_{pl} and the maximum deformation until failure $\delta_{max,beam}$ of the in-plane beams. All simulations were performed on lattice structures with small square cross-sectional beams.

Figure 6.23 shows the calculated curves for two different yielding stresses f_{pl} of the in-plane beams where the curves in Figure 6.23(a) correspond to the original yielding stress measured in the single beam tensile tests. Figure 6.23(b) corresponds to 50% of the original yielding stress. It is visible that the lattice structures, where the in-plane beams have a high yielding stress, reach the higher forces before the first beams fail in the lattice and the force drops down. The

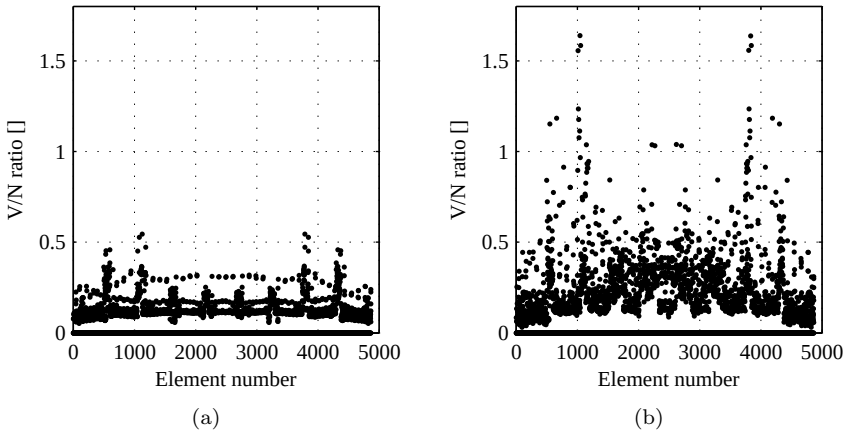

Figure 6.24.: V/N-ratio distribution for a lattice with small square cross-sectional beams at a deformation level of $20mm$ for varying f_{pl} of the in-plane beams: (a) $1 \times f_{pl}$, (b) $0.5 \times f_{pl}$

maximum deformation of the beam $\delta_{max,beam}$ influences the maximum force in the way that the reachable force decreases while reducing $\delta_{max,beam}$. The beams in the lattice change their V/N-ratio when the first in-plane beams fail. The beams with a small $\delta_{max,beam}$ fail at a low deformation level of the lattice structure where a small maximum force can be reached. The stiffness of the lattice structure is not influenced while varying $\delta_{max,beam}$.

The curves, where the yielding stress of the in-plane beams is set to 50% of its original value, show nearly the same behaviour. The main difference lies in the stiffness of the ascending curve after the linear-elastic region. The lattices with 50% f_{pl} of the in-plane beams have a smaller stiffness of the ascending curve than the lattices with 100% f_{pl} of the in-plane beams. This difference is visible when looking at the curve calculated with $3.5mm$ $\delta_{max,beam}$ and 50% f_{pl} (Figure 6.23(b)). The curve reach a maximum force of about 7kN at a deformation level of $12mm$. The curves in Figure 6.23(a) reach a force of about 8kN at the same deformation level of $12mm$. This difference occurs because more beams in the lattice with 50% f_{pl} have a higher V/N-ratio than in the lattice with 100% f_{pl}. More beams are therefore in the class with a V/N-ratio of 0.4 than in the class with a V/N-ratio of 0.2. A further reduction of f_{pl} leads to erroneous deformation patterns of the lattice where the beams can intersect each other. Comparing these results with the measurements from the experiments leads to the statement that the lattice behaviour is modelled more accurately using in-plane beams with 50% f_{pl}.

Figure 6.24 illustrates the V/N-ratio distribution for a lattice with small square cross-sectional beams at a deformation level of $20mm$ for a varying f_{pl} of the in-

plane beams. It is clearly visible that the majority of the beams in the lattice, where the in-plane beams have a yielding stress of 100%, have a low V/N-ratio i.e. a value below 0.3 even at this high level of deformation. Consequently, the whole lattice deformation is dominated by this class i.e. by the force-deformation curve of a single beam measured with a V/N-ratio of 0.2. It is therefore not possible to reach a plateau where the force is constant during the lattice deformation. Such a plateau could be reached when the V/N-ratio of the majority of the beams is in the range above 0.6.

Reducing the yielding stress f_{pl} to 50% of its original value increases the V/N-ratio in the beams which can be seen in Figure 6.24(b). The increase of the V/N-ratio in a few beams correlates with the observation mentioned above, namely, that the stiffness after the linear elastic part of the lattice deformation decreases while reducing f_{pl} of the in-plane beams. More beams reach higher V/N-ratios than 0.3 which reduces the force in the beams. However, the majority of the beams still stays in the region below a ratio of 0.3. This fact and the point that no force-deformation curves are available for V/N-ratios over 0.6, prevents that a plateau can be reached in the simulations. Again, a further reduction of the yielding stress of the in-plane beams would lead to erroneous deformation patterns of the lattice.

6.8. Discussion and conclusion

The deformation behaviour from the experiments of lattice structures with four different beam geometries was compared with the classical model and the new model approach under tensile and compressive load in this Chapter.

The following points were observed for both models in the case of tensile load:

- The input characteristic of the single beam properties dictates directly the system response of the model (modulus of elasticity E_{beam}, yielding stress f_{pl} and the maximum deformation at failure $\delta_{max,beam}$ for the classical model and the visco-elastic force-deformation curves for the new model approach). The classical model describes a nearly linear elastic-purely plastic global lattice behaviour, whereas the experiments show a visco-elastic global lattice behaviour. The new model approach leads to satisfactory results because the visco-elastic lattice behaviour is included in the input force-displacement curves.

- The simulations with different single element properties, which were measured on single beams with two different loading rates, prescribe a lower and an upper force limit of the experiments. The simulations with the single beam properties measured with a loading rate of $5\mu m/s$ prescribe the lower force limit. Lattice structures with a non-uniform deformation over the height reach this limit because the layer with the lowest deformation rate dictates the maximum force $F_{max,lattce}$. The upper force limit is reached

from lattice structures which deformly uniform over the height of the structure, viz. every layer reaches its force capacity. Specimens, which are loaded eccentrically, lie between the two force limits of the simulations.

- The stiffness of the simulations and the experiments lie in the same region for all lattice structures expect from the lattices with small round cross-sectional beams which have a higher stiffness than calculated. The agreement between the simulations and the experiments is an indication that the model assumption, where the nodal areas are modelled as rigid sections, seem applicable for all lattice geometries loaded in tension. The intersection point between the experimental and calculated curves for the classical model lies at a force level of about 60% of the measured curves. This observation confirms the calculation method of the modulus of elasticity of the single beams where the value was calculated between 0% and 60% of the maximum force.

  The force-deformation curves for the new-model approach had to be corrected to reach nearly the same stiffness like in the experiments. The support structures increase the measured deformations which would lead to too small stiffness from the simulations without a correction. Using a material with a higher stiffness for the support structures than the same like the tested specimen would prevent this source of error.

- The fracture pattern of the simulations and the experiments agrees: cracking occurs at the lowest or the topmost layer in the simulations.

- Lattices with small round cross-sectional beams reach higher forces and stiffness than expected from the simulations. The higher forces and stiffness of the global lattice can be a result of the visco-elastic material behaviour of the single beam elements where beams with high end moments reach higher f_{pl}. This is indicated when analysing the force-deformation curves for different V/N-ratios. The single element shows an increase of the yielding force while increasing the V/N-ratio. This could be the reason why the lattices with this beam geometry present a higher stiffness and higher maximum forces than the simulations. Using only the force-deformation curves of the beams with a V/N-ratio of 0.6 increases both parameters to a realistic result. However, V/N-ratios of 0.6 for all beams can not be reached even when reducing the modulus of elasticity of the in-plane beams to 25%. Another possibility is that the beams in the tested lattice could reach higher forces than measured in the single beam experiments. The exact reason for this behaviour is therefore unclear.

One parameter in each model has a main influence on the simulated global lattice behaviour under tensile load:

- The most critical parameter in the classical model is the plastic modulus of elasticity E_2 of the single beam behaviour. Only small lattice deformations

occur when the parameter is set to zero because only the layer, where the first beam starts to yield, deforms plastic until the lattice breaks. The maximum lattice deformation is therefore underestimated. Only a slight positive change of this parameter leads to a significant increase of the maximum lattice deformation. All layers can deform plastic in this case which was also observed in the experiments. However, the maximum lattice deformation is then overestimated. The model is therefore sensitive to small changes of this parameter which is seen as a disadvantage of the classical model.

- The modulus of elasticity of the in-plane beams in the lattice (orientation $0°/0°$ and $60°/0°$) is the only parameter which can change the lattice behaviour i.e. the stiffness, the maximum force and the maximum deformation of the lattice in the new model approach. The model reacts not sensitive to changes of this parameter in the range of 25%-100% of its original value. The modulus of elasticity of the in-plane beams changes the V/N-ratio distribution of the beams in the lattice in such a way that a reduction of the modulus of elasticity leads to higher V/N-ratios in the beams.

The following points were observed for the compressive simulations:

- Classical model:

  The classical model must be extended with a reduction of the modulus of elasticity of the out-of-plane beams for the compressive simulations to reach more realistic results compared with the experimental measurements. Using the classical model without extension leads to non-realistic high maximum forces even when the second order effect is taken into account. The results from the classical model calculated with the single beam properties from the two different loading rates describe again a lower and upper force limit of the experimental values. The deformation mechanism of the lattice under compression is however not equal to the mechanism under tension. The layer with the highest deformation rate prescribes the lattice behaviour contrary to the case in tension where the layer with the lowest loading rate prescribes the lattice behaviour. The beams in the layers with a high deformation rate first reach the loading condition where high end moments are present, which leads to a reduction of the modulus of elasticity and a weaker layer behaviour. A small scatter of the measurements is present although a non-uniform deformation of the global lattice was observed.

  The stiffness of the lattices is overestimated with the classical model due to a prevention of iterations. An iteration would take the reduced modulus of elasticity of the out-of-plane beams into account which would reduce the stiffness until the first in-plane beam in the lattice starts to yield. There is also a tendency that the calculation of the stiffness for lattices, which contain beams with a large length i.e. with a high slenderness, leads to better results than for lattices which contain beams with a small slenderness.

A reduction of the modulus of elasticity of the in-plane beams decreases the force where the first beam in the lattice starts to yield $F_{elastic,lattice}$ and the maximum force of the lattice structure $F_{max,lattice}$ significantly. The stiffness is only slightly influenced by this parameter. The reduction of the modulus of elasticity of the in-plane beams leads to higher moments in the out-of-plane beams. This reduces both parameters $F_{elastic,lattice}$ and $F_{max,lattice}$ due to yielding of the out-of-plane beams at a smaller global force level. It is therefore possible to preserve the maximum forces of the experiments from the simulations with the higher deformation rate with a reduction of the modulus of elasticity of the in-plane beams. This parameter has a large influence on the lattice behaviour in compression where the lattice behaviour in tension is only influenced marginally.

The classical model without modifications is in general not applicable for the simulations in compression. Several modifications would be necessary like a material contact rule and a reduction of the modulus of elasticity of the in-plane beams to model the lattice behaviour more accurately. Consequently, there is a risk that new parameters would make the model more sensitive as it is actually, that the complexity is growing and that a several parameters have to be determined empirically.

- New model approach:

  The results from the new model approach show the same tendency. The stiffness is overestimated for the lattices which contain large cross-sectional beams whereas the stiffness from the experiments and the simulations are in agreement for lattices which contain small cross-sectional beams. A reduction of the modulus of elasticity and the yielding stress of the in-plane beams do not influence the stiffness. An influence is visible in the ascending part after the nearly linear elastic region whereas a reduction of both parameters leads to a decrease in stiffness of the ascending part. The reduction in stiffness of the ascending part is aspired because it reduces the maximum force $F_{max,lattice}$ and the simulations are in better agreement with the experiments. However, the V/N-ratios in the beams of the lattice have too small values to reach the desired lattice behaviour even when reducing the modulus of elasticity and f_{pl} of the in-plane beams.

It can be concluded for the tensile loading condition that the model assumption (the nodal area can be modelled as a rigid section) are valid both for the classical model and the new model approach. This is indicated due to the agreement of the measured and simulated stiffness for both models. The model assumption does not seem to work for compressive loading conditions, both for the classical model and the new model approach due to overestimation of the stiffness of the global lattices, especially those that contain beams with a low slenderness.

Therefore, the nodal area deformation has to be taken into account which changes the element geometry for the single element experiments. Using a linear elastic or a linear elastic-purely plastic material with a high viscosity factor for all

specimens would help to separate the influence of the geometrical and the single element properties to the global lattice behaviour.

7. Conclusion and outlook

The deformation behaviour of lattice structures under tensile and compressive load was investigated in the preceding Chapters. Two different models were used to simulate the deformation behaviour namely the classical model, where the single beam element properties had to be evaluated (modulus of elasticity E_{beam}, yield stress f_{pl} and the maximum deformation $\delta_{max,beam}$) and the new model approach, where the complete force-deformation curves under different loading conditions of the single beam elements form the basic input parameters which was first hypothesized by Van Mier (2007, 2012, 2013). The Polyjet technology which uses acrylic photopolymer as building material was chosen to produce the specimens for the single beam elements and the lattice structures.

The conclusions are as follows:

- *Influence of the single element geometry on the single element properties*

  The material shows a distinct visco-elastic behaviour. Therefore, it was necessary to test the single beams with two different loading rates to obtain a sufficient database of element properties for the simulations. The tested single beam elements with the four different shapes show a distinct size and shape effect on the element properties. Universal material parameters for the classical model could not be determined at this scale of the tested specimens which lie in the mm range. The material properties are subsequently influenced by the geometry of the specimen. It is therefore necessary to determine the element properties when changing the beam geometry in the lattice structure for the classical model. The single beams show also an anisotropy dependent on the orientation in the lattice which is a product of the layered production process. Note that all Rapid Prototyping processes are based on this production method.

- *Video image correlation*

  Video image correlation was successfully adopted to determine the modulus of elasticity of the single beam elements. The assumption for both models that the nodal area of the lattice structure can be modelled as a rigid section was also successfully confirmed using VIC. A non-uniform deformation behaviour of the global lattice under tensile and compressive load was determined using VIC.

- *Global lattice experiments*

  The global lattices loaded in tension show a non-uniform deformation over the whole height i.e. the layers have different loading rates. This leads

to a high scatter in the measured maximum forces. The layer with the lowest loading rate prescribes the force capacity of the structure which is a consequence of the visco-elastic material behaviour. The lattice fails in the weakest layer which corresponds to the weakest link theory by Weibull (1939). It is therefore necessary to measure the needed input parameters using different loading rates to cover the scatter of the experiments. The global lattices loaded in compression show a small scatter in the results whereas also a non-uniform deformation over the height was measured. Contrary to the tensile experiments, the layer with the highest deformation rate prescribes the force capacity of the lattice because the beams with the largest deformation first start to buckle.

- *Comparison of the experiments and the simulations under tensile load*

  The results from the classical model and the new model approach are in agreement with the experiments under tensile load where the new model approach reproduces the deformation behaviour of the lattice more precisely. It is capable to characterize the visco-elastic deformation behaviour whereas the classical model shows a linear elastic-purely plastic deformation behaviour of the lattice structure. The input characteristic of the single beam elements prescribe directly the structural behaviour in both models.

  The lattices which contain beams with a high slenderness show higher maximum forces in the experiments than calculated in both simulations. It is assumed that this observation is also a product of the visco-elastic material behaviour because the moments in the beams increase locally the loading rate at the outer fibres of the elements which increases the yield stress of the beams. This behaviour of the beams with a high slenderness could be observed in the single beam experiments for the new model approach. A higher maximum force is reached with an increase of the moment in the beams i.e. an increase of the V/N-ratio. This leads to the higher measured forces of this type of lattice structures than expected with the classical simulation where the yield stress was determined on centric tensile experiments.

  The classical model is more sensitive to changes of the input parameters especially when changing the stiffness of the plastic part of the single element behaviour. Only a small variation leads to a distinct change of the maximum lattice deformation where the lattice fails. The new model approach does not show such sensitivity to changes of the input parameters. This makes the new model approach more reliable.

- *Comparison of the experiments and the simulations under compressive load*

  The simple classical model is not capable to simulate the deformation behaviour of the lattice structures under compression. The measured deformation behaviour could not be simulated satisfactory even when taking the second order effect into account. One modification was introduced in the model namely the modulus of elasticity was reduced dependent on the stress

in the outer fibre of the beam loaded in compression in order to obtain a sufficient deformation behaviour with this type of simulation. The stiffness and the maximum forces of the lattices are however overestimated. More modifications would be needed to obtain a more realistic deformation behaviour like a contact rule of the elements. A substitution of one element with more elements could also lead to better results where the second order effect would be taken into account in a more realistic way. This approach was successfully applied by Jang and Kyriakides (2009b) on open-cell foams which have a cellular structure consisting of beams with high slenderness.

The new model approach shows a better agreement with the experiments especially for lattice structures which contain beams with a high slenderness. The simulations of lattices which contain beams with a small slenderness show also too high stiffness and maximum forces of the structure. The stiffness of the different lattices are in the same order in both models especially for lattices which contain beams with a small slenderness. One reason for overestimating the stiffness could be that the beams in the global lattices were geometrically imperfect which would reduce the measured stiffness.

The results of both models are strongly dependent on the element properties of the in-plane beams loaded in tension. The properties of these beams influence the maximum reachable force and the deformation behaviour after the maximum force. The in-plane beam properties are difficult to determine due to the visco-elastic material behaviour. These beams have a low deformation rate compared with the out-of-plane beams loaded under compression.

The separation of the influence of the geometrical and single element parameters on the structural behaviour could not be solved in this work for lattices under compressive load. The visco-elastic material behaviour prevents a clear determination of the needed parameters. The high stiffness of the simulations in compression indicates that the geometrical parameters have to be readjusted to take the deformation of the nodal area into account for both models.

The new model approach shows a high potential for the application of fracture modelling, especially to improve the understanding of the fracture process under compressive load. The determination of the material properties (which are directly influenced by the geometry of the elements) has become obsolete with this model whereas the deformation behaviour has to be measured for beams under different loading conditions.

Outlook and recommendations

It is highly recommended to change the used material with a high viscosity for all specimens to a material with a low viscosity i.e. a material which does not change the material behaviour while changing the loading rate like aluminium. Rapid Prototyping has a high potential to produce complex structures but an anisotropy would be present for all different processes at this scale of element size which was used in this work due to the layered production process. Negative

form processes show a higher potential to produce lattices with a homogeneous material behaviour whereas ceramics or aluminium could be used to build the structures. The anisotropy of the single beams can then be circumvented. Meisel et al (2012) investigate a process to produce regular lattice structures by using a negative form of sand which is produced by means of Rapid Prototyping.

The elimination of the anisotropy and the loading rate dependency of the single element properties would lead to a better separation of the model parameters which influences the global lattice behaviour. The influence of the second order effect and the determination of the node rigidity, i.e. the amount of the end moments of the beams which has to be taken into account to calculate the stresses in the beams, could be better investigated and separated in the classical model. The geometrical parameters for the classical model and the geometry of the single beam elements for the new model approach can then be better determined when the single element properties of the in-plane beams are definitely known especially under compressive load. A readjustment of the single beam geometry for the new model approach, which takes the knot geometry into account, is necessary to reach better numerical results. It is therefore also recommended to construct a micro-testing device where the specimen can also be loaded with end moments to preserve the load-deformation curves.

Avoiding the high viscosity of the material would also lead a small scatter in the measured maximum forces of the global lattice under tensile load because a non-uniform layer deformation over the height of the lattice would have no influence to this value.

The interaction between two different beams, produced with different materials, has to be investigated in order to adopt the new model approach to disordered materials where the heterogeneity of the material has to be taken into account like in the classical model. This should finally lead to a more realistic fracture behaviour of the material where the crack pattern of the simulation can indicate the applicability of the new model approach.

A. Tables and figures from specimen production and generation

A.1. STL-file export parameters

Table A.1.: Rhinoceros $V5.0$ export parameters for stl-files

	Value
Density	0.0
Maximum angle	0.0
Maximum aspect ratio	6.0
Minimum edge length	0.0001
Maximum edge length	0.0
Maximum distance, edge to surface	0.01
Minimum initial grid quads	0.0

A.2. Global lattice geometries for different beam shape

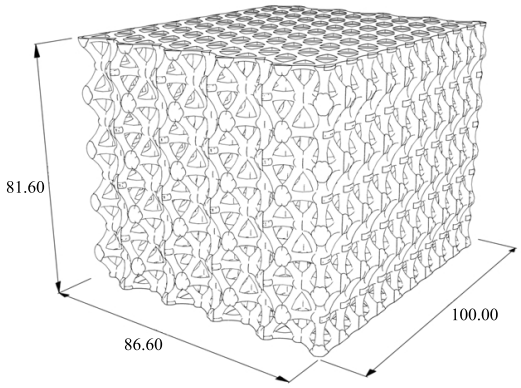

Figure A.1.: Lattice geometry containing large round cross sectional beam elements Dimensions in [mm]

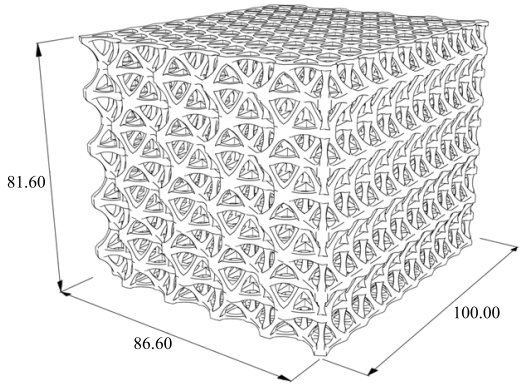

Figure A.2.: Lattice geometry containing small square cross sectional beam elements; Dimensions in [mm]

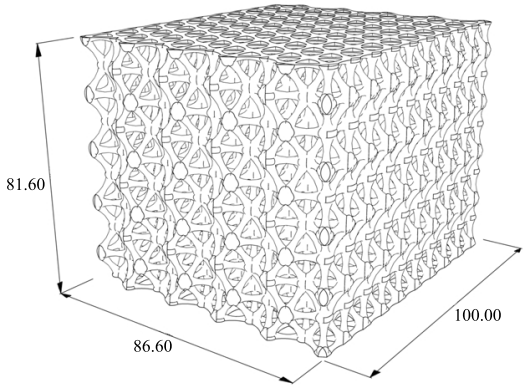

Figure A.3.: Lattice geometry containing small round cross sectional beam elements; Dimensions in [mm]

B. Tables and figures from experimental results

B.1. Measured loading curves for different specimen geometries

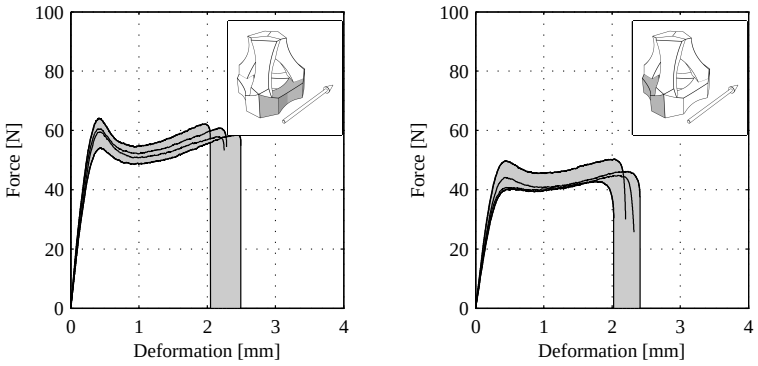

(a) Orientation 0°/0°

(b) Orientation 60°/0°

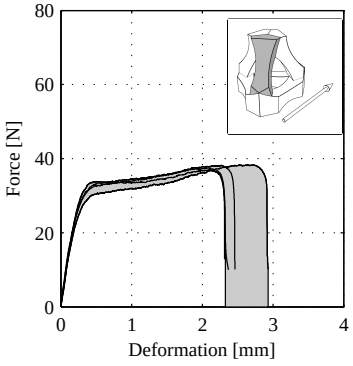

(c) Orientation 30°/55°

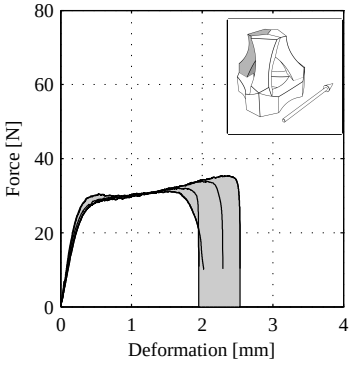

(d) Orientation 90°/55°

Figure B.1.: Load curves in tension for different beam orientations with large square cross section and loading rate of $5\mu m/s$

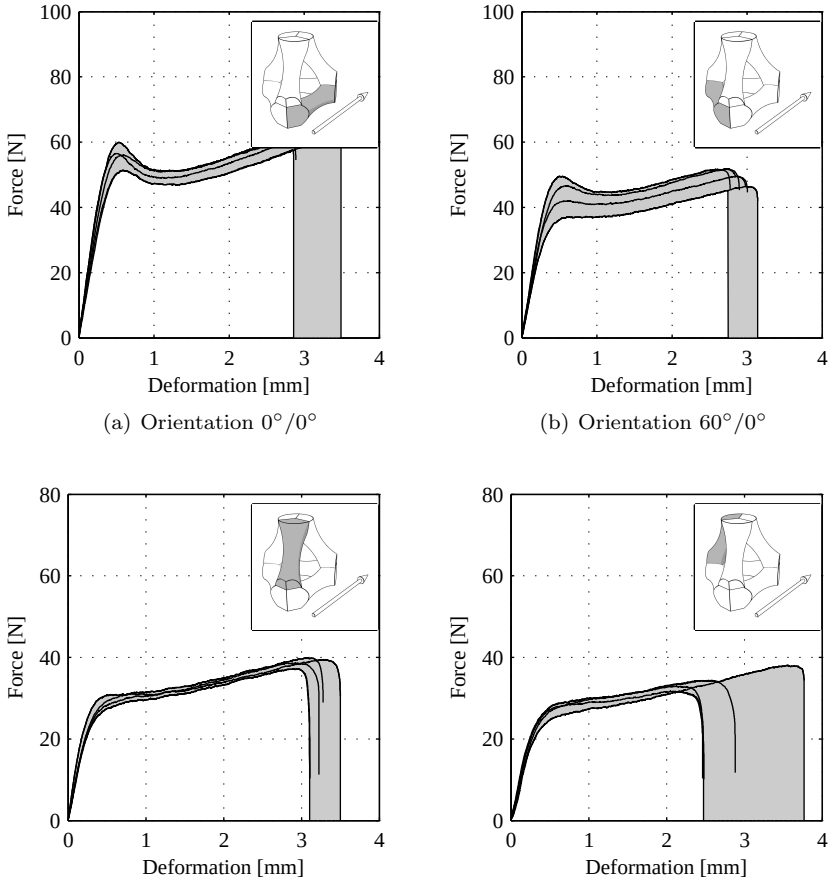

(a) Orientation 0°/0°

(b) Orientation 60°/0°

(c) Orientation 30°/55°

(d) Orientation 90°/55°

Figure B.2.: Load curves in tension for different beam orientations with large round cross section and loading rate of $5\mu m/s$

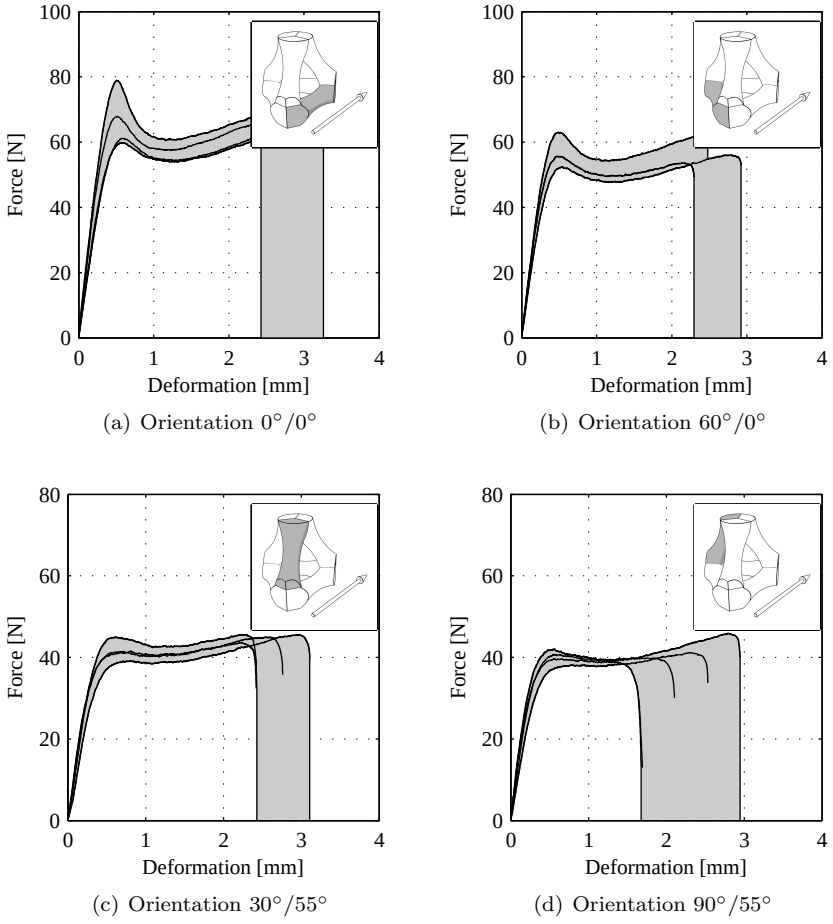

(a) Orientation 0°/0°

(b) Orientation 60°/0°

(c) Orientation 30°/55°

(d) Orientation 90°/55°

Figure B.3.: Load curves in tension for different beam orientations with large round cross section and loading rate of $15\mu m/s$

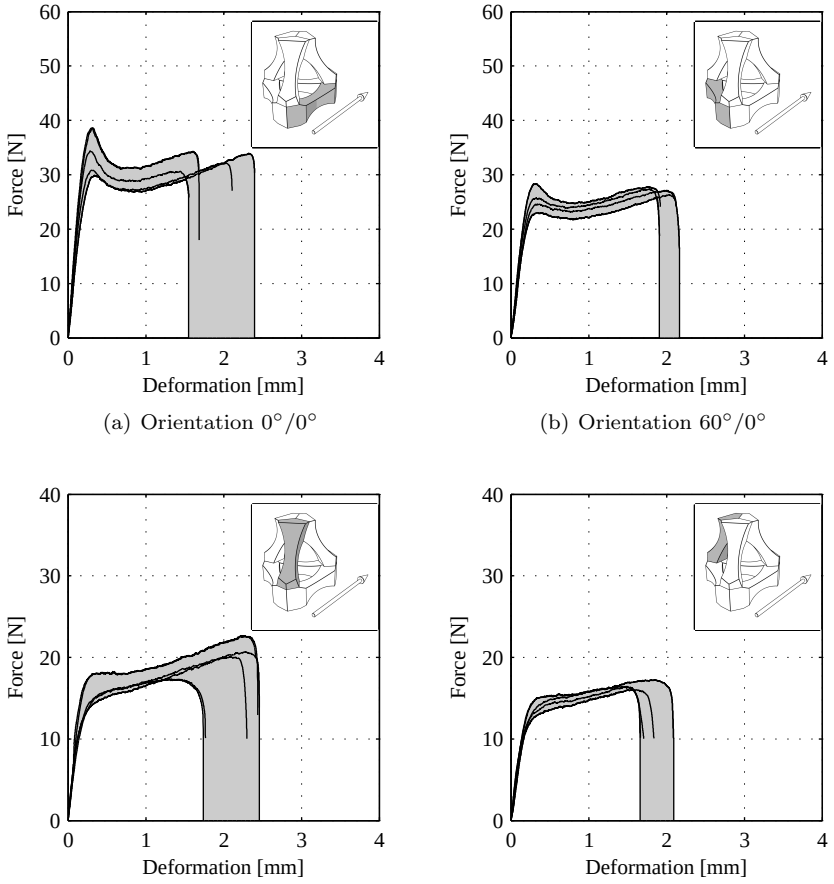

(a) Orientation 0°/0°

(b) Orientation 60°/0°

(c) Orientation 30°/55°

(d) Orientation 90°/55°

Figure B.4.: Load curves in tension for different beam orientations with small square cross section and loading rate of $5\mu m/s$

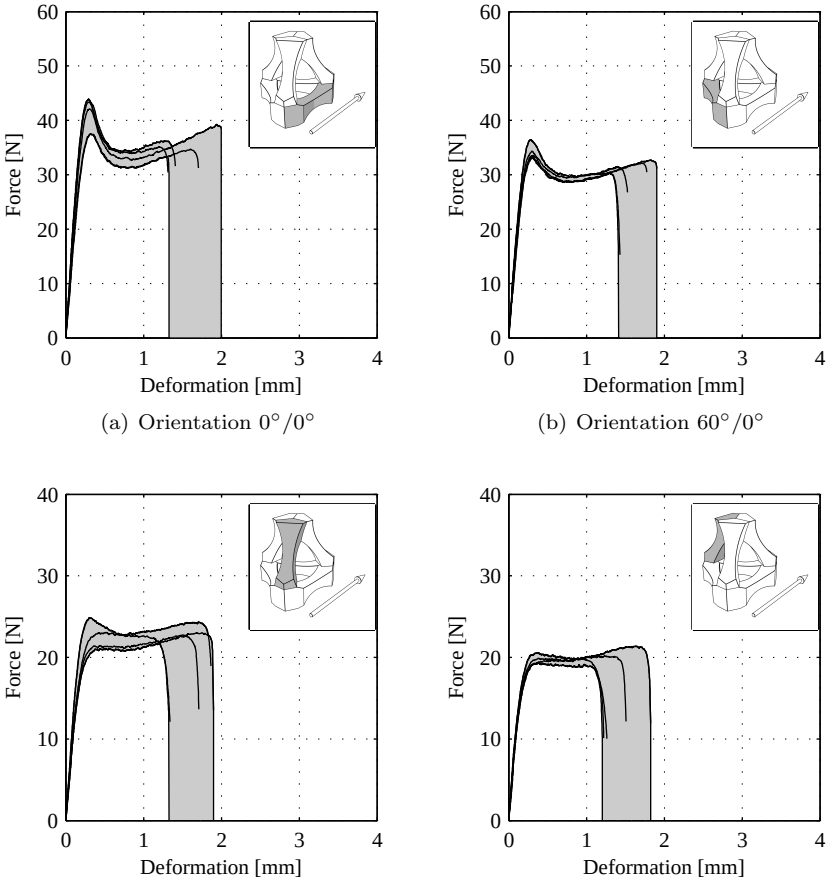

(a) Orientation 0°/0°

(b) Orientation 60°/0°

(c) Orientation 30°/55°

(d) Orientation 90°/55°

Figure B.5.: Load curves in tension for different beam orientations with small square cross section and loading rate of $15\mu m/s$

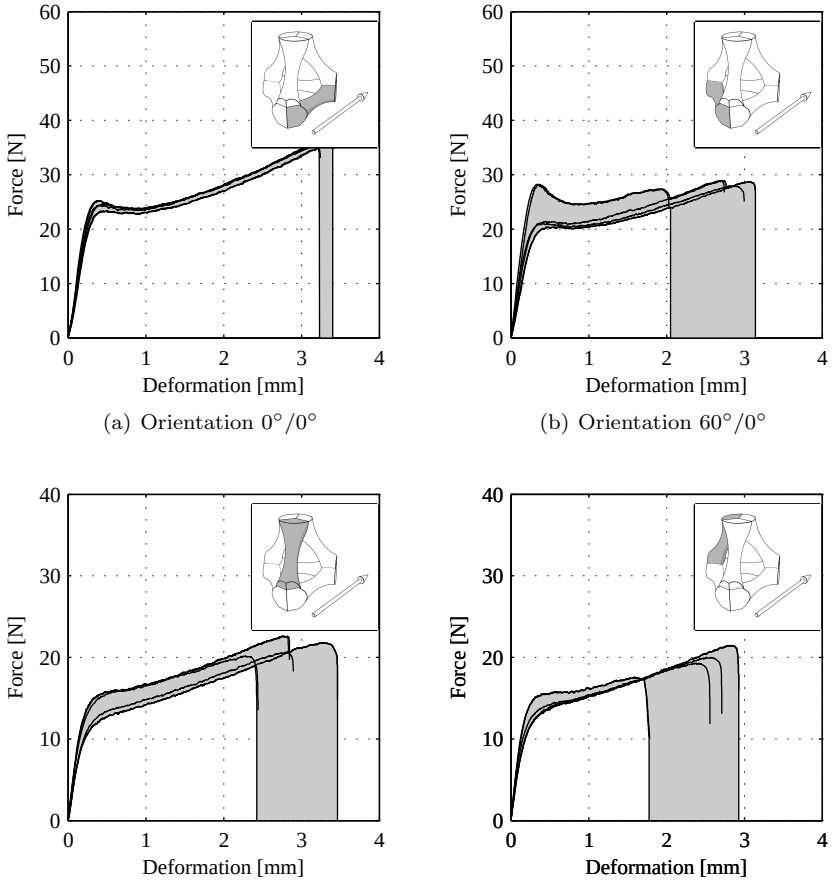

(a) Orientation 0°/0°

(b) Orientation 60°/0°

(c) Orientation 30°/55°

(d) Orientation 90°/55°

Figure B.6.: Load curves in tension for different beam orientations with small round cross section and loading rate of $5\mu m/s$

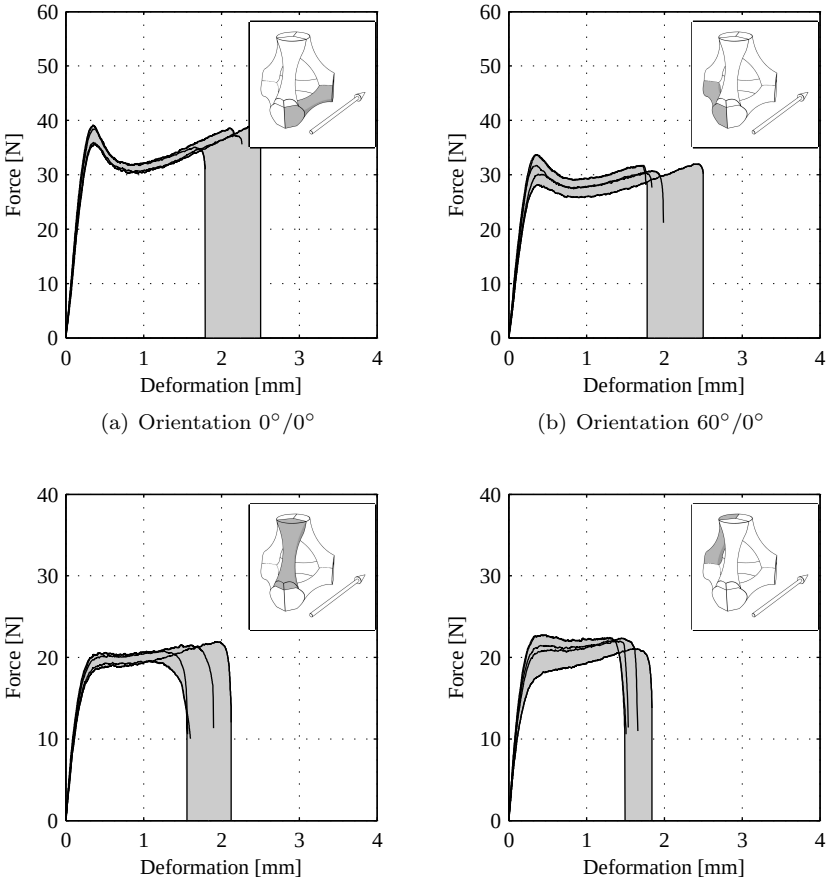

(a) Orientation 0°/0°

(b) Orientation 60°/0°

(c) Orientation 30°/55°

(d) Orientation 90°/55°

Figure B.7.: Load curves in tension for different beam orientations with small round cross section and loading rate of $15\mu m/s$

B.2. Force-deformation curves for specimens with orientation $90°/55°$

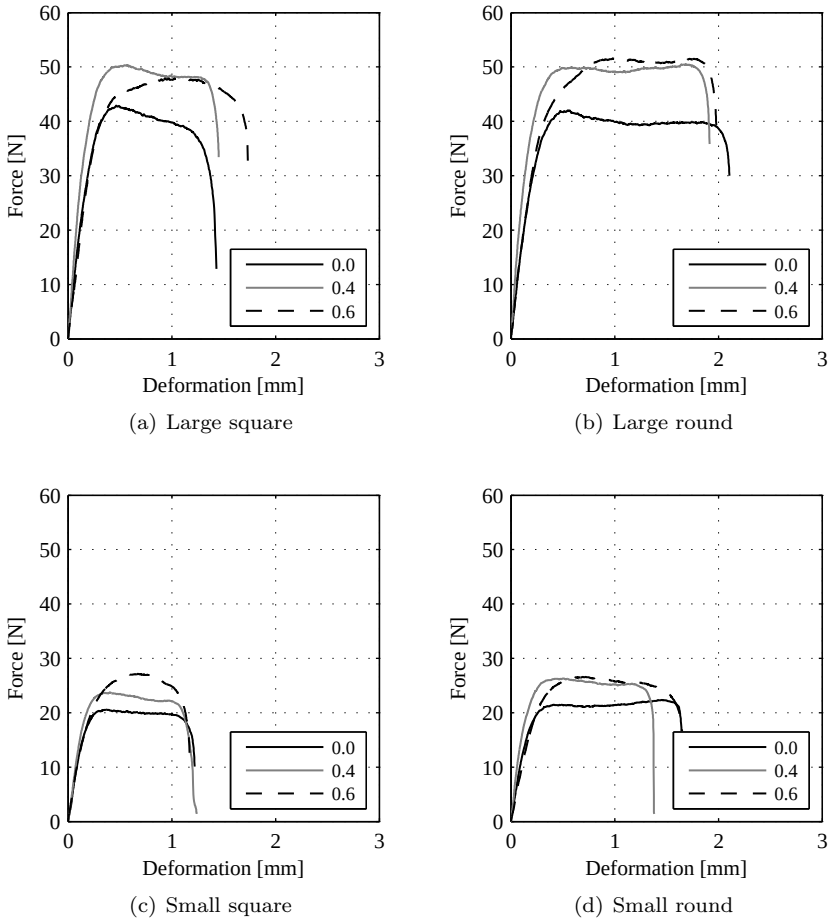

(a) Large square (b) Large round

(c) Small square (d) Small round

Figure B.8.: Force-deformation curves for specimens with different V/N-ratios and orientation of $90°/55°$ and a loading rate of $15\mu m/s$ tested in tension

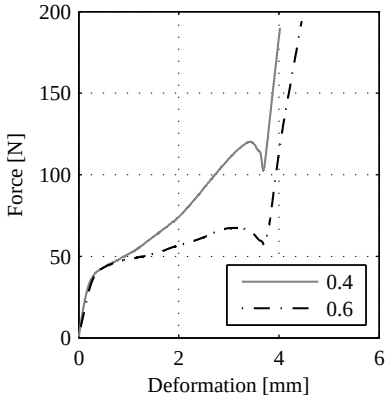

(a) Large square cross section/ loading rate $5\mu m/s$

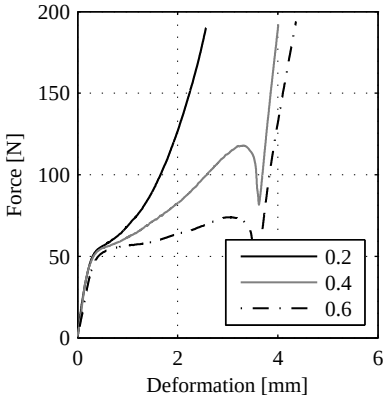

(b) Large square cross section/ loading rate $15\mu m/s$

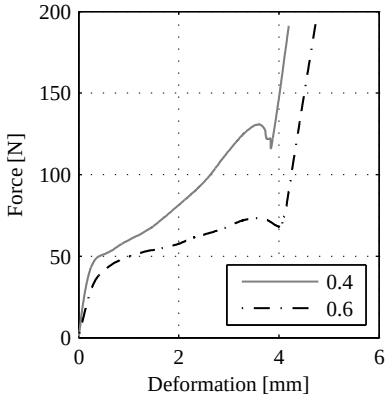

(c) Large round cross section/ loading rate $5\mu m/s$

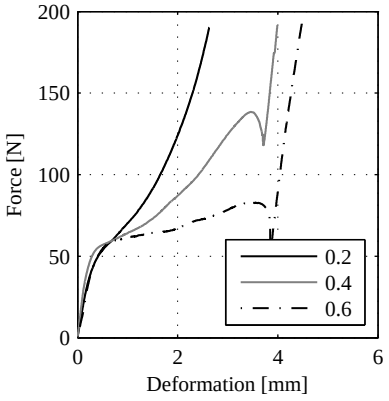

(d) Large round cross section/ loading rate $15\mu m/s$

Figure B.9.: Force-deformation curves for beams with large cross-section, different V/N ratios and orientation of 90°/55° tested in compression

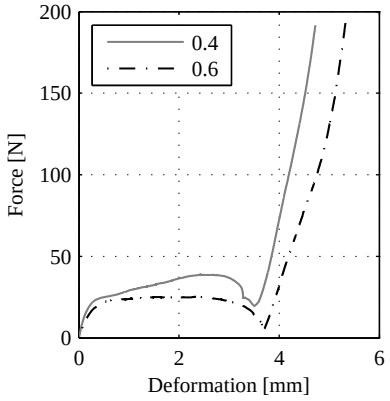

(a) Small square cross section/ loading rate $5\mu m/s$

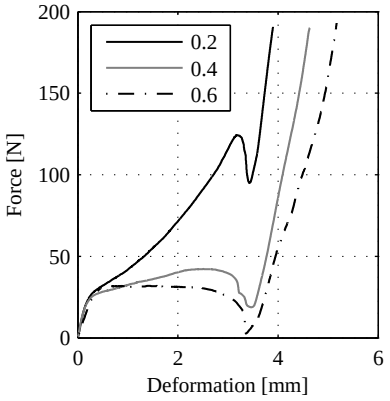

(b) Small square cross section/ loading rate $15\mu m/s$

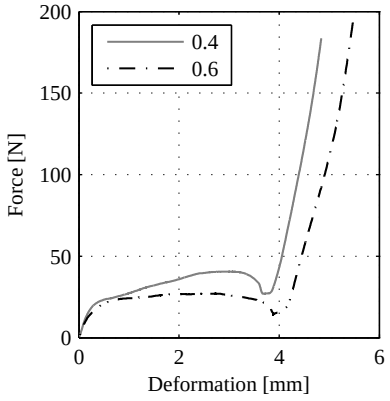

(c) Small round cross section/ loading rate $5\mu m/s$

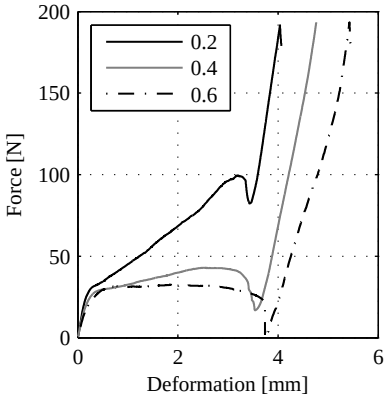

(d) Small round cross section/ loading rate $15\mu m/s$

Figure B.10.: Force-deformation curves for beams with small cross section, different V/N ratios and orientation of 90°/55° tested in compression

C. Tables and figures for lattice experiments

C.1. LVDT measurements for tensile experiments

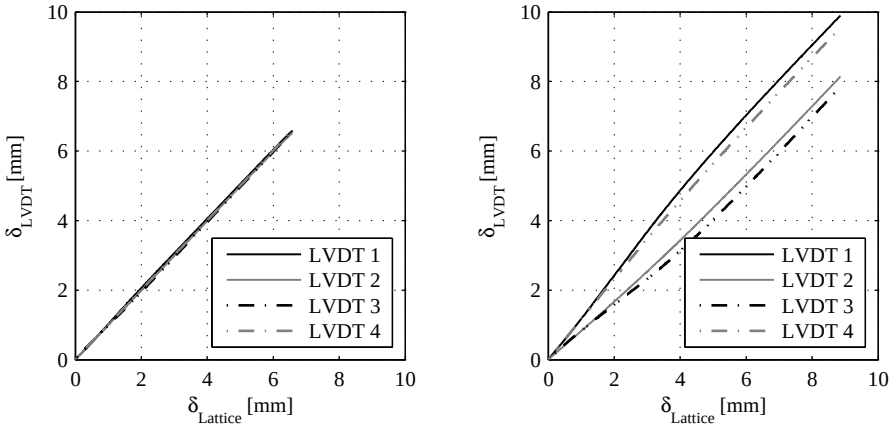

(a) Lattice with large square beams test 1

(b) Lattice with large square beams test 2

Figure C.1.: LVDT measurements: (a) measurement with a difference less than $0.1mm$, (b) measurement with a difference of $2.0mm$

C.2. LVDT measurement for compressive experiments

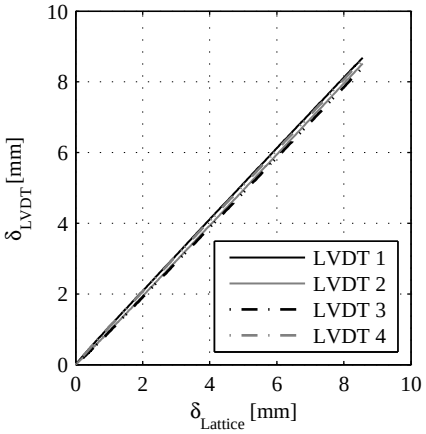

Figure C.2.: Typical LVDT measurement for compressive experiment with a difference of $0.2mm$. The difference takes place at the beginning of the measurement due to contact effect and does not change over the measured lattice deformation

C.3. Crack patters

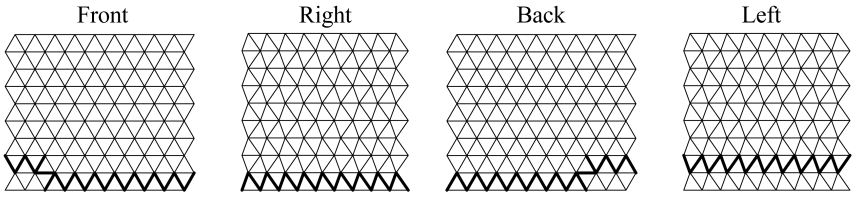

(a) Lattice with large square beams test 1

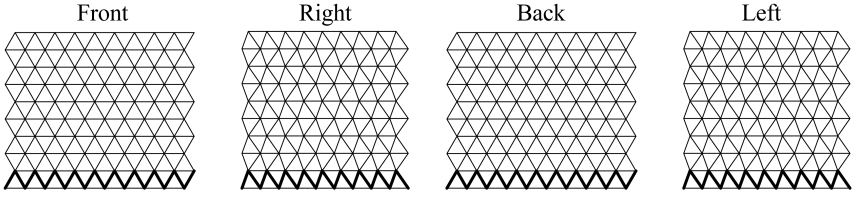

(b) Lattice with large square beams test 2

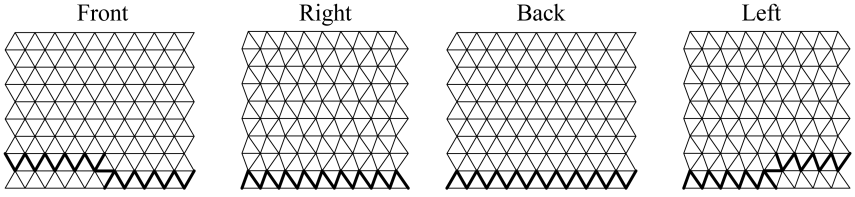

(c) Lattice with large round beams test 1

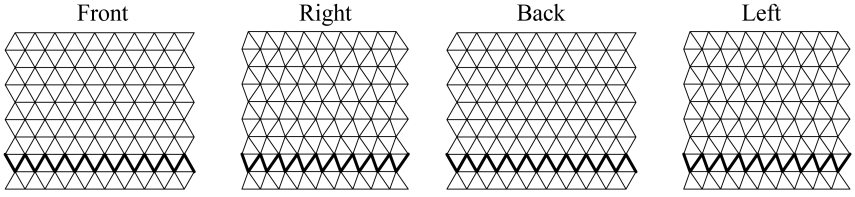

(d) Lattice with large round beams test 2

Figure C.3.: Crack pattern for lattices with large beams

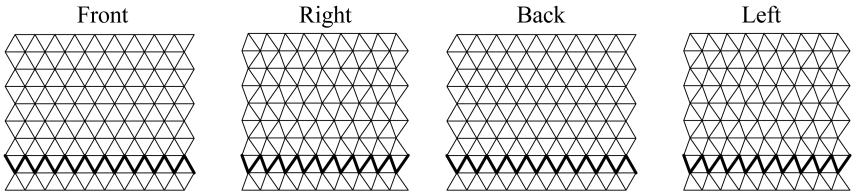

(a) Lattice with small square beams test 1

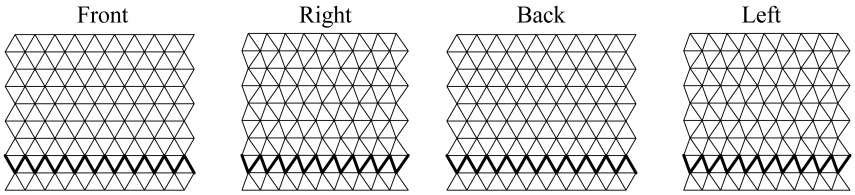

(b) Lattice with small square beams test 2

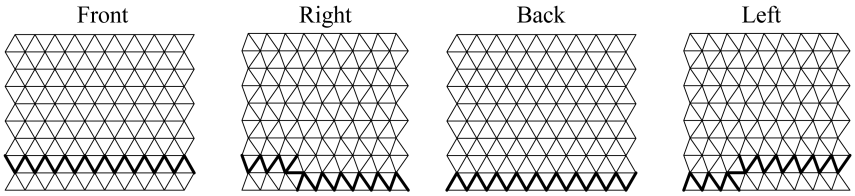

(c) Lattice with small round beams test 1

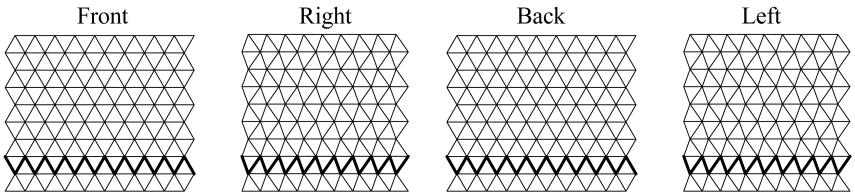

(d) Lattice with small round beams test 2

Figure C.4.: Crack pattern for lattices with small beams

D. Tables and figures for numerical investigation

D.1. Input parameters for classical model

Table D.1.: Input parameters for classical model for all geometries and loading rate of $5\mu m/s$; in-plane: 0°/0°,60°/0°, out-of-plane: 30°/55°,90°/55°

	Modulus of elasticity [MPa]		**Strength [MPa]**		**Ultimate deformation [mm]**	
	in-plane	out-of-plane	in-plane	out-of-plane	in-plane	out-of-plane
Large square	554	344	-	9.7	-	2.4
Large round	439	285	-	8.9	-	3.1
Small square	594	329	-	8.4	-	2.0
Small round	415	302	-	7.9	-	2.7

Table D.2.: Input parameters for classical model for all geometries and loading rate of $15\mu m/s$; in-plane: 0°/0°,60°/0°, out-of-plane: 30°/55°,90°/55°

	Modulus of elasticity [MPa]		**Strength [MPa]**		**Ultimate deformation [mm]**	
	in-plane	out-of-plane	in-plane	out-of-plane	in-plane	out-of-plane
Large square	683	505	-	14.5	-	1.7
Large round	546	396	-	13.0	-	2.5
Small square	775	462	-	12.0	-	1.6
Small round	616	451	-	11.4	-	1.7

D.2. Additional figures for parameter studies

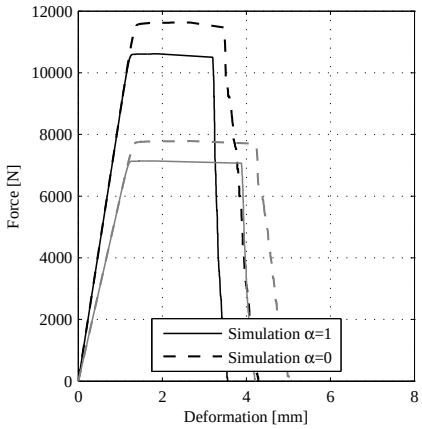

(a)

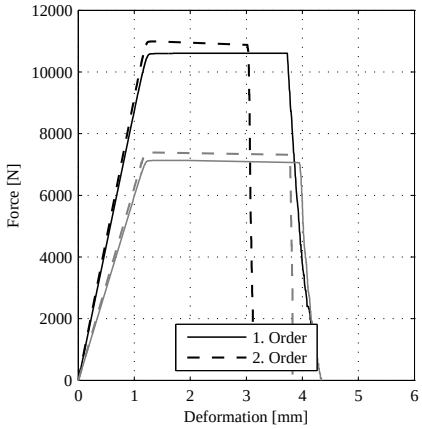

(b)

Figure D.1.: Influences on the simulated lattice behaviour with large square cross-sectional beams: (a) Variation of parameter α, (b) Influence of the second order effect

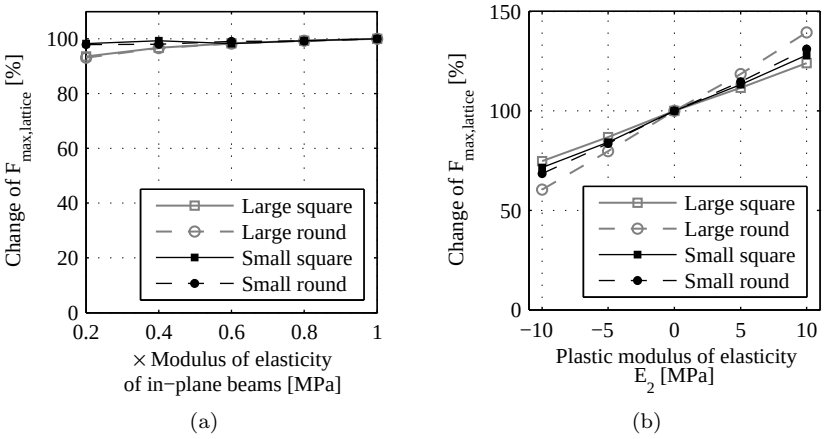

Figure D.2.: Variation of $F_{max,lattice}$ for two varying input parameters

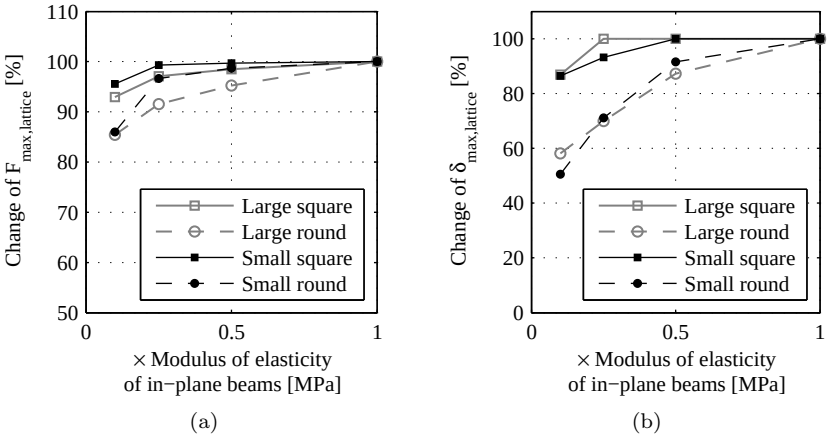

Figure D.3.: Variation of $F_{max,lattice}$ and $\delta_{max,lattcie}$ for varying modulus of elasticity of the in-plane beams

Bibliography

Abe F, Osakada K, Shiomi M, Uematsu K, Matsumoto M (2001) The manufacturing of hard tools from metallic powders by selective laser melting. Journal of Materials Processing Technology 111(1-3):210–213

Agarwala M, Bourell D, Beaman J, Marcus H, Barlow J (1995) Direct selective laser sintering of metals. Rapid Prototyping Journal 1(1):26–36

Andrews E, Gioux G, Onck P, Gibson L (2001) Size effects in ductile cellular solids. part 2: experimental results. International Journal of Mechanical Sciences 43(3):701–713

Arslan A, Schlangen E, Van Mier J (1995) Effect of model fracture law and porosity on tensile softening of concrete. In: edited by F H Wittmann (ed) Fracture Mechanics of Concrete and Concrete Structures; Proceedings FRAMCOS-2, Adeificatio Publishers, vol 1, pp 45–54

ASTM D638 (2008) Standard Test Method for Tensile Properties of Plastics

Beaman JJ, Marcus HL, Bourell DL, Barlow JW, Crawford RH, McAlea KP (1997) Solid freeform fabrication: a new direction in manufacturing. Kluwer Academic Publishers

Bolander J, Sukumar N (2005) Irregular lattice model for quasistatic crack propagation. Physical Review B 71(9):094–106

Bolander JE, Choi S, Duddukuri SR (2008) Fracture of fiber-reinforced cement composites: effects of fiber dispersion. International journal of fracture 154(1-2):73–86

Bolander Jr J, Shiraishi T, Isogawa Y (1996) An adaptive procedure for fracture simulation in extensive lattice networks. Engineering fracture mechanics 54(3):325–334

Bolon DA, Lucas GM, Olson DR, Webb KK (1980) Effect of humidity and elevated temperatures on physical properties of uv-cured polymers. Journal of Applied Polymer Science 25(4):543–553

Bourell DL, Beaman JJJ (2012) The history of laser additive manufacturing. Laser Editorials

Burt NJ, Dougill JW (1977) Progressive failure in a model heterogeneous medium. Journal of the Engineering Mechanics Division 103(3):365–376

Caduff D, Van Mier JG (2010) Analysis of compressive fracture of three different concretes by means of 3d-digital image correlation and vacuum impregnation. Cement and Concrete Composites 32(4):281–290

Cheah C, Nee A, Fuh J, Lu L, Choo Y, Miyazawa T (1997) Characteristics of photopolymeric material used in rapid prototypes part i. mechanical properties in the green state. Journal of Materials Processing Technology 67(1-3):41–45

Cheah C, Fuh J, Nee A, Lu L (1999) Mechanical characteristics of fiber-filled photo-polymer used in stereolithography. Rapid Prototyping Journal 5(3):112–119

Chockalingam K, Jawahar N, Chandrasekar U, Ramanathan K (2008) Establishment of process model for part strength in stereolithography. Journal of materials processing technology 208(1):348–365

Chu T, Ranson W, Sutton M (1985) Applications of digital-image-correlation techniques to experimental mechanics. Experimental Mechanics 25(3):232–244

Chua CK, Leong KF, Lim CCS (2010) Rapid prototyping: principles and applications. World Scientific

Corr D, Accardi M, Graham-Brady L, Shah S (2007) Digital image correlation analysis of interfacial debonding properties and fracture behavior in concrete. Engineering Fracture Mechanics 74(1):109–121

Crisfield M, Remmers J, Verhoosel C, et al (2012) Nonlinear finite element analysis of solids and structures. John Wiley & Sons

Curtis J, Hanna S, Patterson E, Taroni M (2003) On the use of stereolithography for the manufacture of photoelastic models. Experimental mechanics 43(2):148–162

Deckard CR (1988) Selective laser sintering. PhD thesis, The University of Texas at Austin

DIN 50125 (2009) Testing of metallic materials - Tensile test pieces

DIN 53504 (2009) Testing of rubber - determination of tensile strength at break, tensile stress at yield, elongation at break and stress values in a tensile test

DIN EN ISO 527-1 (2012) Kunststoffe - Bestimmung der Zugeigenschaften - Teil 1: Allgemeine Grundsätze

Dulieu-Barton J, Fulton M (2000) Mechanical properties of a typical stereolithography resin. Strain 36(2):81–87

Duxbury PM, Leath PL, Beale PD (1987) Breakdown properties of quenched random systems: The random-fuse network. Phys Rev B 36:367–380

Fudim EV (1988) Method and apparatus for production of three-dimensional objects by photosolidification. US Patent 4,752,498

Fuh J, Choo Y, Lu L, Nee A, Wong Y, Wang W, Miyazawa T, Ho S (1997) Post-cure shrinkage of photo-sensitive material used in laser lithography process. Journal of Materials Processing Technology 63(1-3):887 – 891

Giancane S, Panella F, Nobile R, Dattoma V (2010) Fatigue damage evolution of fiber reinforced composites with digital image correlation analysis. Procedia Engineering 2(1):1307–1315

Gibson L, Ashby M (1997) Cellular Solids: Structure and Properties. (2nd ed.)Cambridge University Press

Godara A, Raabe D (2007) Influence of fiber orientation on global mechanical behavior and mesoscale strain localization in a short glass-fiber-reinforced epoxy polymer composite during tensile deformation investigated using digital image correlation. Composites Science and technology 67(11):2417–2427

Gong L, Kyriakides S, Jang WY (2005) Compressive response of open-cell foams. part 1: Morphology and elastic properties. International Journal of Solids and Structures 42(5-6):1355–1379

Grediac M (2004) The use of full-field measurement methods in composite material characterization: interest and limitations. Composites Part A: applied science and manufacturing 35(7):751–761

G'sell C, Jonas J (1979) Determination of the plastic behaviour of solid polymers at constant true strain rate. Journal of Materials Science 14(3):583–591

Hague R, Mansour S, Saleh N, Harris R (2004) Materials analysis of stereolithography resins for use in rapid manufacturing. Journal of Materials Science 39(7):2457–2464

Herrmann HJ, Hansen A, Roux S, et al (1989) Fracture of disordered, elastic lattices in two dimensions. Physical Review B 39(1):637–648

Hild F, Roux S (2006) Digital image correlation: from displacement measurement to identification of elastic properties - a review. Strain 42(2):69–80

Hilyard N (1982) Mechanics of cellular plastics. Applied Science

Hilyard N, Cunningham A (1994) Low density cellular plastics: physical basis of behaviour, vol 5. Chapman & Hall London

Hrennikoff E (1941) Solutions of problems of elasticity by the framework method. Journal of Applied Mechanics 12:169–175

Hsieh C, Thomson R (1973) Lattice theory of fracture and crack creep. Journal of Applied Physics 44(5):2051–2063

Ince R, Arslan A, Karihaloo B (2003) Lattice modelling of size effect in concrete strength. Engineering Fracture Mechanics 70(16):2307–2320

Jacobs PF (1992) Rapid prototyping and manufacturing: fundamentals of stereolithography. Sme

Jacobs PF (1995) Stereolithography and other RP&M technologies: from rapid prototyping to rapid tooling. Society of Manufacturing Engineers

Jang WY, Kyriakides S (2009a) On the crushing of aluminum open-cell foams: Part 1: Experiments. International Journal of Solids and Structures 46(3):617 – 634

Jang WY, Kyriakides S (2009b) On the crushing of aluminum open-cell foams: Part 2: analysis. International Journal of Solids and Structures 46(3):635 – 650

Jerabek M, Major Z, Lang R (2010) Strain determination of polymeric materials using digital image correlation. Polymer Testing 29(3):407–416

Joseph C, Jefferson A (2007) Stochastic regularisation of lattice modelling for the failure of quasi-brittle materials. Proceedings of Fracture Mechanics of Concrete and Concrete Structures 6

Karalekas D, Rapti D (2002) Investigation of the processing dependence of sl solidification residual stresses. Rapid prototyping journal 8(4):243–247

Kim H, Buttlar WG (2005) Micro mechanical fracture modeling of asphalt mixture using the discrete element method. Geotechnical Special Publication (130-142):209–223

Klocke F, Celiker T, Song YA (1995) Rapid metal tooling. Rapid prototyping journal 1(3):32–42

Kochan D (1993) Solid freeform manufacturing: advanced rapid prototyping. Elsevier Science Inc.

Kontou E, Farasoglou P (1998) Determination of the true stress-strain behaviour of polypropylene. Journal of Materials Science 33(1):147–153

Kruth J (1991) Material incress manufacturing by rapid prototyping techniques. Annals - Manufacturing Technology 40(2):603–614

Kuentz M, Jolin M, Bastien J, Perez F, Hild F (2006) Digital image correlation analysis of crack behavior in a reinforced concrete beam during a load test. Canadian Journal of Civil Engineering 33(11):1418–1425

Landis EN, Vasic S, Davids WG, Parrod P (2002) Coupled experiments and simulations of microstructural damage in wood. Experimental mechanics 42(4):389–394

Liliu G (2007) 3d analysis of fracture processesin concrete. PhD thesis, TU Delft

Lilliu G, Van Mier JG (2003) 3d lattice type fracture model for concrete. Engineering Fracture Mechanics 70(7):927–941

Liu XY, Jiang J (2003) Environmental effects on the dimensions of sl5195 resin. Rapid Prototyping Journal 9(2):88–94

Ma D, Lin F, Chua C (2001) Rapid prototyping applications in medicine. part 1: Nurbs-based volume modelling. The International Journal of Advanced Manufacturing Technology 18(2):103–117

Man HK (2010) Analysis of 3d scale and size effects in numerical concrete. PhD thesis, ETH Zurich

Man HK, van Mier JG (2008) Size effect on strength and fracture energy for numerical concrete with realistic aggregate shapes. International journal of fracture 154(1-2):61–72

Mangipudi K, Onck P (2011) Multiscale modelling of damage and failure in two-dimensional metallic foams. Journal of the Mechanics and Physics of Solids 59(7):1437–1461

McAlea K (1997) Materials and applications for the sls selective laser sintering process. Proceedings of the 7th International Conference on Rapid Prototyping-1997 pp 23–33

Meisel NA, Williams CB, Druschitz A (2012) Lightweight metal cellular structures via indirect 3d printing and casting. In: International Solid Freeform Fabrication Symposium, pp 162–176

Metelnick J (1991) How today's model/prototype shop helps designers use rapid prototyping to full advantage. Society of Manufacturing Engineers

Nooru-Mohamed MB (1992) Mixed-mode fracture of concrete: an experimental approach. PhD thesis, Delft University of Technology

Onck P, Andrews E, Gibson L (2001) Size effects in ductile cellular solids. part i: modeling. International Journal of Mechanical Sciences 43(3):681–699

Onck P, Van Merkerk R, De Hosson JTM, Schmidt I (2004) Fracture of metal foams: In-situ testing and numerical modeling. Advanced engineering materials 6(6):429–431

Ottemer X, Colton JS (2002) Effects of aging on epoxy-based rapid tooling materials. Rapid Prototyping Journal 8(4):215–223

Prinz FB, Atwood CL, Aubin RF, Beaman JJ, Brown RL, Fussell PS, Lightman AJ, Sachs E, Weiss LE, Wozny MJ (1997) Rapid prototyping in europe and japan. Center for Advanced Technology 102

Puebla K, Arcaute K, Quintana R, Wicker RB (2012) Effects of environmental conditions, aging, and build orientations on the mechanical properties of astm type i specimens manufactured via stereolithography. Rapid Prototyping Journal 18(5):374–388

Quintana R, Choi JW, Puebla K, Wicker R (2010) Effects of build orientation on tensile strength for stereolithography-manufactured astm d-638 type i specimens. The International Journal of Advanced Manufacturing Technology 46(1-4):201–215

Rieger C (2010) Micro-fibre cement; pullout tests, uniaxial tensile tests and material scaling. PhD thesis, ETH Zuerich

Saleh N, Hopkinson N, Hague RJ, Wise S (2004) Effects of electroplating on the mechanical properties of stereolithography and laser sintered parts. Rapid prototyping journal 10(5):305–315

Salmoria G, Ahrens C, Fredel M, Soldi V, Pires A (2005) Stereolithography somos 7110 resin: mechanical behavior and fractography of parts post-cured by different methods. Polymer Testing 24(2):157–162

Sandoval JH, Wicker RB (2006) Functionalizing stereolithography resins: effects of dispersed multi-walled carbon nanotubes on physical properties. Rapid Prototyping Journal 12(5):292–303

Santos E, Osakada K, Shiomi M, Kitamura Y, Abe F (2004) Microstructure and mechanical properties of pure titanium models fabricated by selective laser melting. Proceedings of the Institution of Mechanical Engineers, Part C: Journal of Mechanical Engineering Science 218(7):711–719

Santos EC, Shiomi M, Osakada K, Laoui T (2006) Rapid manufacturing of metal components by laser forming. International Journal of Machine Tools and Manufacture 46(12-13):1459–1468

Scheirs J (2000) Compositional and failure analysis of polymers: a practical approach. Wiley. com

Schlangen E (1993) Experimental and numerical analysis of fracture processes in concrete. Phd Thesis TU Delft

Schlangen E, Garboczi E (1997) Fracture simulations of concrete using lattice models: Computational aspects. Engineering Fracture Mechanics 57(2):319 – 332

Schlangen E, Van Mier J (1992a) Experimental and numerical analysis of micromechanisms of fracture of cement-based composites. Cement and Concrete Composites 14(2):105–118

Schlangen E, Van Mier J (1992b) Simple lattice model for numerical simulation of fracture of concrete materials and structures. Materials and Structures 25(9):534–542

Schlangen E, Van Mier J (1993) Lattice model for simulating fracture of concrete. In FH Wittmann, editor, Numerical Models in Fracture Mechanics of Concrete A.A. Balkema Publishers:195–205

Schmidt I, Fleck N (2001) Ductile fracture of two-dimensional cellular structures - dedicated to prof. dr.-ing. d. gross on the occasion of his 60th birthday. International Journal of Fracture 111(4):327–342

Schorn H, Rode U (1989) 3-d-modeling of process zone in concrete by numerical simulation. In: Fracture of concrete and rock, Springer, pp 220–228

Stähli P (2008) Ultra-fluid, oriented hybrid-fibre-concrete. PhD thesis, ETH Zurich

Suh K, Webb D (1985) Cellular materials. Wiley-Interscience, Encyclopedia of Polymer Science and Engineering 3:1–59

Suh KW (1980) Foamed plastics. Kirk-Othmer Encyclopedia of Chemical Technology

Sutton MA, Orteu JJ, Schreier HW (2009) Image correlation for shape, motion and deformation measurements: basic concepts, theory and applications. Springer

Thomson R, Hsieh C, Rana V (1971) Lattice trapping of fracture cracks. Journal of Applied Physics 42(8):3154–3160

Tolochko N, Laoui T, Khlopkov Y, Mozzharov S, Titov V, Ignatiev M (2000) Absorptance of powder materials suitable for laser sintering. Rapid Prototyping Journal 6(3):155–160

Van Mier JGM (1991) Mode i fracture of concrete: discontinuous crack growth and crack interface grain bridging. Cement and concrete research 21(1):1–15

Van Mier JGM (1997) Fracture processes of concrete: Assesment of material parameters for fracture models. CRC Press (Boca Raton)

Van Mier JGM (2007) Multi-scale interaction potentials (f-r) for describing fracture of brittle disordered materials like cement and concrete. International Journal of Fracture 143(1):41–78

Van Mier JGM (2012) Concrete Fracture: A Multiscale Approach. CRC Press

Van Mier JGM (2013) A solution to the parameter-identification conundrum: multi-scale interaction potentials. International Journal of Fracture pp 1–13

Van Mier JGM, Schlangen E, Vervuurt A (1996) Tensile cracking in concrete and sandstone: Part 2-effect of boundary rotations. Materials and Structures 29(2):87–96

Van Vliet MRA (2000) Size effect in tensile fracture of concrete and rock. PhD thesis, TU Delft

Van Vliet MRA, van Mier JGM (2000) Experimental investigation of size effect in concrete and sandstone under uniaxial tension. Engineering Fracture Mechanics 65(2):165–188

Vanlanduit S, Vanherzeele J, Longo R, Guillaume P (2009) A digital image correlation method for fatigue test experiments. Optics and Lasers in Engineering 47(3):371–378

Vervuurt A (1997) Interface fracture in concrete. PhD thesis, TU Delft

Vervuurt A, Van Mier JGM (2000) Experimental and numerical analysis of boundary effects in uniaxial tensile tests. Localized Damage III pp 3–10

Wattrisse B, Chrysochoos A, Muracciole JM, Némoz-Gaillard M (2001) Analysis of strain localization during tensile tests by digital image correlation. Experimental Mechanics 41(1):29–39

Weibull W (1939) A statistical theory of the strength of materials. Royla Swedish Academy of Engineering Sci Proc 151:1–45

Wendle BC (1976) Engineering guide to structural foam. CRC

List of Symbols

Abbreviations

DIC	Digital image correlation
$ESEM$	Environmental Scanning Electron Microscope
$LVDT$	Linear variable differential transducer
RP	Rapid prototyping
SL	Stereolithography
SLS	Selective laser sintering
STL	Standard Tesselation Language
V/N	Shear to normal force

Greek

α	Weighting factor of the moment to the normal stress [-]
$\delta_{max,beam}$	Maximum deformation of one single beam element [mm]
$\delta_{max,lattice}$	Maximum deformation of the global lattice [mm]
ϵ_i	Strain in one beam [%]
ϵ_{max}	Maximum strain of one beam [%]
η	Viscosity [m^2/s]
λ	Slenderness of one beam
μ	Force and deformation scale factor
ν	Poisson's ratio [-]
σ_i	Normal stress in one beam [MPa]
φ	Virtual rotation

$\xi_{i,j}$	Stress scale factor for element i at step j
$\zeta_{i,j}$	Strain scale factor for element i at step j

Variables

$\delta_{max,beam}$	Maximum deformation at failure of one beam element [mm]
A	Cross-sectional area of one beam [mm^2]
A_{eq}	Equivalent area of one beam whit a non-constant shape [mm^2]
E	Modulus of elasticity [MPa]
E_2	Plastic modulus of elasticity [MPa]
E_{beam}	Modulus of elasticity of a single beam element [MPa]
F	Global force vector [N]
F_i	Normal force in one beam element [N]
$F_{elastic,lattice}$	Force of the global lattice at first yielding of one beam [N]
$F_{max,lattice}$	Maximum force of the global lattice [N]
f_{pl}	Yielding stress [MPa]
G	Shear modulus [MPa]
I_y, I_z	Cross-sectional moment of inertia of one beam [mm^4]
I_{eq}	Equivalent moment of inertioa of one beam whit a non-constant shape [mm^4]
J	Cross-sectional polar moment of inertia of one beam [mm^4]
K	Global stiffness matrix
k_g	Geometrical stiffness matrix
$K_{lattice}$	Stiffness of global lattice [N/mm]
L	Length of one beam [mm]
M_i	Maximum end moment in one beam element [Nmm]
T	Normal Force in one beam [MPa]
U	Global deformation vector [mm]
w_i	Deformation of one beam [mm]
$W_{el,pl}$	Elastic or plastic moment of resistance [mm^3]

List of Publications

Caduff D, Fontana M, van Mier JGM (2014) Experimental and numerical investigations of the mechanics of 3d lattice structures produced by rapid prototyping (submitted)

Caduff D, Van Mier JGM (2010) Analysis of compressive fracture of three different concretes by means of 3d-digital image correlation and vacuum impregnation. Cement and Concrete Composites 32(4):281–290

Niemz P, Caduff D (2008) Research into determination of the poisson ratio of spruce wood. Holz als Roh-und Werkstoff 66(1):1–4

Acknowledgement

This Ph.D. thesis was carried out at the Institute of Structural Engineering (IBK) and the Institute of Building Materials (IfB), Departement of Civil, Environmental and Geomatic Engineering (D-BAUG) of ETH Zuerich from September 2008 until March 2014.

I would like to thank Prof. Dr. Mario Fontana, who gave me the opportunity to continue and finish my thesis under his supervision. Thank you for the profitable discussions and the support during the work.

I would like to express my sincere gratitude to my co-examiner Prof. Dr. ir. Jan G.M van Mier. Thank you that I could start my work under your supervision and for your support, the constructive discussions and the freedom you gave me over the whole time. Thanks a lot that you gave me the opportunity to work on this research project and the completion of the thesis. I am very thankful for having made all this possible.

I would also like to thank Prof. Dr. Robert J. Flatt and Prof. Dr. Peter Niemz for the opportunity to use the testing machines from the IfB.

A lot of people were involved to make this work possible in terms of technical, theoretical and financial help. A great thank to Heinz Richer for his support in the lab and the fruitful discussions. It was a very great time to work with you. I would like to thank Simon Zweidler for the discussions about the topic during the work and also after work. You were a big help for me during the whole time. Thanks a lot for your patience and your inputs. I want to express my thank to Gabriele Peschke for great work with the microscopy. A special thank goes to Peter Jenny for his support and great work at the testing devices and the collaborative discussions. For the support on the electronic equipment I want to thank Ernst Bleiker and Cornelius Senn. I thank the Bauhallen-Team Thomas Jaggi, Dominik Werne, Partick Morf and Christoph Gisler for their help at the testing machines. For the IT-support, I want to thank Roberto Pascolo. I thank also Thomas Schnider, Franco Michel and Werner Dahinden for their support.

A special thank goes to Dr. Patrick Dilger and Edith Altenburger from the departement D-BAUG, who supported me in the financial concerns. Thank you Edith that you did the financial work for me.

I want to thank my group members for the great time to work with them, namely Diego Somaini, Fangxia Lu, Eike Klingsch, Jacqueline Pauli, Martin Neuenschwander, Dr. Markus Knobloch, Katharina Fischer, Gianluca De Sanctis, Partick Schulthess, Claudio Scandella, Lex Reiter and Heidi Honegger. Thank you for the discussions and the support. I also want to thank the members of the timber group, namely Prof. Dr. Andrea Frangi, Matthias Theiler, Michael

Klippel, Flavio Wanninger, Gerhard Fink, Robert Jockwer, Peter Kobel, Lorenzo Boccadoro, Claude Leyder, Lukas Blank and Pedro Palma for the discussions and the nice time.

Finally, I want to thank my family and friends for their great support during the whole time, my parents and my sister, Simon, Eike, Diego, Jacqueline, Luis, Fangxia, Markus, Dominik, Thomas, Matthias Fuhr, Matthias Theiler, Michael, Flavio, Reto, Hans, Claudia and Christian with their family, Miryam and Roman with their family and Jasmin and Bruno with their family.

Daniel Caduff, March 2014